# Application of statistical physics tools to intracellular transport

**Dissertation**

zur Erlangung des Grades
des Doktors der Naturwissenschaften

der Naturwissenschaftlich-Technischen Fakultät II
- Physik und Mechatronik -
der Universität des Saarlandes

und

der Université Paris-Saclay am Standort Université Paris-Sud
ED564 : «Physique en Île-de-France» / NNT: 2016SACLS090

von
**Sarah Klein**

Saarbrücken
2015

| | |
|---|---|
| Tag des Kolloquiums: | 27.04.2016 |
| Dekan: | Univ.-Prof. Dr. Georg Frey |
| Mitglieder des Prüfungsausschusses: | Dr. Cécile Appert-Rolland<br>Prof. Dr. Hendrik-Jan Hilhorst<br>Prof. Dr. Jan Kierfeld<br>Prof. Dr. Giovanna Morigi (Vorsitzende)<br>Prof. Dr. Andrea Parmeggiani<br>Prof. Dr. Ludger Santen<br>Dr. Emmanuel Terriac |

# Eidesstattliche Versicherung

Hiermit versichere ich an Eides statt, dass ich die vorliegende Arbeit selbstständig und ohne Benutzung anderer als der angegebenen Hilfsmittel angefertigt habe. Die aus anderen Quellen oder indirekt übernommenen Daten und Konzepte sind unter Angabe der Quelle gekennzeichnet. Die Arbeit wurde bisher weder im In- noch im Ausland in gleicher oder ähnlicher Form in einem Verfahren zur Erlangung eines akademischen Grades vorgelegt.

_____

Ort, Datum

_____

Unterschrift

## Abstract

Most processes in our daily life are far from equilibrium. The prime example is a cell and the transport occurring within. In this thesis intracellular transport is modeled by means of stochastic processes. For this, two different approaches are applied: the explicit modeling of active particles with internal degrees of freedom with characteristics as they were determined experimentally. And secondly, the collective effects occurring in many particle systems are studied in a phenomenological way by means of exclusion processes.

In the explicit model one important result is given by the fact that force fluctuations are essential to capture the relevant motion characteristics. Further, the influence of the cellular environment creates counter-intuitive effects, like a possible inversion of the bias. The motion characteristics can be represented in a coarse-grained manner as an exclusion process for particles with internal states. Due to the resulting disorder in the hopping rates a density-dependent condensation occurs.

In a second part, a two-lane exclusion model is studied. Two species in a tubular geometry inspired by filamentous fungi are considered.This can be seen as a minimal model exhibiting a phase transition from a low density phase to an intriguing phase with periodically changing particle densities.

**Keywords:** stochastic modeling, non-equilibrium systems, bidirectional transport, molecular motors, intracellular transport, exclusion processes.

## Kurzzusammenfassung

Die meisten Prozesse in unserem täglichen Leben laufen unter Zufuhr von Energie ab und müssen daher als Nichtgleichgewichtszustände gesehen werden. Ein wichtiges Beispiel hierfür ist eine biologische Zelle und der darin auftretende Transport. In dieser Arbeit werden Aspekte jenes intrazellulären Transports mittels stochastischer Prozesse modelliert. Dazu werden zwei unterschiedliche Herangehensweisen untersucht: Zum einen das explizite Modellieren aktiver Teilchen mit innerem Freiheitsgrad mit Bewegungscharakteristiken wie sie experimentell bestimmt wurden. Zum anderen mittels eines phänomenologischen Ansatzes gegeben durch Exklusionsprozesse.

Als eines der Hauptergebnisse im expliziten Modell wird gezeigt, dass Kraftfluktuationen von essentieller Natur sind, um relevante Bewegungscharakteristiken zu erzeugen. Weiter ist der Einfluss des zellulären Millieus nicht zu vernachlässigen, was zum Beispiel eine Umkehrung des Richtungsbias herführen kann. Der Transport kann im Rahmen einer effektiven Beschreibung durch ein Teilchen mit internen Bewegungszuständen repräsentiert werden. Aufgrund der dadurch resultierenden Unordnung in den Hüpfraten entsteht eine dichteabhängige makroskopische Kondensation.

Des Weiteren wird ein zwei-spuriger Exklussionsprozess analysiert. In diesem bewegen sich zwei Teilchenspezies in einer röhrenartigen Geometrie, die durch filamentartige Fungizellen inspiriert wurde. Diese Annahmen definieren ein minimales Modell, das einen Phasenübergang von einer Niedrigdichtephase zu einer faszinierenden Phase mit periodischen Dichteänderung aufweist.

**Stichworte:** stochastische Modellierung, Nicht-Gleichgewichtssysteme, bidirektionaler Transport, molekulare Motoren, intrazellulärer Transport, Exklusionsprozesse.

## Résumé

La plupart des processus dans notre vie quotidienne sont des processus hors équilibre. Un exemple de système hors équilibre est la cellule biologique et le transport qui a lieu dedans. Dans cette thèse ce transport intracellulaire est modélisé par des processus stochastiques. Pour cela deux approches différentes ont été utilisées : d'une part une modélisation explicite de particules actives avec des degrés de liberté internes obtenus expérimentalement, d'autre part une description phénoménologique des effets collectifs, qui est réalisée au moyen de processus d'exclusion.

Un des résultats principaux pour le modèle explicite est qu'il est crucial de prendre en compte les fluctuations des forces pour reproduire les caractéristiques principales du mouvement. Un autre élément important est la prise en considération de l'environnement cellulaire, qui peut produire des effets non-triviaux, comme par exemple une inversion du sens de déplacement moyen. Pour étudier les effets collectifs il est possible de représenter le mouvement des particules d'une manière simplifiée, en utilisant un processus d'exclusion avec des particules ayant des états internes. Le désordre sur les taux de saut qui en résulte peut provoquer une condensation dépendant de la densité.

Un autre modèle étudié est un processus d'exclusion sur un réseau à deux voies. On suppose que deux types de particules se déplacent dans une géométrie tubulaire, inspirée par les champignons filamenteux. Ces hypothèses définissent un modèle minimal qui présente une transition de phase d'une phase de basse densité vers une phase pulsante caractérisée par des oscillations de densité.

**Mots-clés :** modélisation stochastique, systèmes hors équilibre, transport bidirectionnel, moteurs moléculaires, transport intracellulaire, processus d'exclusion.

# Zusammenfassung

Viele stochastische Prozesse, die wir aus dem Alltag kennen, wie etwa der Straßenverkehr [24,87,98], die Bewegung von Fußgängern [51] oder auch Prozesse im Innersten unserer Zellen [23, 47, 107], zeigen faszinierende Eigenschaften auf. Auch wenn diese Beispiele auf den ersten Blick sehr unterschiedlich wirken, haben sie doch aus Sicht eines Physikers vieles gemeinsam: Sie befinden sich nicht im Gleichgewicht mit ihrer Umwelt. In den oben beschriebenen Fällen kommt dieses Nichtgleichgewicht dadurch zustande, dass die jeweiligen Objekte selbstgetrieben sind. Diese Eigenschaft führt dazu, dass die theoretische Beschreibung des Systems deutlich schwieriger ist, da man sich nicht wie in der Gleichgewichtsstatistik auf eine allgemeingültige Theorie stützen kann. Diese Arbeit konzentriert sich ganz generell auf die Modellierung zellulärer Transportprozesse, deren Nichtgleichgewichtscharakter sich hauptsächlich auf die Umwandlung chemischer in mechanische Energie zurückführen lässt.

In gesunden Zellen ist funktionierender Transport grundlegend für fast alle Funktionen, wie etwa für die Zellteilung oder für neuronale Transportprozesse. Sind diese grundlegenden Funktionen gestört, können neurodegenerative Krankheiten wie Alzheimer oder Parkinson auftreten [28]. Um langreichweitigen Transport zu gewährleisten, bilden Zellen Proteinnetzwerke aus, entlang derer molekulare Motoren Vesikel oder gar Organelle ziehen.

Im Folgenden werde ich auf zwei unterschiedliche Arten die Physik von Nichtsgleichgewichtssystemen und in der Biologie beobachtet Effekte verbinden. Zum einen werde ich das Zusammenspiel mehrere Motoren, die an einen zellulären Cargo gebunden sind, modellieren und den resultierenden Transport prognostizieren. Zum anderen werde ich Phänomene, die durch kollektive Transporteffekte mehrerer Cargos entstehen, im Rahmen von Exklusionsprozessen untersuchen.

## Einführung in die Biologie des intrazellulären Transports

Eukaryotische Zellen bilden ein Netzwerk aus Proteinen, die intrazellulären Transport ermöglichen. In dieser Arbeit liegt der Schwerpunkt auf langreichweitigem Transport, der größtenteils entlang Mikrotubuli stattfindet. Mikrotubuli sind lange, hohle Proteinröhren, die sich aus 13 Protofilamenten zusammensetzen. Diese bilden sich durch Polymerisation

von Tubulin-Dimeren. Der Nukleationspunkt ist hierbei für einen Großteil der Zellen in der Nähe des Zellkerns, am Mikrotubuli-organisierenden Zentrum. Generell besitzen Mikrotubuli eine Polarisierung und damit ein wohldefiniertes $(+)$- und $(-)$-Ende. Letzteres ist für einen Großteil der Zellen am Mikrotubuli-organisierenden Zentrum lokalisiert. Dort bildet sich zunächst ein stabiler Ring aus $\gamma$-Tubulin. Mit der Zeit polymerisieren weitere freie Tubulin-Dimere an diesen Ring. Das in Richtung der Membran wachsende $(+)$-Ende ist im Gegensatz dazu sehr dynamisch. Es kann entweder in einem wachsenden oder schrumpfenden Zustand sein. Man spricht von einer dynamischen Instabilität. Hierbei ist wichtig, dass die Tubulin-Dimere selbst aus $\alpha$- und $\beta$-Tubulin bestehen und immer in gleicher Orientierung polymerisiert werden.

Die Polarisation gibt für die molekularen Motoren die Bewegungsrichtung vor. Allgemein kann man molekularen in zwei Gruppen unterteilen: in zytoplasmisches Dynein (im Folgenden nur noch Dynein) und in die Familie der Kinesine (im Folgenden sei Kinesin-I gemeint). Beide sind in der Lage sich entlang eines Mikrotubulus zu bewegen, allerdings unterscheiden sie sich unter anderem durch ihre Bewegungsrichtung. Im Normalfall laufen Kinesine in Richtung des $(+)$-Endes und Dynein in Richtung des $(-)$-Endes eines Mikrotubulus. Man spricht dabei von einer anterograden beziehungsweise retrograden Bewegung. Die Motoren laufen jedoch im Regelfall nicht frei entlang eines Mikrotubulus, sondern können eine Vielzahl von Vesikeln oder Organellen binden. Ziehen sie diese, wirkt eine Kraft auf die Motoren.

Generell ist nicht nur die Bewegungsrichtung der beiden Motorenarten unterschiedlich, sondern auch ihre Reaktion auf äußere Signale. So wurde zum Beispiel die Reaktion der beiden Motoren auf Adenosintriphosphat (ATP) gut untersucht. ATP ist ein Molekül, das von grundlegender Bedeutung für alle lebenden Organismen ist, da es die Energie für aktive Zellprozesse bereitstellt. Die obengenannten Motoren benötigen genau ein Molukül ATP, um eine Schritt entlang des Filaments zu machen. Doch hängt die Wahrscheinlichkeit dafür, einen Schritt zu machen, nicht nur von der ATP-Konzentration in der Zelle ab, sondern auch von der Kraft, die der Motor erfährt. Es wurde experimentell bestimmt, dass die Geschwindigkeit in Abhängigkeit der ATP-Konzentration und der Kraft für beiden Motorentypen dem gleichen Gesetz folgt [116]. Man kann sie mit einer sogenannten Michaelis-Menten-Gleichung beschreiben [100]. Diese steigt zuerst linear mit der ATP-Konzentration an und saturiert bei zellulärer ATP-Konzentration. Die Kombination aus ATP-Konzentration und Kraft aufgrund eines gebundenen Cargos erzeugt ein effektives Potential, das die Wahrscheinlichkeit für einen Motorschritt gibt. Kann man nun auch die Geschwindigkeit in Abhängigkeit der ATP-Konzentration für beide Motoren gleich modellieren, ist die Kraft, die notwendig ist, um einen Motor zum Stehen zu bringen, zum einen unterschiedlich groß, zum anderen nur für Dynein im experimentell relevanten Bereich ATP-abhängig. Bei letzterem steigt diese Blockierkraft linear von 0.3 pN bei verschwindend geringer ATP-Konzentration auf 1.2 pN bei gesättigter ATP-Konzentration an [82]. Im Gegensatz dazu

ist die Blockierkraft für Kinesin unter zellulären Bedingungen konstant und liegt bei einem Wert von etwa 6 pN [100].

Oben wurde die Anordnung von Mikrotubuli diskutiert. Die radialsymmetrische Anordnung ist für einen Großteil der Zellen gegeben [1], nämlich für eben die Zellen, die selbst mehr oder minder als kugelförmig angenommen können werden. Die Situation ist allerdings anders in sehr langen, sehr dünnen Zellen, wie zum Beispiel im Axon oder in sogenannten Hyphen-Zellen, wie sie bei Fungi auftreten. In diesen Zellen findet man, auch hier angepasst an die Geometrie der Zelle, parallele Mikrotubuli-Bündel.

In dieser Arbeit werden Transportprozesse generell und unter Berücksichtigung spezieller Zellgeometrien untersucht. Hierbei ist das Hauptproblem, dass die molekularen Motoren generell auf dem gleichen Mikrotubulus in entgegensetze Richtungen laufen können. Daher vermutet man zunächst, dass die Situation entlang eines Mikrotubulus stark gestaut sein müsste. Allerdings wird in gesunden Zellen das Gegenteil beobachtet, nämlich stabiler, bidirektionaler Transport über lange Strecken.

## Modellierung mit zellulären Automaten

In den letzten Jahre wurden viele Modelle im Rahmen sogenannter zellulärer Automaten benutzt, um intrazellulären Transport zu beschreiben. Ein einfaches Modell ist der asymmetrische einfache Exklusionsprozess. Dieser ist auf einem eindimensionalen Gitter der Länge $L$ definiert. Auf eben diesem Gitter gibt es eine gewissen (Durchschnitts-)Zahl an Teilchen, die sich nach gewissen Regeln, abhängig von dem einzelnen Modell, entlang des Gitters stochastisch bewegen. Das Exklusionprinzip erlaubt pro Gitterplatz nur genau ein Teilchen, sodass ein Teilchen nur dann zu seinem gewünschten Platz hüpfen kann, wenn dieser leer ist.

Um nun bidirektionalen Transport zu realisieren, müssen die Teilchen in beide Richtung entlang des Gitters hüpfen können. Oft ist dies jedoch stattdessen durch zwei Populationen an Teilchen modelliert, wobei die Teilchen der einen Population ausschließlich nach links und die der anderen ausschließlich nach rechts hüpfen können. Offensichtlich sind zusätzliche Regeln notwendig sind, um einen stabilen Fluss entlang solch eines Gitters zu verwirklichen.

Wir haben ein Modell entwickelt, das eine Typen-Änderung erlaubt, sodass Plus-Teilchen, die nach rechts hüpfen, zu Minus-Teilchen werden können, die nach links hüpfen und umgekehrt. Dieses Modell wurde inspiriert durch die Arbeit von Lin *et al.* [79]. Sie haben in ihrer Arbeit ein Modell, bestehend aus 13 Spuren entwickelt, um Bewegungen in Hyphenzellen zu beschreiben. Mit einem reflektierenden und einem offenen Ende finden sie eine periodische Dichteänderung entlang des Gitters für gewisse Parameterbereiche. Unser Modell ist ein minimales Modell, das genau dieses periodische Verhalten reproduziert.

Um das Modell analytisch zu untersuchen, gehen wir von einer Mean-Field-Näherung

aus. Hiermit finden wir heraus, dass zwei Spuren ausreichen, jedoch eine Asymmetrie zwischen den beiden Teilchenarten bestehen muss. Wir haben hierbei diese Asymmetrie insofern realisiert, als dass nur Minus-Teilchen zwischen den beiden Spuren wechseln können, während Plus-Teilchen warten müssen, bis ihr benachbarter Gitterplatz frei wird. Diese Regeln erlauben es, einen stabilen Teilchenfluss zu generieren. Man beobachtet, dass sich das System sehr schnell mit Teilchen auffüllt. In diesem Füllzustand gibt es am reflektierenden Rand eine Hochdichteregion, während in dem Teil des Systems am offenen Rand die durchschnittliche Teilchendichte weiterhin niedrig bleibt. Sobald das System einmal mit Teilchen angefüllt ist und somit die Zahl der Teilchen nahezu $2L$ beträgt, bildet sich am reflektierenden Rand eine Niedrigdichteregion. Diese propagiert vom geschlossenen zum offenen Ende des Systems mit einer Geschwindigkeit, die um mindestens eine Größenordnung kleiner ist als die des sich füllenden Systems. Anhand der Massenerhaltung entlang des Gitters kann man die Geschwindigkeit der Leerung des Systems abschätzen. Zusätzlich beobachtet man, dass der Teilchenfluss der Minus-Teilchen doppelt so groß ist wie der der Plus-Teilchen. Analytisch kann man dieses Ergebnis reproduzieren, indem man annimmt, dass die Dichte für beide Teilchenarten in der Hochdichteregion nur um einen sehr kleinen Wert $\eta$ von $1/2$ abweicht.

Integriert man die Mastergleichung numerisch, findet man mehrere überraschende Effekte. In der periodischen Phase beachtet man in der Hochdichteregion des sich leerenden Systems räumliche Dichteoszillationen mit exponentiell abfallender Amplitude in der Nähe des Schocks. Jedoch ist für die Summe der beiden Dichten keine Oszillation zu beobachten, wodurch sich darauf schließen lässt, dass die beiden Dichten exakt gegenphasig sind. Zusätzlich findet man in der Niedrigdichteregion nicht-sinusoidale zeitliche Oszillationen in beiden Dichten. Diese sind mit der Bewegung des Schocks um einen Gitterplatz verbunden. Sobald sich dieser um einen Platz verschiebt, entsendet er Dichtepulse zum reflektierenden Rand in beiden Teilchendichten. Man kann diesen Effekt auf die Nichtlinearität der Mastergleichung zurückführen.

Um zu verstehen, wie diese räumlichen und zeitlichen Oszillationen entstehen, vollführen wir eine Stabilitätsanalyse ähnlich wie in der Arbeit von Evans *et al.* [39]. Man nimmt an, dass konstante Dichten Lösungen der Mastergleichung sind. Zu diesen konstanten Profilen addiert man räumliche und zeitliche Instabilitäten, die für das letztendliche Profil ausschlaggebend sind. Wir finden heraus, dass die Störungen dynamisch stabil sind und exponentiell mit der Zeit abnehmen. Für die räumlichen Störungen hängt das Verhalten von der Dichte ab. Für geringe Dichten treten drei Äste auf, die mit dem Ort exponentiell abnehmen. Mit steigender Dichte werden zwei dieser drei Lösungen komplexwertig und ihr Absolutbetrag größer als eins. Dies beschreibt den exponentiellen Anstieg der Dichte in Richtung des Schocks und auch die Dichteoszillationen.

Variiert man die Parameter, um genau zu sein das Verhältnis zwischen Injektionsrate und Konvertierungsrate, findet man einen Phasenübergang zu einer Niedrigdichtepha-

se. Diese hat einen wohldefinierten stationären Nichtgleichgewichtszustand. Mittels einer Taylor-Entwicklung der Mastergleichung findet man die exakten Ausdrücke für die Dichteprofile in dieser Phase. Dieses Modell wird detailliert in einer Teilveröffentlichung analysiert werden [61].

## Das EPB-Modell

In verschiedenen Zellen wurde beobachtet, dass Objekte, wie zum Beispiel Organelle oder Vesikel, die entlang eines Filaments gezogen wird, plötzlich seine Bewegungsrichtung ändert. Einige Forscherteams haben in den letzten Jahren versucht dieses Phänomen genauer zu quantifizieren und zu modellieren [17, 72, 86]. Ein *in vivo* Experiment mit Endosomen in *Dictyostelium*-Zellen hat gezeigt, dass diese transportierten Endosome sich entlang des Mikrotubulus verlängern, wenn sie ihre Bewegungsrichtung ändern [110]. Dies zeigt, dass gleichzeitig Kräfte in entgegengesetzte Richtung auf den Cargo wirken. Diese Beobachtung weist darauf hin, dass mit großer Wahrscheinlichkeit mehrere Motoren unterschiedlicher Art zeitgleich an einen Cargo gebunden sind. Daraus schließen wir, dass auf zellulärer Ebene kein Mechanismus existiert, der zur Richtungsänderung einen Typ von Motoren deaktiviert.

Ein Modell, das diesen Sachverhalt beschreibt, wurde 2008 von Müller *et al.* [86] entwickelt. Sie postulieren in ihrer Arbeit, dass es genügt die Zahl der gebundenen Motoren pro Team in Betracht zu ziehen. Die resultierende Kraft auf den Cargo teilt sie gleichmäßig unter allen Motoren eines Teams auf. Dies ermöglicht die exakten Motorenpositionen zu vernachlässigen. Weiter wird angenommen, dass anhand dieser Kraft eine Abrissrate für die einzelnen Teams bestimmt werden kann, sodass sich die Zahl der Motoren pro Team mit der Zeit ändert. Ist ein Motor einmal abgerissen, kann er mit konstanter Rate wieder an das Filament binden und somit seinen Anteil der Kraft wieder übernehmen. Mit diesen Annahmen ist es möglich eine konstante Cargo-Geschwindigkeit zwischen zwei Motorenevents zu bestimmen, wobei sie mit steigender effektiver Kraft linear abnimmt. Man kann dies als eine Mean-Field-Näherung sehen. Mit ihrem Modell finden Müller *et al.* drei Motilitätszustände in Abhängigkeit der gewählten Parameter. Der überraschendste dieser Zustände ist der, der symmetrisch bimodale Wahrscheinlichkeitsverteilungen für die Cargogeschwindigkeit und die Zahl der gebunden Motoren pro Team zeigt (im Folgenden: Zustände mit SBDs - engl. *symmetric bimodal distributions*). Entgegen der Erwartung sind hierbei diejenigen Zustände, in denen nur ein einzelnes Team am Filament gebunden ist, sehr stabil und dominieren somit die Dynamik des Systems. In diesen Zuständen propagiert der Cargo fast durchgehend mit der kräftefreien Geschwindigkeit der Motoren.

Ein Teil dieser Arbeit besteht darin, die biologische Relevanz dieser stabiler Zustände zu analysieren. Dazu stellen wir ein Modell vor, das die Position eines jeden Motors explizit in Betracht zieht, weshalb wir es im Folgenden EPB-Modell (engl. *explicit position-*

*based*) nennen werden. In unserem Modell machen die Motoren einzelne Schritte entlang des Filaments und die Kraft, die sie durch das Strecken ihrer Proteinkette auf den Cargo erzeugen, modellieren wir als lineare Feder mit Ruhelänge $L_0$. Mit dieser Annahme berücksichtigen wir die Positions- und somit Kräftefluktuationen der einzelnen Motoren. Anhand von Monte-Carlo-Simulationen zeigen wir, dass eben diese Fluktuationen essentiell sind, um die Dynamik eines transportierten Cargos zu beschreiben. Vergleicht man die Ergebnisse für die Geschwindigkeitsverteilung und die Verteilung der Zahl der gebunden Motoren mit denen des Modells von Müller *et al.* wird leicht ersichtlich, dass Positionsfluktuationen die bimodale Struktur zerstören. Die Modellierung ist im Detail in Teilveröffentlichungen diskutiert [64, 65].

Um nun herauszufinden, welche Bedingungen gelten müssen, um Zustände mit SBDs zu erhalten, führen wir eine artifizielle gegenseitige Aktivierung der Motoren innerhalb eines Teams ein. Diese Aktivierung ist so definiert, dass die Hüpfrate eines jeden Motors, der sich innerhalb eines gewissen Radius um einen Motor, der gerade einen Schritt vollführt, aufhält, mit einem konstanten Faktor multipliziert wird. Diese Definition ist ad hoc eingeführt und stützt sich nicht auf experimentelle Beobachtungen. Allerdings führen wir mittels dieser Aktivierung eine explizite Synchronisierung zwischen den Motoren innerhalb eines Teams ein, deren Stärke parametrisiert werden kann. Dieser Effekt ist vergleichbar mit der Mean-Field-Näherung in der Arbeit von Müller *et al*. Durch die Mean-Field-Annahme existiert eine perfekte Synchronisierung zwischen den Motoren eines Teams. Man findet heraus, dass im EPB-Modell eine starke Synchronisierung zusammen mit einer hohen Anzahl an Motoren notwendig ist, um Zustände mit SBDs zu erhalten. Es ist nicht zu erwarten, dass diese Situation biologisch relevant ist. Somit haben wir gezeigt, dass Zustände mit einer hohen Motilität ohne eine zusätzliche Regulierung von Seiten der Zelle nicht realisierbar sind. Dieses Resultat ist in einer Teilveröffentlichung [64] diskutiert.

Die oben beschrieben Situation gilt für zwei Teams von Motoren mit gleichen Eigenschaften. Im Allgemeinen, ist diese Situation nicht gegeben für intrazelluläre Transportprozesse. Dabei setzen sich die beiden Teams, die in entgegengesetzte Richtung ziehen, aus unterschiedlichen Motoren zusammen, wie im Abschnitt *Einführung in die Biologie des intrazellulären Transports* genauer erklärt wird. Im obigen Modell nimmt man an, dass die Abrissrate für beide Motorenarten exponentiell mit der Kraft wächst. Diese Beschreibung ist im Allgemeinen nicht ausreichend für realistische Motoren. Im Besonderen für Dynein hängt diese Rate von der Blockierkraft ab, denn für stärkere Kräfte zeigt Dynein ein interessantes Verhalten: Entgegen der Erwartung steigt die Abrissrate mit steigender Kraft nicht weiter an, sondern nimmt ab. Damit agiert Dynein wie ein Anker für einen Cargo, sobald große Kräfte auftreten. Dieses Verhalten wurde für Kinesin-Motoren nicht beobachtet. Wie im Abschnitt zur Biologie beschrieben, ändert sich das Verhalten der Motoren auch unterschiedlich mit der ATP-Konzentration. Aus diesem Grund ist es sinnvoll, diese für die Modellierung in Betracht zu ziehen. Sie ändert hierbei die Hüpfrate für beide Arten von Motoren in gleicher

Weise, jedoch ändert sich nur für Dynein der Betrag der Blockierkraft.

Beachtet man diese Unterschiede zwischen den Motoren, kann man Vorhersagen zur Cargodynamik in Abhängigkeit des zellulären Milieus machen. So kann man zum Beispiel die Zytoplasma-Viskosität oder die zelluläre ATP-Konzentration variieren. Für diese beiden Änderungen findet man überraschende Ergebnisse. Erhöht man die Viskosität, erwartet man lediglich eine Verlangsamung der Cargo-Bewegung. Im Rahmen des EPB-Modells wird allerdings für erhöhte Viskosität der Cargo-Bias umgekehrt, da die Motoren unterschiedlich auf diese erhöhte effektive äußere Kraft reagieren. Mit unseren gewählten Parametern und für mittlere ATP-Konzentrationen kehrt sich der Bias mit steigender Viskosität um, von einer überwiegend retrograden Bewegung für geringe Viskositäten zu einer überwiegend anterograden Bewegung mit steigender Viskosität. Ein ähnlicher Effekt wird für eine Variation der ATP-Konzentration beobachtet. Da molekulare Motoren genau ein ATP-Molekül benötigen, um einen Schritt zu machen, erwartet man, dass ein Absenken der ATP-Konzentration eine Reduktion der Cargo-Geschwindigkeit zur Folge hat. Allerdings ändert sich auch in diesem Fall entgegen der Erwartung die Bewegungsrichtung. Für geringe Konzentrationen entsteht ein negativer Bias, der zuerst mit steigender Konzentration verringert wird und schließlich in positive Richtung wieder anwächst. Interessanterweise ist nur für sehr wenige Parameterkonfigurationen kein globaler Bias zu sehen.

Es bleibt zu erwähnen, dass die ATP-Konzentration in den meisten Zellen räumlich konstant ist. Für das EPB-Modell ist sie nur ein Beispiel eines externer Parameters, der prinzipiell von der Zelle variiert werden kann. Entscheidend ist, dass die Motoren unterschiedlich auf die Änderung von Größen wie der Temperatur, der ATP-Konzentration, der Viskosität etc. reagieren. So treten Viskositätsvariationen auch dadurch auf, dass sich die transportierten Objekten in unterschiedlich dichten Regionen der Zelle bewegen. Daher darf man die Viskosität im Rahmen des EPB-Modells nicht als reine Viskosität des Zytosol sehen, sondern als generalisierte externe Kraft, wie sie zum Beispiel in sehr dichten Regionen der Zelle existiert. Die Effekte werden in einer Teilveröffentlichung [62] genauer diskutiert.

In *in vivo* Experimenten ist es nicht einfach Größen wie die Viskosität oder die ATP-Konzentration zu ändern. Manipuliert man eine der beiden Größen, kann man schnell die Zelle zerstören, da auch andere zelluläre Prozesse beeinflusst werden. Um nun trotzdem die mit dem EPB-Modell erzielten Resultate mit denen von *in vivo* Experimenten zu vergleichen, braucht man eine Messgröße, die keine Manipulation benötigt. Hierbei bietet sich die Änderung der mittlere quadratische Verschiebung der Cargo Position mit der Zeit an. Zum einen ist dies eine stabile Messgröße, die keine temporalen oder räumlichen Grenzwerte benötigt, um bestimmt zu werden. Zum anderen wurde sie schon für unterschiedliche Cargos in unterschiedlichen Zelle experimentell bestimmt [22, 71, 96]. Hierbei charakterisiert der Anstieg der mittleren quadratischen Verschiebung mit der Zeit die Bewegung. Ist dieser proportional zur Zeit, spricht man von einer diffusiven Bewegung. Für einen algebraischen Anstieg mit kleineren oder größeren Exponenten als 1 spricht man von anormaler Diffusi-

on. Man hat gemessen, dass sich der Cargo für sehr kurze Zeiten subdiffusiv, also mit einem Exponenten kleiner als eins, bewegt [71]. Für mittlere Zeiten tritt ein Übergang in ein superdiffusives Regime auf, charakterisiert durch einen Exponenten zwischen 1 und 2 [22]. Für größere Zeiten werden unterschiedliche Exponenten gemessen. Dies kann daran liegen, dass auf lange Sicht Netzwerkeffekte oder Dichteänderungen die Bewegung stark beeinflussen können. Beides tritt in der Definition des EPB-Modell nicht auf.

Mithilfe des EPB-Modells kann man die gemessenen Diffusionsregime reproduzieren und erklären. Das superdiffusive Regime tritt aufgrund einer persistenten Cargo-Bewegung auf. Bewegt sich ein Motor eines Teams, der unter Spannung steht, ändert sich die Kraft auf den Cargo. Dadurch vollführt dieser eine Bewegung in eben die Richtung des Motors, der einen Schritt gemacht hat. Dadurch steigt wiederum die Kraft auf die Motoren des entgegengesetzten Teams, während die Kraft auf die Motoren im gleichen Team abnimmt. Somit steigt die Wahrscheinlichkeit, dass ein Motor aus dem selben Team ebenfalls einen Schritt macht. Es entsteht eine positive Korrelation zwischen den Motoren, die superdiffusives Verhalten erzeugt. Die Korrelationszeit ist endlich und mit den von uns gewählten Parametern im Bereich von einer Sekunde. Misst man die mittlere quadratische Abweichung der Cargoposition für längere Zeiten als die Autokorrelationszeit, ist eine diffusive Bewegung zu beobachten. Um im Rahmen des EPB-Modells die Bewegung auf sehr kurzen Zeitsklalen zu untersuchen, müssen zusätzlich thermische Fluktuationen berücksichtigt werden. Diese erzeugen für die Cargo-Bewegung im Potential der Motorfedern eine subdiffusive Bewegung, die gut mit experimentell bestimmten Werten übereinstimmt [63, 71].

Wie bereits in der Einleitung erwähnt, muss bidirektionaler Transport stabil und effizient erfolgen. Aus diesem Grund sollte ein Cargo im EPB-Modell effizienter transportiert werden als dies durch reine Diffusion geschehen würde. Um die Effizient zu quantifizieren, beschränken wir das Filament räumlich, indem wir zwei hochviskose Barrieren links und rechts im gleichen Abstand vom Ursprung annehmen. Wir nehmen an, dass der Cargo sich zu Beginn der Simulation im Ursprung befinde. Gemessen wird nun die mittlere Zeit, die ein Cargo benötigt, um zum ersten Mal eine der Barrieren zu durchqueren. Hierbei unterscheiden wir zwei Szenarien: Der Cargo wird der entweder im Rahmen des EPB-Modells inklusive thermischer Fluktuationen oder aber rein durch thermische Fluktuationen propagiert. Für geringe Barrierenviskositäten und -längen ist reine Diffusion effizienter und somit ausreichend für intrazellulären Transport. Erhöht man nun allerdings die Barrierenlänge oder die Viskosität ist es notwendig, dass der Cargo aktiv transportiert wird. Diese Effekte werden in einer Teilveröffentlichung [63] diskutiert.

## Kollektive Effekte

Im Normalfall sind viele zu transportierenden Cargos entlang eines einzelnen Mikrotubulus gebunden. Im Modell der zellulären Automaten wurde bereits offensichtlich, dass dadurch

kollektive Effekte durch pure sterische Wechselwirkung auftreten. Mithilfe des EPB-Modells konnte gezeigt werden, dass Cargos, die von zwei Teams von molekularen Motoren gezogen werden, ganz automatisch immer wieder ihre Bewegungsrichtung ändern. Im Folgenden soll eine vereinfachte Beschreibung eingeführt werden, die die essentiellen Charakteristiken der Bewegung eines Cargos im EPB-Modell erfasst. Dazu entwickeln wir Teilchen, die sich wie ein gewöhnlicher Random Walker verhalten, allerdings mit sich zeitlich ändernden internen Zuständen. Für jeden Zustand existiert ein Paar von Hüpfraten, jeweils für einen Schritt nach links oder rechts. Die Ratenpaare sind so gewählt, dass zwei der Zustände einer langsamen und einer schnellen Diffusion entsprechen und zwei weitere einen Bias nach rechts oder nach links aufweisen. Mittels dieser Beschreibung finden wir eine gute Übereinstimmung für die Richtungsänderungszeitverteilung mit dem EPB-Modell.

Um nun die auftretenden kollektiven Effekte zu bestimmen, werden $N$ dieser Teilchen auf ein periodisches Gitter der Länge $L$ gesetzt. Entlang des Gitters herrscht das Exklusionsprinzip, sodass ein einzelner Gitterplatz entweder leer oder mit genau einem Teilchen besetzt sein kann. Mit einer geschickten Wahl der Übergangsraten zwischen den einzelnen Zuständen kann das Modell von einem System im Teilchenbild auf ein System im Abstandsbild abgebildet werden. Die sich zeitlich ändernde Hüpfrate aufgrund der inneren Zustände kann als Signatur einer teilchenweisen Unordnung im Rahmen von Exklusionsmodellen interpretiert werden. Aufgrund dieser findet man für geringe Dichten eine Teilchenkondensation, während für größere Dichten die Geschwindigkeit der Teilchen nur noch von der Dichte und nicht mehr von der Unordnung abhängt.

## Schlussfolgerung und Ausblick

Während meiner Promotion wurden drei Modelle entwickelt, die mit unterschiedlichen Transportszenarien zu assoziieren sind. Hierbei lag der Schwerpunkt auf der generellen Modellierung, ohne spezielle Berücksichtigung der Geometrie, und wurde im Rahmen des EPB-Modells analysiert. Das EPB-Modell beschreibt den Transport eines Cargos durch zwei Teams von molekularen Motoren. Diese beiden Teams sind nur über ihre Verbindung zum Cargo miteinander gekoppelt. Die einzelnen Motoren können diskrete Schritte entlang des Mikrotubulus, ein eindimensionales, unendlich langes Gitter, vollführen. Mittels dieser Schritte wächst der Abstand der Motordomäne zum Cargo, was einem Anstieg der Kraft entspricht.

Ich habe zwei Versionen dieses Modells untersucht: Zum einen mit Motoren, die abgesehen von der Bewegungsrichtung die gleichen Eigenschaften haben, zum anderen mit Motoreigenschaften, die experimentelle Befunde über die beiden Motortypen widerspiegeln. Im symmetrischen Fall ist das wichtigste Ergebnis, dass Zustände mit SBDs nur in einer Mean-Field-Näherung existieren und dadurch eine explizite Synchronisation zwischen den Motoren eines Teams voraussetzen. Für eine solche Synchronisierung gibt es bisher keine

experimentelle Evidenz.

Im Fall asymmetrischer Motoren ist es mit dem EPB-Modell möglich, Vorhersagen über die Bewegungscharakteristik eines Cargos unter Einfluss des zellulären Milieus zu machen. Hier wurde gezeigt, dass es in *in vivo* Experimenten von großer Bedeutung ist die Umgebung zu berücksichtigen, wenn die Trajektorien analysiert und interpretiert werden. Im Allgemeinen ist der Bias eines Cargos nicht verschwindend, sondern in einer der beiden möglichen Bewegungsrichtungen deutlich ausgeprägt. Dies ist vor allem dann wichtig, wenn man die mittlere quadratische Verschiebung berechnet. Hierbei kann ein globaler Bias schnell als anormale Diffusion gedeutet werden.

Zusammenfassend kann man sagen, dass das zelluläre Milieu von essentieller Bedeutung ist, wenn man bidirektionalen Cargo-Transport modelliert. Schon einfach Änderungen können hierbei große und unerwartete Effekte erzielen - wie zum Beispiel eine Umkehrung der Bewegungsrichtung. Aus diesem Grund ist es außerordentlich wichtig, dass in naher Zukunft *in vitro* Experimente gemacht werden, die unter kontrollierten Bedingungen ablaufen. Hierbei sollte zum einen die Charakteristik der Motoren genau bekannt sein und auch das Medium, in dem sich ein möglicher Cargo bewegen würde. Für lange Zeit waren solche Experimente nicht möglich, da es keinen Mechanismus gab, um Dyneine von Säugetieren in einer prozessiven Weise in *in vitro* zu untersuchen. Lediglich Experimente mit Dynein aus Hefe und Kinesin von Säugetieren wurden bisher durchgeführt - diese Kombination von Motorproteinen kommt in realen Zellen nicht vor. Vor nun etwa zwei Jahren gab es jedoch einen Durchbruch für *in vitro* Experimente mit Säugetier-Dynein [84]. Experimentelle Ergebnisse sind in naher Zukunft zu erwarten [48].

Die beiden weiteren Modelle, die in dieser Arbeit analysiert wurden, zielen darauf ab kollektive Effekte zu analysieren. Diese entstehen durch die Interaktion mehrerer Teilchen, die sich stochastisch entlang eines Gitters unter Annahme einer Hardcore-Wechselwirkung bewegen. Dadurch kann immer nur maximal ein Teilchen pro Gitterplatz existieren. Eines dieser Modelle ist eine effektive Beschreibung mehrerer Cargos, wie sie sich im EPB-Modell bewegen. Um die komplexe Bewegung zu modellieren, haben die Teilchen vier unterschiedliche interne Zustände, die die Hüpfraten definieren. Analysiert man dieses Modell in einer Mean-Field-Näherung, beobachtet man eine dichteabhängige Kondensation entlang des Gitters. Die unterschiedlichen Hüpfraten kann man hierbei als zeitabhängige Unordnung interpretieren.

Des Weiteren wurde ein Modell definiert, das durch eine Arbeit von Lin *et al.* [79] inspiriert wurde. Das Gitter ist hierbei zweispurig, wobei an einem Ende offene und am anderen reflektierende Randbedingungen angenommen werden. Entlang dieses Gitters bewegen sich zwei Teilchenarten, die sich zum einem in ihrer Bewegungsrichtung zum anderen im Spurwechselverhalten unterscheiden. Mithilfe dieser Asymmetrie ist es möglich durch Variation der Parameter einen Phasenübergang von einer Niedrigdichtephase zu einer Phase mit sich periodisch ändernder Dichte zu beobachten. Diese periodische Phase zeigt nicht-

lineares Verhalten, was sich unter anderem in nicht-sinusoidale Dichteoszillationen niederschlägt. Wir sind in der Lage mehrere Effekte analytisch zu erklären, unter anderem Dichteoszillationen in der Hochdichteregion oder das Dichteprofil in der Niedrigdichtephase. In diesem Modell bleiben allerdings noch einige Fragen offen, die es zu erklären gilt.

# Résumé substantiel

## Introduction

Beaucoup de processus que l'on observe dans la vie quotidienne, comme par exemple la circulation routière ou piétonne [24,51,87,98], les essaims d'animaux [26] ou même les fonctions essentielles dans notre propre corps [23,47,107], présentent des caractéristiques fascinantes. Mêmes si ces exemples sont bien différents au premier coup d'œil ils font partie de la même classe de physique. Tous ces phénomènes se rapportent aux systèmes hors équilibre. Pour les exemples susmentionnés cet état de non-équilibre existe parce que les particules sont actives et autopropulsées. Alors que pour les systèmes en équilibre une théorie générale existe pour obtenir la probabilité d'un micro-état, elle n'existe pas pour les systèmes hors équilibre. Le sujet de cette thèse est en général l'application des outils de la physique statistique au transport intracellulaire. Ce transport est un exemple révélateur de processus hors équilibre qui, comme la plupart des processus intracellulaires, est seulement réalisable par la conversion d'énergie chimique en énergie mécanique.

Dans une cellule saine le transport est essentiel. Plusieurs études indiquent que les maladies neurodégénératives comme la maladie d'Alzheimer ou de Parkinson sont reliées à un transport perturbé et un gonflement de cellule [28]. Pour établir un transport stable une cellule construit un réseau de protéines le long desquels les moteurs moléculaires transportent des vésicules et organelles.

Dans ce que suit je discuterai deux approches différentes pour modéliser le transport intracellulaire. D'un coté j'utiliserai un modèle explicite qui prend en considération les degrés de liberté internes comme ils ont été déterminés expérimentalement. D'un autre coté j'analyserai phénoménologiquement les effets collectifs au moyen de processus d'exclusion.

### Les bases biologiques

Dans une cellule un réseau de fibres de protéines permet le transport intracellulaire. Dans cette thèse la priorité est donnée au transport le long des microtubules. Microtubules sont des fibres qui se composent de treize protofilaments formés de dimères de tubuline. Ces protofilaments s'assemblent en un tube pour former la microtubule. La formation des microtubules commence à partir du centrosome et cette extrémité, dénommée extrémité $(-)$,

de la microtubule est très stable. En assemblant les dimères le microtubule grandit vers la membrane cellulaire. Cette extrémité $(+)$ par contraste est très dynamique et peut basculer entre deux états croissant ou rétrécissant. Les transitions entre ces deux états s'appellent catastrophe (passage d'un état croissant à rétrécissant) et sauvetage (transition inverse). On dit qu'une microtubule présente une instabilité dynamique.

Il est important de noter qu'il y a deux types de tubuline : la tubuline $\alpha$ et $\beta$. Grâce à ces deux types, les microtubules sont polarisées. La polarisation est utilisée par les moteurs moléculaires pour déterminer la direction. Un moteur moléculaire est une protéine qui peut marcher le long d'une microtubule. Ce déplacement est stochastique et les moteurs peuvent aussi se détacher du filament. La distance parcourue le long du filament entre deux événements d'attachement/détachement caractérise la processivité du moteur. Dans les cellules eucaryotes deux types différents de moteurs existent qui se distinguent par la direction de mouvement. En général les moteurs de la famille des kinésines marchent dans la direction de l'extrémité $(+)$ tandis que les dynéines cytoplasmiques marchent vers l'extrémité $(-)$. On dit que le mouvement des kinésines est anterograde et celui des dynéines est rétrograde. Mais la direction de mouvement n'est pas la seule différence entre les deux types de moteurs. Ils réagissent aussi d'une manière différente aux signaux externes. Par exemple on peut prendre en considération la concentration d'adénosine-5'-triphosphate (ATP). L'ATP est une molécule qui est cruciale pour tous les organisme vivants car elle alimente tous les processus cellulaires actifs en énergie. Les moteurs moléculaires ont besoin d'une molécule d'ATP exactement pour faire un pas le long de microtubule. Il a été observé qu'il est possible de trouver une relation entre le taux de saut du moteur, la force exercée sur le moteur et la concentration d'ATP, sous la forme d'une fonction de type de Michaelis-Menten qui est une fonction croissante mais qui sature pour les valeurs hautes de la concentration d'ATP [100]. Il est intéressant de noter que cette relation peut être utilisée pour la kinésine ainsi que pour la dynéine [116]. En outre, la concentration d'ATP a également un effet sur la force d'arrêt nécessaire pour stopper un moteur de dynéine. Cette force d'arrêt augmente de 0.3 pN à 1.3 pN de façon linéaire avec cette concentration jusqu'à une concentration de saturation à 1 mM environ [82]. Au contraire, la force pour stopper un moteur de kinésine est constante et n'est pas influencée par la concentration d'ATP.

La situation est un peu différente dans les neurones - cellule nerveuse -, mais aussi pour les cellules de champignons filamenteux. Pour ces cellules très fines et longues on trouve que l'arrangement des microtubules est parallèle. Dans cette thèse plusieurs géométries seront considérées, avec des conditions aux limites ouvertes où fermées. Le problème principal pour le transport intracellulaire est donné par le fait que les deux équipes de moteurs moléculaires utilisent la même voie. On pourrait naïvement en déduire que la situation est fortement embouteillée facilement. Néanmoins, le trafic intracellulaire, même bidirectionnel est observé être très stable dans une cellule saine.

### Modèles d'automates cellulaires

Ces dernières années plusieurs modèles basés sur des automates cellulaires ont été utilisé pour la modélisation de transport intracellulaire. Un modèle simple est le processus d'exclusion asymétrique. Il est réalisé par un gaz sur réseau, évoluant sur un réseau unidimensionnel de $L$ sites. Sur ce réseau discret un ensemble de particules se déplace aléatoirement avec une particule maximale par site. Chaque particule peut sauter d'un site à l'autre le long du réseau tant que le site voisin est vacant. Pour modéliser le transport bidirectionnel il faut qu'en fait les particules puissent sauter dans les deux directions. Souvent cela est réalisé en considérant deux populations dont l'une saute à gauche et l'autre à droite. Sans règles supplémentaires il est évident qu'aucun flux de particules n'est possible, les particules de différents types ne pouvant pas se croiser.

Nous avons développé un modèle dans lequel on permet une transformation des particules qui sautent à droite (plus) en particules qui sautent à gauche (minus). En plus, nous considérons une deuxième voie pour que les particules puissent se dépasser. Un modèle similaire mais plus compliqué était introduit par Lin *et al.* [79] pour modéliser le transport bidirectionnel dans les cellules de champignons filamenteux. Ils ont trouvé que pour une grande gamme de paramètres le système présente une phase de pulsation si ils supposent que la limite à gauche est ouverte et l'une à droite est réfléchissante. Avec ces conditions aux limites les plus particules sont introduites à gauche et sautent vers la limite réfléchissante. Le long du réseau les particules peuvent se transformer - ce qui veut dire qu'elles peuvent changer leur direction de saut. Pour empêcher une situation embouteillée les particules peuvent changer de voie chaque fois que le site voisin est déjà occupé par une autre particule. Le modèle de Lin *et al.* est formulé très généralement. Nous nous sommes intéressés à déterminer quels sont les ingrédients minimaux pour obtenir une phase de pulsation. On trouve qu'il suffit de prendre deux voies en considération mais qu'il est nécessaire d'introduire une asymétrie entre les deux types de particules. Dans notre modèle par exemple nous avons choisi de permettre seulement aux minus particules à changer de voie. Ces règles dynamiques permettent un flux périodique stable. On observe que le système se remplit rapidement alors qu'il se vide très lentement. Dans cette phase le système est divisé en une région avec une densité de particules d'environ un alors que l'autre moitié du système près de l'extrémité réfléchissante est presque vide avec une densité d'environ zéro. Avec une analyse qui s'appuie sur la conservation de la matière totale on peut estimer la vitesse d'évacuation des particules. En plus on observe que le flux des minus particules est le double de celui des plus particules. On explique ce résultat analytiquement en supposant que les deux densités sont $1/2$ moins une valeur très petite.

En plus on trouve plusieurs effets mystérieux lorsqu'on réalise une intégration numérique des équations d'évolution. Dans la région de haute densité on observe des oscillations spatiales près de la position du choc qui décroissent exponentiellement mais avec une valeur constante pour la somme des deux densités. Dans la région de densité basse on trouve

a contrario des oscillations temporelles. Elles sont reliées au mouvement du choc sur un site de réseau. Afin de comprendre comment ces oscillations temporelles et spatiales se constituent on peut faire une analyse de stabilité. On suppose des perturbations petites en espace et temps dans l'esprit de Evans *et al.* [39]. On trouve que les solutions sont stables en temps. Contrairement, en considérant une perturbation en espace on trouve que pour une valeur de la densité donnée trois racines complexes apparaissent avec une valeur absolue plus grande que un. Donc, une instabilité spatiale existe qui produit des oscillations dans la région de haute densité.

En fonction des paramètres on peut trouver une deuxième phase qui est caractérisée par une densité basse pour les deux espèces. En ce cas la transformation de type des particules est suffisamment rapide comparé à l'introduction des particules à l'entrée. Au moyen du développement en série de Taylor des équations dynamiques on trouve des expressions exactes pour les profils de densités dans cette phase de densité basse. Le modèle sera discuté plus en détail dans notre publication en préparation [61]. Il faut remarquer que ce modèle est plus intéressant d'un point de vue de physicien que pour modéliser le transport intracellulaire de façon réaliste.

### EPB-model

Pour modéliser le transport bidirectionnel j'analyse un deuxième modèle plus détaillé dans cette thèse. Le centre d'attention pour ce projet est de comprendre la dynamique d'une particule transportée par des équipes de moteurs moléculaires. Dans plusieurs cellules différentes il a été observé qu'une particule, comme par exemple une vésicule, change de direction plusieurs fois. Pas mal de chercheurs essaient expliquer ce phénomène. Une expérience avec des endosomes dans des cellules de *Dictyostelium* a montré que les endosomes sont allongés chaque fois qu'ils changent de direction de mouvement. Cela prouve que deux forces opposées sont exercées au même temps. Entre autres, cette observation justifie une classe de modèles qui suppose que deux équipes de moteurs sont attachées à la particule transportée au même temps. Un modèle très populaire a été introduit par Müller *et al.* [86]. Ils proposent de considérer qu'il n'est pas important de savoir explicitement où sur le filament est attaché chaque moteur, mais qu'il suffit de prendre en compte le nombre de moteurs attachés par équipe. Ce nombre change en fonction de la force qui est exercée par l'autre équipe. En supposant que les moteurs dans une équipe partagent la force également il est possible de déterminer la vitesse de la particule transportée. Chaque moteur qui est détaché peux se rattacher avec un taux constant. On peut voir ces hypothèses comme un modèle de champ moyen. Avec ces hypothèses, Müller *et al.* trouvent trois états de motilité différents dépendant des paramètres choisis. Un de ces trois états comporte un intérêt particulier : il est caractérisé par une distribution de la vitesse et du nombre de moteurs attachés bimodale. Contre toute attente la configuration avec seulement une équipe attachée est très stable et domine la dynamique du système. Dans cette situation la particule est déplacée en moyenne

avec la vitesse de moteurs ne subissant pas de force.

Nous nous sommes posé la question de l'existence de cet état dans un modèle plus pertinent biologiquement. Pour cette raison un modèle qui prend en compte explicitement la position de chaque moteur est introduit dans cette thèse, que nous avons appelé EPB-modèle (*explicit position-based* - dépendant de la position explicitement). Dans notre modèle les moteurs peuvent faire des pas le long du réseau et la force exercée est modélisée comme un ressort linéaire donc linéaire en distance entre moteur et particule. Avec cette hypothèse notre modèle capture les fluctuations de position des moteurs. Les simulations de Monte Carlo d'EPB-modèle montrent que ces fluctuations sont cruciales pour déterminer la dynamique de la particule transportée. En comparant nos résultats numériques pour la distribution de la vitesse avec ceux trouvés avec le modèle de champ moyen il devient évident que les fluctuations de position détruisent la structure bimodale. Cet idée de modélisation explicite est introduit dans notre publication [65].

Afin de déterminer les conditions nécessaires pour obtenir une distribution bimodale nous introduisons une activation mutuelle entre les moteurs d'une même équipe. Cette activation introduit un facteur multiplicatif constant pour le taux de saut de chaque moteur dans un certain rayon autour du moteur qui a fait un pas. Notez que cette définition de l'activation est arbitraire et n'est pas supposée exister dans un système biologique. Mais grâce à cette activation nous introduisons une synchronisation effective entre les moteurs d'une même équipe. Cet effet est comparable à une description de champ moyen où les moteurs bougent tout de façon synchrone. Nous trouvons qu'une activation très forte avec un grand nombre de moteurs est nécessaire pour retrouver une distribution de vitesse bimodale. Cette situation n'est pas considérée être pertinente pour décrire la situation dans une vraie cellule. Donc nous avons montré que les états de motilité avec des distributions bimodales ne sont pas réalistes pour le transport intracellulaire. Ces résultats sont discutés en plus détail dans notre publication [64].

La situation mentionnée ci-dessus décrit le mouvement d'une particule transportée par des équipes de moteurs avec des propriétés symétriques. En général, ce n'est pas le cas dans une cellule. Normalement, les deux équipes de moteurs ont des caractéristiques bien différentes. Dans le modèle décrit ci-dessus le taux de détachement est exponentiel en la force exercée. En fait cette description n'est pas suffisante. En particulier pour la dynéine, le taux augmente exponentiellement mais seulement jusqu'à une force particulière : la force d'arrêt nécessaire pour stopper un moteur. Pour une force plus forte on observe une baisse du taux. Ce comportement n'est pas observé pour les moteurs de la famille des kinésines. Comme décrit dans le chapitre sur la biologie les deux types de moteurs réagissent d'une manière différente à la concentration d'ATP. Il est donc raisonnable de prendre la concentration d'ATP en considération dans notre modèle. Elle change le taux de saut pour les deux types de moteurs d'une manière identique mais elle influence la force d'arrêt des dynéines seulement.

En considérant ces différences entre les deux types de moteurs on peut faire des prédictions de mouvement dans des circonstances différentes d'environnement. On peut par exemple varier la viscosité du cytosol ou la concentration d'ATP. Pour les deux on trouve une modification du mouvement bien surprenante. Si la viscosité est modifiée on s'attend à ce que le mouvement soit simplement ralenti. Mais pour une particule transportée par deux équipes de moteurs on n'observe pas seulement un ralentissement mais une inversion du biais général du mouvement. En considérant ces propriétés des moteurs moléculaires on peut changer le biais de la particule. Avec notre choix de paramètres de simulation on trouve que le biais est vers l'extrémité (+) de la microtubule mais qu'il s'inverse lorsque la concentration d'ATP augmente. Les deux équipes s'équilibrent seulement pour un ensemble de paramètres très particulier, ce qui résulte en une situation sans biais global.

Il faut remarquer que la concentration d'ATP est apparemment plus ou moins constante dans une cellule. Par contre elle pourrait être modifiée dans des expériences in vitro. Dans le cadre du EPB-modèle il est facile de changer ce paramètre, d'autant plus qu'on dispose de résultats bien vérifiés sur la réponse des deux types de moteurs à un changement de la concentration d'ATP. On pourrait de même changer un autre facteur externe qui influence le comportement des moteurs d'une façon similaire.

Dans le cadre de cette thèse j'ai aussi analysé comment la viscosité influence le comportement de la particule transportée. On peut voir cette viscosité comme une viscosité effective résultant de la structure spatiale à l'intérieur d'une cellule. L'environnement cellulaire est très bondé - un réseau de structures élastiques passe dans tout l'intérieur. Ces structures peuvent gêner la particule, voire marcher de façon similaire à un piège. A l'inverse de la concentration d'ATP qui influence directement le comportement des moteurs l'effet d'un changement de la viscosité est indirect. La particule obéit à son equation du mouvement dans laquelle le terme de frottement est proportionnel à la viscosité. Avec cette définition on peut comprendre qu'une augmentation de la viscosité correspond à une force plus forte. On s'attend à ce que dans ce cas le mouvement de la particule soit simplement ralenti. Mais au contraire, on observe que le biais vers l'extrémité (+) augmente avec la viscosité dans un environnement avec une concentration d'ATP basse. De plus, pour une concentration intermédiaire le biais est effectivement inversé en commençant par un biais négatif pour une viscosité basse en passer à un biais positif pour une viscosité assez grande. Cet effet apparait en raison des réactions différentes des moteurs à une force exercée.

Dans une expérience *in vivo* il n'est pas facile de changer la viscosité ou en général une force homogène, et pas non plus la concentration d'ATP. Les deux manipulations peuvent détruire la cellule. Pour comparer quand même l'EPB-modèle à des résultats d'expériences *in vivo* on peut analyser le déplacement quadratique moyen d'une particule. Cette mesure est très stable car elle ne fait pas intervenir de seuil ni temporel ni spatial. En plus il y a plusieurs résultats expérimentaux disponibles à comparer avec nos résultats numériques. L'augmentation du déplacement quadratique moyen avec le temps permet de caractériser

le mouvement : Si l'augmentation est linéaire en temps le déplacement est diffusif. Pour un comportement qui croît de façon plus ou moins rapide que linéaire en temps on dit que la trajectoire présente une diffusion anormale. Dans les expériences *in vivo* on a trouvé que le caractère du mouvement change avec le temps. Pour les temps courts le comportement est subdiffusif donc le déplacement quadratique moyen croît de façon moins rapide que linéaire en temps. Pour les temps plus longs on observe une transition vers un comportement superdiffusif qui est caractérisé par une croissance plus rapide que linéaire en temps. Pour les temps plus longs que plusieurs minutes le caractère est fortement dépendent de la particule considérée. Une particule pourrait être captive dans une région cellulaire qui est très bondée ou en raison du réseau de filaments changer de direction bien que les même moteurs restent actifs. Ces effets sont exclus dans l'EPB-modèle puisque le réseau est unidimensionnel et il n'y a aucun empêchement stérique. Pour plus de détails veuillez-vous lire notre publication [62].

Avec notre modèle on trouve que le déplacement quadratique moyen croît de façon plus rapide que linéaire pour un intervalle temporel de moins d'une seconde environ. Au delà on trouve une transition vers un état purement diffusif. Pour aussi trouver la croissance subdiffusive pour les temps très courts il faut introduire une force aléatoire qui représente les fluctuations thermiques.

Ces trois régimes sont facile à expliquer dans l'EPB-modèle : La phase subdiffusive est une combinaison de mouvement thermique qui est par définition diffusif et du potentiel quadratique dû aux moteurs. L'interaction des deux résulte en une croissance sublinéaire en temps. Pour les temps plus longs le jeu collectif des moteurs crée une persistance : si un moteur qui sent une force fait un pas la particule transportée suit. Ainsi la force exercée par les moteurs de la même équipe est réduite alors que la force est plus élevée sur l'autre équipe. Donc la probabilité que le mouvement se continue dans la même direction est plus élevée. Cette autocorrélation positive produit un comportement superdiffusif. Pour les temps plus longs que le temps d'autocorrélation le mouvement est naturellement diffusif.

Dans l'introduction j'ai mentionné que le transport bidirectionnel doit être stable et efficace. Pour cette raison il faut analyser si l'EPB-modèle est plus efficace qu'une pure diffusion. Donc nous restreindrons le filament spatialement en introduisant deux barrières visqueuses. La particule est placée à l'origine au début de la simulation et ensuite elle est déplacée en prenant les fluctuations thermiques en considération. Pour mesurer l'efficacité on calcule la valeur moyenne du temps écoulé avant la première visite au point derrière la barrière, d'une part pour les particules transportées par deux équipes de moteurs et d'autre part pour celles qui bougent de façon purement diffusive. On trouve que pour les distances courtes la diffusion des particules est complètement suffisante et en fait en considérant une viscosité basse la diffusion est plus efficace. Mais dès que la taille de la barrière à traverser atteint une valeur de taille d'organelle ou plus longue, le transport actif par moteurs est nécessaire. Veuillez trouver une description plus détaillée dans notre publication [63].

En concluant on voit que l'environnement est très important pour décrire le mouvement d'une particule. Des facteurs externes très simples peuvent changer le comportement complètement et même inverser le biais global du déplacement. Pour cette raison il est nécessaire qu'on fasse une expérience *in vitro* avec une particule tirée par deux équipes de moteurs bien caractérisés et avec un environnement qui ne change pas avec le temps. Les expériences de ce type n'étaient pas possibles jusqu'à récemment car la dynéine de mammifère ne marchait pas d'une façon processive *in vitro*. De ce fait on ne pouvait utiliser que des particules transportées par une équipe de kinésines de mammifère et une équipe de dynéines de levure - une combinaison qui n'est jamais trouvée dans la nature. Il y a deux ans, on a trouvé un mécanisme pour produire une dynéine de mammifère processive. Donc espérons que bientôt les résultats *in vitro* seront disponibles.

### Mouvement collectif

Comme on a compris le mécanisme de transport de particules intracellulaires le prochain pas est de comprendre les effets de mouvement collectif. J'ai déjà décrit que normalement une cellule est très encombrée. De plus on a seulement une seule voie de transport pour des particules qui peuvent marcher dans les deux directions. On peut le voir comme une rue à sens unique avec des voitures qui veulent conduire dans les deux sens. Si les voitures ne peuvent pas faire demi-tour la rue est bouchée rapidement. Il y a au moins deux mécanismes différents qui peuvent empêcher ce scénario : ou bien la rue a plusieurs voies et donc les voitures peuvent se dépasser, ou bien les voitures peuvent faire demi-tour et donc créent des flux périodiques vers les deux côtés.

Les particules qui sont transportées par plusieurs moteurs différents peuvent changer de direction de mouvement sur la base de détachements et réattachements de moteurs. Mais l'effort de simulation pour un système de particules qui prend chaque moteur en considération est énorme. Donc il faut trouver une description effective qui sauvegarde la caractéristique du mouvement d'une particule qui est transportée par deux équipes de moteurs. Dans ma thèse cette idée est réalisée en prenant des particules qui ont quatre états internes différents qui sont caractérisés par une paire de taux de saut vers la gauche et vers la droite. Dans deux de ces états les particules bougent diffusivement mais avec deux taux différents dans les deux états. Dans les deux autres états la particule a un biais effectif vers la gauche ou la droite. Les transitions d'états sont choisies de telle sorte que seulement un seul taux change. Les distributions de temps de changement de direction de déplacement pour l'EPB-modèle et pour le modèle décrit ici sont en très bon accord. Aussi on peut trouver une approximation analytique pour cette distribution.

En mettant plusieurs particules avec états internes sur un réseau on peut examiner les effets collectifs. Il y a eu plusieurs articles ces dernières années qui traitent des modèles de processus d'exclusion. Si on suppose que le taux de saut de particules est désordonné on trouve qu'un effet de condensation apparaît souvent si la densité de particules est relative-

ment basse, un effet qui est comparable à la condensation de Bose-Einstein [38]. Dès que la densité dépasse une valeur typique une transition de phase se produit vers une phase de haute densité. Normalement, ces problèmes sont étudiés en supposant que les corrélations de densité entre un site et son voisin sont (presque) zero et donc on utilise une approximation de champ moyen. Afin de déterminer si une transition de phase existe il est commode de choisir la représentation la distance. Au lieu d'utiliser la position de la particule sur le réseau on choisit la distance à la prochaine particule comme variable. Dans ce cadre de représentation les sites vacants sont les particules sur un réseau auxiliaire. Notez que la direction de saut d'une particule dans le processus original est inversée dans la représentation de distance. On analysera le modèle dans un cadre d'approximation champ moyen et aussi numériquement par des simulations de Monte Carlo.

Donc nous sommes intéressés à savoir si une transition de phase existe aussi pour notre modèle. Par une intégration numérique des équations maîtresses on trouve qu'effectivement une condensation de particules se forme. Quand la densité de particules augmente cet effet disparaît. Dans le schéma fondamental on observe facilement que des corrélations entre les particules dans des états différents existe. Pour la simulation de Monte Carlo le flux s'écarte des résultats connus pour un processus d'exclusion simple (SSEP) pour toutes densités. Par contraste, pour les densités basse on trouve le même résultat pour le modèle de champ moyen et le modèle de réseau explicite. Mais si la densité augmente, le flux dans le modèle de champ moyen s'approche des résultats obtenus pour le SSEP.

### Conclusions et développements futurs

Durant mon doctorat j'ai développé trois modèles différents qui représentent des situations différentes mais qui sont toutes associées au transport intracellulaire. Le modèle le mieux analysé dans cette thèse est l'EPB-modèle. Il prend en considération deux équipes de moteurs qui n'interagissent pas directement mais qui sont amarrés à une même particule. Les moteurs eux-mêmes font des pas sur la microtubule, un réseau discret et unidimensionnel. En faisant des pas en directions opposées les deux équipes s'éloignent l'une de l'autre et donc une force s'instaure. Dans cette thèse j'ai analysé deux situations différentes dans le cadre de ce modèle. En premier, j'ai examiné un ensemble de deux équipes symétriques. Dans ce cas le plus important a été de montrer que les états de motilité qui produisent des distributions bimodales n'existent plus si on relâche les hypothèses de champ moyen. J'ai montré qu'une synchronisation forte est nécessaire pour les retrouver - si forte qu'elle n'est pas pertinente pour une modélisation réaliste biologique.

Avec notre EPB-modèle il est aussi possible de faire des prédictions pour un changement des conditions externes. J'ai montré qu'il est crucial pour les expériences *in vivo* de prendre l'environnement en considération si on analyse des trajectoires de particules intracellulaires. En particulier le biais d'une particule est rarement zero mais le plus souvent un biais général du mouvement est observé. Ce fait est important surtout si l'on calcule le déplacement

quadratique moyen : un biais peut alors facilement être pris pour une diffusion anormale.

Les deux autres modèles que j'ai analysés se concentrent plus sur les effets collectifs. Dans les deux cas on considère un modèle d'automate cellulaire, ce qui veut dire qu'on a un réseau discret de longueur $L$ sur lequel $N$ particules peuvent se déplacer d'un nœud à un nœud voisin à la condition que celui-ci ne comporte pas de particule.

Le premier modèle de gaz sur réseau est déterminé dans l'intention d'étudier les effets collectifs pour des particules qui ont les mêmes caractéristiques de mouvement qu'un cargo dans l'EPB-modèle. Comme il est très astreignant de faire des simulations numériques pour plusieurs particules dans un cadre d'EPB-modèle on a défini un modèle effectif. Les caractéristiques sont implémentés en introduisant des états internes pour les particules. Pour chaque état une paire de taux de saut est définie et l'état change aléatoirement. Avec les règles pour les transitions entre les états les transitions sont indépendantes et donc la projection de la représentation de distance est exacte. Donc on peut calculer la distribution de sites vacants entre deux particules le long du réseau. On observe une condensation de particules pour les densités basses. Cette condensation se produit parce que la transition entre états joue comme un désordre de taux. Cet effet devient évident en mesurant la vitesse des particules en fonction de la densité. Pour le processus d'exclusion simple la vitesse décroit de manière linéaire quand la densité augmente au contraire du modèle avec les états internes.

L'autre des deux modèles comporte deux voies avec une condition aux limites ouverte et l'autre réfléchissante, donc une structure tubulaire. Le long de ce réseau deux types de particules bougent vers la gauche ou vers la droite selon leur type actuel. En introduisant une asymétrie entre les deux types par rapport à leur comportement de changement de voies on observe une transition de phase d'une phase de densité basse à une phase de pulsation de la densité. Dans cette phase le réseau se remplit vite. Mais ensuite une région de densité basse se forme à proximité de la limite réfléchissante. En supposant que la masse est conservée on peut prédire la vitesse de vidange approximativement. En plus, par une analyse de stabilité on comprend la structure le long du réseau dans la région de haute densité. En considérant une perturbation spatiale on trouve une augmentation exponentielle de la densité près du choc et aussi des oscillations de densité. La phase de pulsation est gouvernée par un comportement fortement non-linéaire. Cela devient évident lorsqu'on analyse les oscillations de densité dans la région de basse densité. On peut prédire plusieurs effets mais il reste encore des questions ouvertes.

Pour les développements futurs il est nécessaire que des expériences avec deux équipes de moteurs soient réalisées *in vitro*. Ces expériences pourraient montrer le comportement de moteurs sans influence de l'environnement ou d'un bouchon le long de la microtubule. Avec notre EPB-modèle il est possible de faire des prédictions pour ce transport bidirectionnel intracellulaire pur. En plus, si on comprend des effets bidirectionnels on pourrait complexifier pas à pas l'environnement, en commençant avec des microtubules décorées ou

un changement de conditions externes.

Du coté théorique il faut qu'on comprenne les effets des états internes plus en détail. Le prochain pas serait de résoudre analytiquement l'équation de la densité de probabilité pour trouver une distance $d$ entre deux particules. Cette densité pourrait donner des éclaircissements sur les conditions dans lesquelles le système présente un état embouteillé. En sachant quels ingrédients produisent un bouchon de particules intracellulaires on pourrait comprendre comment les maladies neurodégénératives se constituent et comment on peut les traiter.

# Contents

# Table des matières

# Nomenclature

| | | |
|---|---|---|
| $\mathcal{C}$ | configuration | 30 |
| $\eta$ | medium's viscosity | 51 |
| $\mathcal{K}$ | motor stiffness | 50 |
| $\tau_i$ | occupation variable at site $i$ | 31 |
| $a$ | activation factor | 54 |
| $d$ | motor step length | 51 |
| $F_D$ | detachment force | 48 |
| $F_S$ | stall force | 47 |
| $k_a$ | attachment rate | 48 |
| $k_B$ | Boltzmann constant | 29 |
| $k_d(F)$ | force-dependent detachment rate | 48 |
| $k_d^0$ | force-free detachment rate | 48 |
| $L$ | lattice length | 31 |
| $L_0$ | motor spring rest length | 50 |
| $m$ | cargo's mass | 51 |
| $N$ | number of particles | 31 |
| $N_\pm$ | number of plus-/minus-motors bound to the cargo | 46 |
| $n_\pm$ | number of plus-/minus-motors attached to the filament | 47 |
| $P^s(\cdot)$ | stationary distribution | 30 |
| $P^{eq}(\cdot)$ | equilibrium distribution | 29 |
| $R$ | cargo's radius | 51 |
| $R_A$ | activation radius | 54 |
| $s(F_i)$ | force-dependent stepping rate | 50 |
| $v_B$ | force-free backward velocity | 47 |
| $v_F$ | force-free forward velocity | 47 |
| *U. maydis* | *Ustilago maydis* | 26 |
| ASEP | asymmetric simple exclusion process | 32 |
| ATP | Adenosine triphosphate | 23 |
| CTMC | Continuous time Markov chain | 75 |
| EE | Early endosomes | 27 |

| | | |
|---|---|---|
| EPB | explicit position-based | 46 |
| GTP | guanosine diphosphate | 21 |
| GTP | guanosine triphosphate | 21 |
| KPZ | Kardar-Parisi-Zhang | 34 |
| MF | mean-field | 45 |
| MFPT | first passage time | 68 |
| MPA | matrix product ansatz | 33 |
| MSD | mean square displacement | 24 |
| MT | microtubule | 20 |
| MTOC | microtubule organizing center | 20 |
| NESS | non-equilibrium stationary states | 30 |
| pbc | periodic boundary conditions | 31 |
| SBD | symmetric bimodal distributions | 46 |
| SEP | simple exclusion process | 31 |
| SSEP | symmetric simple exclusion process | 32 |
| TASEP | totally asymmetric simple exclusion process | 32 |
| ZRP | zero range process | 34 |

# List of Figures

# List of Tables

*"Essentially, all models are wrong, but some are useful."*
(George E. P. Box, 1979)

# Chapter 1

# Introduction

A huge variety of phenomena in our daily life, from car and pedestrian traffic [24,51,87,98], animal swarms [26] to the key functions in our own bodies [23, 47, 107], show intriguing characteristics of many particle systems. Though these examples are very different at first glance, they belong to the same class of systems from a physicist's point of view. The fact that they are self-driven, and therefore out of equilibrium, is their common ground. Whereas for equilibrium systems a general theory is known to calculate the probability to be in a given micro state, the steady state distribution for non-equilibrium systems is usually not easy to obtain. Therefore, for every system it remains challenging to predict the essential effects analytically. In contrast to equilibrium systems, driven systems may exhibit a non-trivial behavior already in one-dimension. For instance, in a simple uni-directional exclusion process phase transitions occur for open boundary conditions.

A prime example of non-equilibrium systems is a cell. Most cellular processes take place under the consumption of energy, a signature of non-equilibrium dynamics. Usually, they are rate-driven, resulting in a stochastic sequence of reactions occurring. In the special case of motion inside a cell, which is usually quite dense, hard-core exclusion has to be taken into account. A minimal model ... is of the most intensively studied models in non-equilibrium physics, the totally asymmetric simple exclusion process (TASEP). In the first place, it was introduced as a model to describe the dynamics of ribosomes along mRNA [81]. Since then, the model was extended in many aspects, for instance different boundary conditions [30, 114], different update schemes [4,93,122], multiple species [35,92], several lanes [27,39] and disorder [38,55].

In this thesis we focus on intracellular transport phenomena, to which almost every cellular function is related. It is necessary in order to maintain concentration gradients, but also in order to build and adapt cellular structures. Firstly I will introduce and discuss two different approaches to understand the collective effects occurring in intracellular transport. I addition I will model active particles with internal degrees of freedom with characteristics as they were determined experimentally. On the other hand I will discuss collective effects

occurring in many particle systems in a phenomenological way by means of exclusion processes.

Many intracellular transport issues are carried out by molecular motors i.e. proteins which perform a directed stochastic motion along the polar filaments of the cytoskeleton. Microtubules, one type of a cytoskeletal filament, are indispensable for long-range transport. Two families of proteins, called molecular motors, walk along microtubules, in most instances with opposite stepping direction [2]. Most importantly, these molecular motors are able to bind to various types of intracellular cargo and transport it along the filament. It was observed experimentally, both *in vivo* [110] and *in vitro* [49], that the resulting cargo motion is bidirectional, which suggests that not only one type of motor is attached to a cargo at the same time but that two or more types interact.

Nevertheless, a stable long-distance vesicle transport in neurons is crucial. In the human body the longest axon growing from the base of the spinal cord to the tip of the big toe can reach lengths of up to 1 m [2]. And along those axons stable transport has to be functional. It was observed that for severe neuronal diseases, like Alzheimer's and Parkinson's disease or amyotrophic lateral sclerosis, intracellular transport breaks down and the axon swells due to an accumulation of microtubule-associated proteins (MAPs), molecular motors, organelles and vesicles [28]. In the non-pathological case the cell must avoid this and therefore must have a mechanism to let bidirectionally moving cargos pass by each other.

Hence, one can pose two important questions regarding intracellular transport: How is bidirectional motion organized on a motor level i.e. are two different kinds of motors attached at the same time? And do the motors within one team cooperate? In addition, and on a bigger scale, the collective effects of bidirectionally moving cargo are themselves of interest - what is necessary in order to avoid a jammed scenario? And how does steric exclusion alter the single cargo dynamics? Both types of questions are analyzed in this thesis.

On the molecular motor scale we will first analyze the teaming-up of motors which is particularly relevant for moving large objects like vesicles or cell organelles [99]. Transporting cargo by several motors in a crowded environment is obviously beneficial since it increases the processivity along the MT dramatically and also allows the motor-cargo complex to withstand larger frictional forces. The number of motors is usually estimated to be in the order of up to five motors per team [44, 121]. In experiments however, the cargo trajectory is usually only visible, so that the underlying mechanism of the motor stepping itself remains unclear.

Depending on the given motor-cargo complex and the environment of the filaments, different types of motion have been observed, which could be controlled by several different mechanisms. Some pigment cells (melanosomes) for example have the ability to switch between two states, in which the pigments are either dispersed all over the cell or aggregated in the close vicinity of the nucleus [43, 88]. The mechanisms that allow for such a transition

from a non-biased to a biased motion are not yet well understood but have been related to signaling processes, which regulate the activity of the attached motors [89].

Various theoretical models have been suggested, which aim at describing the origin of the complex dynamics of bidirectionally transported cargo [47, 72, 86]. A mean-field model (MF-model) was introduced a few years ago by Müller *et al.* [86] which describes bidirectional cargo motion driven by two teams of molecular motors,. Their model predicts for a particular choice of parameters the existence of states, which are characterized by a symmetric bimodal (or trimodal) distribution of cargo velocities around both single motor velocities (and zero velocity). In this case, also the distribution of the number of attached motors is bi/trimodal. In the following we shall refer to these types of distributions as *symmetric bimodal distributions (SBD)*. In their model, these states originate from a purely stochastic tug of war between the oppositely directed motors without requiring any regulatory mechanism.

One aim of this work is to test whether those states with SBDs persist beyond mean-field. We use a more explicit modeling approach (explicit position-based model, EPB-model) inspired by the model introduced by Kunwar *et al.* [72]. In contrast to the MF-model, we explicitly consider the motor's positions on the filament, and the couplings between motors and cargo. First we concentrate on the case of equal teams as in [86]. Our main result is that SBDs cannot be observed anymore when the MF assumption is released. By introducing an artificial mutual motor activation, we quantify the degree of motor synchronization, corresponding to a mean-field description, needed to reach the limit of SBDs. We can conclude that this realization is not relevant for biological applications [64].

With this knowledge in mind, we are interested if the EPB-model describes cargo motion qualitatively and quantitatively as it was measured experimentally. It is known that kinesin and dynein do not only differ in their preferred stepping direction but also react differently to the cellular environment. By taking their particular properties into account we develop a model which agrees with experimentally found cargo transport characteristics, like the sub- and superdiffusive motion on different time scales [22, 62, 63, 71, 95]. By means of the EPB-model we show that a variation of the environment changes the cargo-dynamics in a non-trivial way and can even invert the direction of the bias. Furthermore, we analyze how the single cargo motion is influenced by an effective spatial confinement representing highly crowded areas. Having two teams of motors attached to the cargo provides an efficient mechanism to pass, if the area to pass is of the size of a cargo.

Understanding the mechanisms of a single cargo leads us to the question what happens if several of these cargos meet along the filament. As the cargos are usually rather big compared to the size of a molecular motor we cannot neglect the steric interaction anymore, which naturally leads us to exclusion processes. In order to capture the dynamics found by the EPB-model we introduce a coarse-grained model dealing with particles with internal states. These internal states define the particle dynamics inasmuch as the internal state

gives the pairs of left and right hopping rates. We assume four different states, with either a biased motion to the left or to the right or diffusive but with two different diffusion rates. The transitions between the single particle states are defined in a way that the hopping rates change independently. With this choice the mapping onto a distance picture is exact. By numerical integration we find that a density dependent macroscopic condensation occurs due to annealed disorder in the hopping rates.

In order to enrich the phenomenology of collective effects of bidirectionally moving particles, we introduce a second model depending on exclusion processes. It is inspired by the tubular geometry of hyphae, fungal cells growing in a polarized manner, which can reach lengths of several hundreds of micrometers [109]. Surprisingly, their internal microtubule structure is comparable to the one in neurons but they grow faster and under easier environmental conditions. Therefore, they serve as model cells for the analysis of long-range transport [113]. In [79] a TASEP-based model comprising 13 lanes, inspired by experimental observations of dynein dynamics on the hyphal tip [102], was considered. For certain parameter regions the model displays so-called pulsing states in which the system alternatively fills and empties, as a result of the motion of some fronts separating dilute and dense regions.

Many non-equilibrium states have, due to bidirectionally moving objects, an oscillatory or alternating nature not exhibited by equilibrium states. For example the proteins may coherently oscillate from end to end of bacteria [52], and also molecular motors may exhibit collective pulsing states [13]. An understanding of how non-equilibrium conditions allow such states is only just emerging and forms an important challenge of non-equilibrium statistical physics. Such systems, comprising several species and lanes, are often only tractable via a mean-field theory, the simplest implementation that results in a set of partial differential equations for the densities of different species on different lanes. It has been shown in many systems that the mean-field equations and furthermore a reduction to an effective single lane description gave an accurate description of steady state behavior in a wide range of cases [39]. Thus an important task is to determine if and when one can go further with a mean-field description and predict non-equilibrium oscillatory behaviors.

As a contribution to this understanding we studied a minimal model exhibiting periodic density changes in a half-open system. At the open end plus particles, which exclusively hop to the right, are injected with constant rate. All along the lattice they can convert to minus particles and vice versa. The minus particles move in opposite direction and leave the system again at the open boundary. We show that even in a mean-field description two species on two equal lanes are enough to observe periodic density changes, as long as the particle dynamics themselves feature an asymmetry. A discontinuous phase transition from a low-density phase to a pulsing phase occurs. If the asymmetry is implemented in the lane changing, the transition solely depends on the ratio between particle injection and type conversion rate.

For the low-density phase we can predict the bulk densities analytically and confirm it with direct numerical integration of the master equation. In the pulsing phase we observe effects appearing due to a non-linearity in the evolution equations. By means of a stability analysis we can understand structure of the density profiles, including spatial oscillations close to the moving shock.

This thesis is organized as follows: In chapter 2, some biological ingredients needed for active intracellular transport are given. In chapter 3, stochastic many particle systems are introduced in a general way. The focus hereby is on stochastic exclusion processes far from equilibrium, which are related to the systems studied in the following sections. One of these systems is discussed in chapter 4, in which a model for hyphal growth is introduced and analyzed. This is based on a two-species, two-lane system which exhibits a phase transition from a low density to a pulsing phase, in which the density changes periodically in time. Chapter 5 deals with single cargo transport governed by two teams of molecular motors. First, a model with symmetric teams is investigated in order to show that states with SBD as found in a MF description are an artifact of implicit motor synchronization. Second, the results of the same model but with asymmetrically chosen motor parameters are compared to experimentally found ones. Both, sub- and superdiffusive motion is observed in the model. Besides, we are able to predict how the cargo reacts to changes in the cellular environment. A second model on the base of driven lattice gases is discussed in chapter 6. In this model the single particles inherit the motion characteristics as they are found for the model given in chapter 5 by taking internal motion states into account. The simplicity of the coarse-grained model allows one to study the occurring collective effects, both numerically and analytically. The overall conclusion of this thesis is given in chapter 7.

# Chapter 2

# Biological background of intracellular transport

**Contents**



*In this work the tools known from statistical physics are used in order to analyze intracellular activity. For this reason in this chapter some biological facts about cells will be introduced and discussed. At first the internal cell structures will be in focus and it will be pointed out why filaments and their dynamics are important for intracellular transport. Afterwards, more details will be provided about the transport itself - how it is carried out, its properties and components. With this knowledge an example will be given on the basis of a hyphal cell which is a fungal cell in a filamentous growing state.*

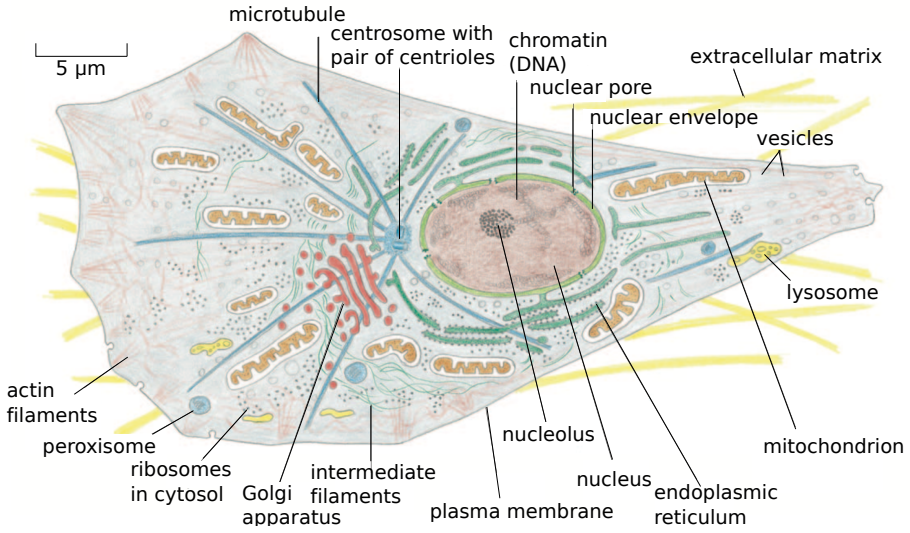


**Figure 2.1:** The drawing depicts a typical animal cell, but almost all the same components are found in plants and fungi and in single-celled eukaryotes such as yeasts and protozoa. Plant cells contain chloroplasts in addition to the components shown here, and their plasma membrane is surrounded by a tough external wall formed of cellulose.
Reprinted by permission from Alberts, B. *et al. Molecular biology of the cell*. Garland Science Taylor & Francis Group, 4 edition, 2002. ISBN 0815332181.

## 2.1 Internal cell structure

The internal structure of a eukaryotic cell is a complex composition as it becomes obvious in Figure 2.1. On the one hand we have the cytoplasm which fills the space between the nucleus and the flexible cell membrane. The cytoplasm itself consists of the aqueous cytosol and i.e. organelles and vesicles. On the other hand we have an elaborated network of three different types of filaments - the actin filament, intermediate filaments and microtubules - which build the cytoskeleton [2] . The three types are build of single proteins in a repetitive manner. In this work we concentrate on microtubules which are crucial for *inter alia* long range intracellular transport [2].

Microtubules (MTs) are hollow protein tubes created by 13 protofilaments and with an inner diameter of 25 nm and with a length in the order of micrometers [2]. The single protofilaments are built by the tubulin-subunits $\alpha$- and $\beta$-tubulin. Due to an ordered assembly with ...$\alpha\beta\alpha\beta\alpha$... the microtubules have a well-defined polarization [118]. On the basis of this polarization we can refer unambiguously to a plus- and minus-end of the microtubule.

The dynamic behavior is not exactly the same *in vitro* and *in vivo* for the MT ends. *In vitro* both ends grow and shrink, even though with different velocities. *In vivo* for most cell types the minus-end is located close to the nucleus at the microtubule organizing center (MTOC). A $\gamma$-tubulin ring stabilizes the minus-end against depolymerization whereas the peripheral plus-end remains highly dynamic. The plus-end can be in two different states: in a growing or a shrinking one corresponding to tubulin polymerization and depolymerization, respec-

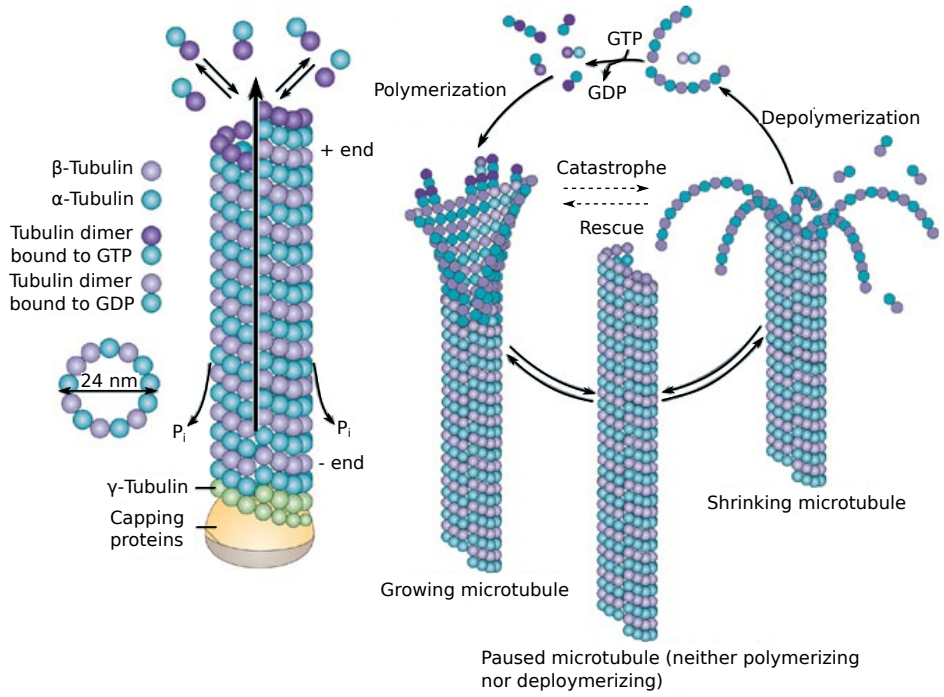


**Figure 2.2:** The drawing shows on the left the structure of the MT and assembly of $\alpha\beta$-dimers. On the right the dynamic cycle is depicted with the transition from shrinking via a rescue event to growing and then via a catastrophe event which occurs usually due to GTP hydrolysis to shrinking.
Reprinted by permission from *Nature Reviews Molecular Cellular Biology*, 9(4):309-322, 04 2008.

tively. The switches between these two states are called rescue and catastrophe, respectively. The rates for the four events (growing, shrinking, rescue and catastrophe) determine the steady state length of the MT [118]. Usually, a guanosine triphosphate (GTP)-cap prevents the plus-end from catastrophe for a while. Once GTP hydrolyzes to guanosine diphosphate (GDP) this stabilizing effect is destroyed. In Figure 2.2 the structure and the dynamic cycle are depicted.

The fact that MTs grow from the nucleus, which is usually located in the cell center, to the periphery in a polarized manner gives so called molecular motors the possibility to use the MTs as streets for long range transport.

## 2.2 Molecular motors

In the former section we got to know the cellular streets - the microtubules. In this section I will introduce the engines which can walk along those streets and transport cargo from the nucleus to the membrane and vice versa - the molecular motors. Molecular motors are proteins which can due to conformational changes move along a polarized filament. In cells a zoo of those molecular motors exists. On actin filaments one mainly finds the family of myosin motors, while the family of kinesin and cytoplasmic dynein walk along MTs. In the

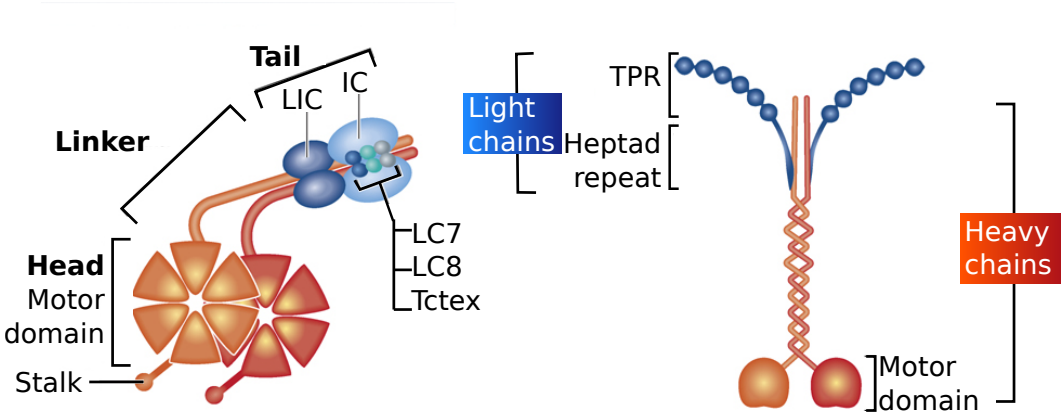


**Figure 2.3:** The drawing depicts dynein (left) and kinesin (right). Both motors consist of a motor domain which can step along the MTs, a linker and a tail domain. However, dynein's structure is more complex.
Reprinted by permission from EMBO J, 30(17):3527–3539, 08 2011.

following sections I will introduce the latter ones only since we are interested in long-range MT transport. Single motors usually make a number of steps but stochastically detach from the filament before they reattach and start stepping again. By measuring the number of steps between these events a run length is defined for every type of motor. If a motor makes several steps in a preferred direction, the motor is called processive.

However, the outstanding feature is not the possibility to walk solely but that molecular motors can bind to several different types of cargo and pull them along the MT. Due to this a motor feels a load force while stepping. Depending on this force, its dynamics usually changes. By pulling cargo molecular motors serve as transport engines and establish active transport in a cell. Compared to passive transport, which occurs due to a concentration gradient, active transport can create a more or less arbitrary spatial cargo distribution inside a cell.

From a molecular point of view dynein and kinesin differ a lot as one can see in Figure 2.3. So is for instance dynein's molecular weight more than three times as big as the one of kinesin [80]. However, from a slightly coarse-grained point of view the motors act similarly. For this work the most important difference is the direction of motion. In the following sections I will point out further similarities and differences between the two types.

### 2.2.1 Kinesin

The term "kinesin" summarizes a whole family of motor proteins. Most of them walk anterogradely along MTs - so towards the plus-en - with a force-free stepping velocity of approximately 1 $\mu$m/s [21]. In most *in vitro* experiments kinesin-I (or conventional kinesin) is used and also in this chapter I will only discuss this particular kinesin. It has two identical heads - the so-called motor domains - which can bind to the tubulin-dimers of the MT. Under

consumption of adenosine triphosphate (ATP), a molecule that serves as an intracellular energy source, the motor takes a step of 8 nm. For one of those steps, whose length corresponds to the length of one tubulin-dimer, kinesin-I hydrolyzes exactly one ATP molecule [21]. The neck linker via which the motor can bind to a cargo surface is composed of two heavy and two light chains.

Kinesin-I is a processive motor with an *in vitro* measured mean run length of 1 $\mu$m if no external force is exerted on a motor which transports a small bead [15]. The finite run length arises from a finite probability of the motor to detach from the filament exponentially with the exerted force. Once detached the motors diffuse in the cytoplasm before they attach again to a MT. In this case the motor moves anterogradely - so towards the plus-end of the MT - with a velocity of roughly 1 $\mu$m/s at saturating ATP concentration [21]. With increasing external force on the motor the velocity decreases linearly until the force reaches the so-called stall force of about 6 pN [67]. Kojima *et al.* [67] measured as well the influence of the ATP concentration on the motor velocity and stall force. The latter is unchanged with changing ATP concentration. The velocity is of course decreasing with decreasing ATP concentration since the probability to hydrolyze an ATP molecule decreases. Schnitzer *et al.* [100] developed a theory which gives the motor's velocity depending on the ATP concentration and the exerted force.

### 2.2.2 Dynein

In Figure 2.3 one realizes easily that dynein's structure is more complicated than kinesin's one. Similar to kinesin, dynein has a motor domain consisting of two heads as well. But here the single heads consist of six $AAA^+$ ATPases ('ATPases-associated with a variety of cellular activities') [60]. Only four out of those six $AAA^+$ ATPases can hydrolyze ATP. This facts hints at a more complicated relation between dynein motility and ATP concentration. The linker and tail region is formed by several light and heavy chains.

In contrast to kinesin dynein moves retrogradely - so towards the minus-end of the MT. But dynein's building complexity reflects also in its motion characteristics. Dynein can make steps of a length of 32 nm. This step size decreases in discrete 8 nm steps with increasing force until the force reaches the stall force [82].

By 2014 it was not possible to realize an experiment to show the processivity of purified mammalian dynein *in vitro* . Richard McKenney *et al.* [84] set up an experiment which shows that dynein needs two more associated proteins (dynactin and BicD) to run processively *in vitro* . Dynein from rat brain shows then a run length of more than 8 $\mu$m with a velocity of about 376 nm/s at saturating ATP concentration.

As expected also dynein's velocity decreases with decreasing ATP concentration and increasing force [116]. And interestingly, the model developed by Schnitzer *et al.* [100] to predict kinesin's velocity in dependence of the ATP concentration and force allows one as well to predict (with different model parameters) dynein's velocity. Contrary to kinesin, for

dynein the stall force depends on the ATP concentration as well. It increases in an affine-linear manner from 0.3 to 1.1 pN [82]. For forces bigger than the stall force a counter-intuitive effect occurs: dynein's probability to detach from the filament does not as expected increase anymore but shows a catch-bond like behavior [72].

### 2.2.3 Collective transport

In the sections above we figured out that kinesin and dynein are proteins which can carry cargo to the plus- and minus-end, respectively. Now we are interested in scenarios where several motors of either the same or different type are bound at a cargo at the same time.

Since each single motor can only step as long as the force it feels is smaller than its stall force more motors should facilitate efficient cargo transport. From this point of view a cargo with more and more motors should walk even faster and smoother. However, in [6] Arpağ *et al.* found that even within a team of identical motors, individual motors can build up substantial forces, both hindering and assisting directions. This shows that cargo transported by several identical motors is highly non-trivial.

It remains an open question whether teams of different types of motors acting on the cargo at the same time exist *in vivo* . Indeed, several evidence was found. In an electron microscopy picture in [8] a mitochondria is bound via four motors to a MT (cf. Figure 2.4 **(a)**). Apparently, two teams of motors are bound to the same cargo and pull in opposite directions. Even more obvious is this scenario in Figure 2.4 **(b)**. The trajectory of an endosome is shown which moves along a MT first in positive $y$-direction before it reverses its direction. During the reversal an elongation of the endosome along the axis of the MT is observed [110]. This is clear evidence that two opposing force are exerted on the cargo at the same time.

Several different quantities were measured to compare bidirectional cargo transport between different cargos or also to compare differences between *in vivo* and *in vitro* transport. In many experiments the cargo motion is characterized via the mean square displacement (MSD) $\langle (X(t+\Delta t) - X(t))^2 \rangle$ of cargo trajectories $X(t)$. Here the brackets indicate the average over $t$. With the relation MSD$\propto t^{\alpha}$ the exponent $\alpha$ characterizes the cargo motion. For a purely ballistic motion $\alpha = 2$ while it is equal to one for the purely diffusive case without bias. This easy classification is usually not given in *in vivo* experiments. In several *in vivo* experiments [22,71,96] a time-dependent exponent was detected. Exponents smaller than one were mainly found on small time scales and refer to subdiffusion [71]. At bigger times an exponent $1 < \alpha < 2$ could indicate a positive temporal correlation in the cargo displacement (superdiffusion) [22,71,96], meaning that it is more likely that the cargo continues moving in the same direction than reversing it. But in fact, the time dependence of the MSD is difficult to interpret for finite times as it is given in biological experiments. Indeed, apparent superdiffusion ($\alpha > 1$) may also originate from a biased but uncorrelated motion of the cargo.

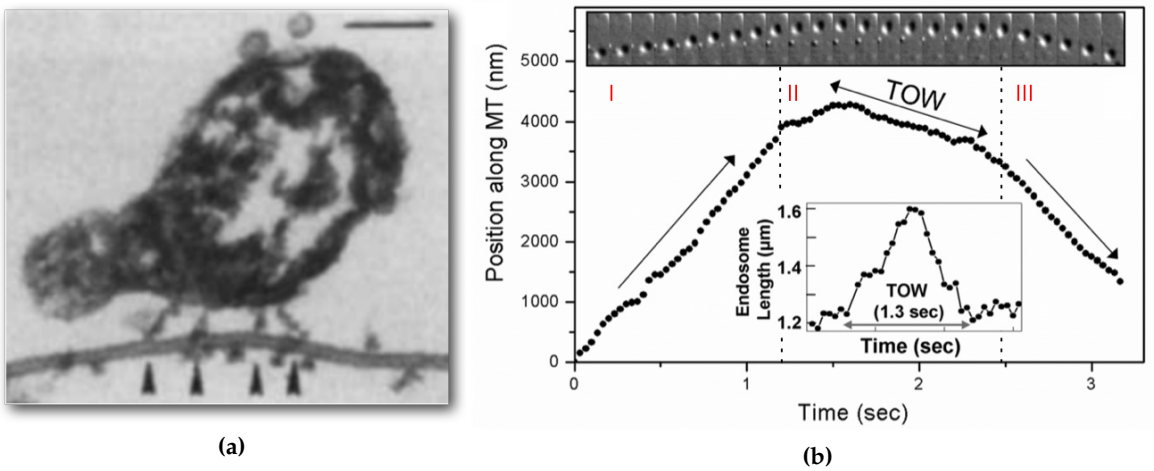


**(a)** **(b)**

**Figure 2.4: (a)** Example of a mitochondria with 4 crossbridges to a microtubule, as seen by electron microscopy. Bar, 0.1 $\mu$m. In the study was shown that the crossbridges are active.
Reprinted by permission from *Nature*, 348(6299):346–348, 11 22, 1990.
**(b)** Tug-of-war between kinesin and dynein on endosomes inside *Dictyostelium* cells. Motion of a endosome close to a reversal is projected along a microtubule by assuming the microtubule to be a straight line. A slow tug-of-war (TOW) segment is sandwiched between fast motion. (Upper Inset) A time series of images (150 ms apart) of an endosome during reversal. The microtubule orientation is approximately vertical. Note the slowing down and elongation of the endosome, interpreted as a TOW between motors. (Lower Inset) Elongation of this endosome is quantified manually. Endosome length (distance between front and rear ends along direction of motion) is plotted as a function of time. There is a 33% increase in the length during TOW. TOW lasts for approximately 1.3 sec.
Reprinted by permission from EMBO J, 30(17):3527–3539, 08 2011.

An easy way to distinguish these two kinds of particle motion by analyzing the variance

$$\mathbb{V}\mathrm{ar}[X(\Delta t)] = \langle (X(t+\Delta t) - X(t))^2 \rangle - \langle (X(t+\Delta t) - X(t)) \rangle^2. \tag{2.1}$$

instead of the MSD.

Anomalous diffusion was found in *in vivo* experiments. One possible explanation, why it was observed, could be the inner cellular structure that presents several obstacles which can impede cargo's motion [22, 119]. Additionally, the MTs form a network which could also induce direction changes. On a branched network a purely ballistic motion also shows $\mathbb{V}\mathrm{ar}[X] \sim \Delta t^{\alpha}$ with $1 < \alpha < 2$ depending on the turning angle distribution of the network [106].

By Kulić *et al.* [71] another explanation of the observed anomalous diffusion was given. They argue that the motion of microtubules which bend and than relax again might add a velocity component to the cargo motion possibly resulting in enhanced diffusion.

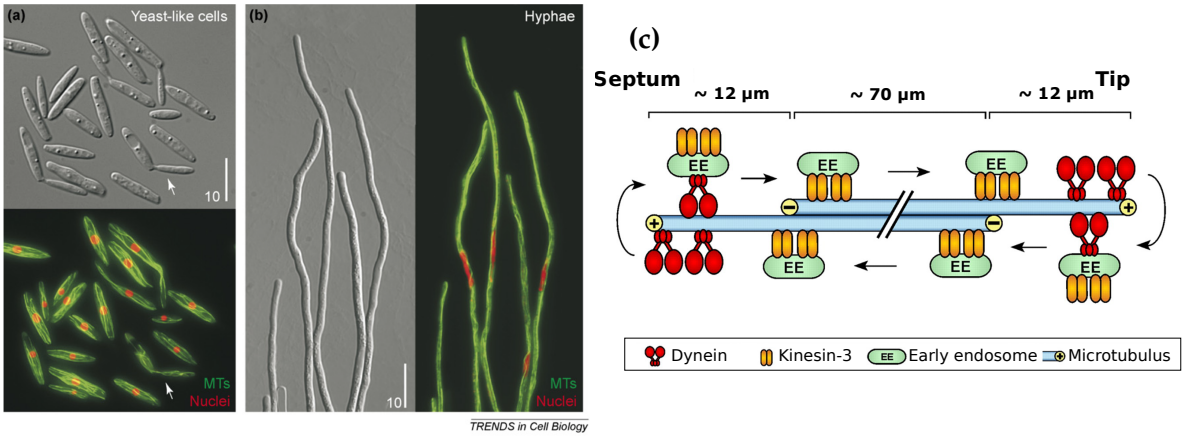


**Figure 2.5:** Morphological stages of U. maydis. **(a)** In liquid culture haploid sporidia grow as yeast-like cells. They contain a single nucleus (a; red fluorescent protein was targeted to the nucleus) that is positioned in the middle of the mother cell, while the polar bud is formed. Upon mitosis, the nuclear envelope is removed and the nuclear proteins are released (arrow: the cell is in late anaphase). Microtubules are formed at cytoplasmic nucleation sites and reach into the bud (a; microtubules are visualized by green fluorescent protein fused to $\alpha$-tubulin). **(b)** Under natural conditions, two mating partner cells recognize each other on the plant surface and fuse, which results in the assembly of the b-transcription factor and the formation of a bi-nucleated hypha. In a mononucleated mutant strain that expresses both halves of the heterodimeric b-transcription factor under the control of inducible promoters filamentous growth can be induced by a medium shift. Again microtubules span the entire length of the hyphae (MT, green) and the nucleus is positioned close to the middle of the cell (nuclei, red) Bar: 10 $\mu$m.
Reprinted by permission from *Trends in cell biology*, 18(2):61–67, 2008.
**(c)** Model for motor cooperation in long-range retrograde EE motility. EEs arrive at MT plus ends and get loaded onto dynein that takes the organelles through the unipolar MT array toward minus ends. At this time, kinesin-3 is a passive cargo. Cytoplasmic MTOCs are absent from the regions near the cell end, and their appearance at $\approx 12$ $\mu$m behind the tip indicates the beginning of the antipolar MT array.
Reprinted by permission from *Molecular biology of the cell*, 22(19):3645-3657, 2011.

## 2.3 Hyphae

In the above sections the behavior on the scale of a single cargo was discussed. In this section now a bigger scale is going to be discussed - the scale of a whole cell. Note that the interior of a mammalian cell is very crowded and complex. That is why in this section the hyphal state of the fungus *Ustilago maydis* (*U. maydis*) is introduced as an example. In general, fungus cells can either be in a yeast state or in a hyphal state. The two states exhibit a very different structure as shown in Figure 2.5 **(a,b)**. These cells exhibit a comparatively easy structure and give a good base to study long range transport in tubular structures [113]. Though, I don't study transport in hyphae in detail in this thesis, this type of cell will give us inspiration for the pulsing behavior discussed in chapter 6.

*U. maydis* is a dimorphic fungus, meaning that it can either be in a spherical yeast-like state or switch into a state of filamentous growth. In the latter *U. maydis* cells form a tubular structure, the so-called hypha, which grows in a polarized manner. These parasitic cells

cause corn smut disease in maize. Usually, hyphae consist of only one single tip cell which penetrates the plant tissue and invades them with their growing tip to on the one hand reach the nutrients but also to overcome the immune system of the host plant. For both processes endocytosis plays an pivotal role [10, 14]. On order to suppress the defense reaction of the maize plant the *U. maydis* cell creates secreted effectors. At the basal end of the hyphal cell, the septum, a vacuole grows with time. This vacuole is involved in many cellular processes, such as macromolecular degradation, for metabolite storage or in cytosolic ion and pH homeostasis [66].

It was discovered in *in vitro* experiments that the microtubule network in a *U. maydis* mutant is antipolar and so similar to mammalian neuronal cells. To establish this structure the existence of dynein is crucial [113]. In the single cells an overlap between oppositely assembled MTs was found over almost the whole length scale of the cell (Figure 2.5**(c)**) [103]. Along this MT network kinesin-I and kinesin-3 (another anterogradely moving motor) and dynein transport some cargo bidirectionally [101]. Interestingly, in the yeast forms *S. pombe* and *S. cervisiae*, which are rather small, kinesin-I and kinesin-3 do not appear. This provides evidence that those two types of kinesins are mainly engaged in long-range transport [113].

One important cellular function for hyphal growth is endocytosis. Endocytosis describes the internalization of molecules (e.g. proteins) via engulfment by the membrane. Right after the absorption the created vesicles are called early endosomes (EE). So far EEs are the only known membranous vesicles in *U. maydis* . It was observed that EEs in *U. maydis* are transported to the nucleus along MTs [104]. Note, that the distance from the middle of the cell, where the nucleus is usually located, to the membrane can be of several tens of micrometers. Comparing this to the step size of a motor of 8 nm shows clearly that stable long-range transport is needed to solve this transport issue. Besides, it was observed that the EEs move in a bidirectional manner, indicating that kinesin and dynein participate simultaneously in endosomal motion. It was indeed measured that during anterograde transport kinesin-3 is active on EEs. If this motors-cargo complex hits a dynein, it reverses its direction suggesting that dynein takes over the cargo and wins against kinesin-3 [104]. If this endosomal motility is suppressed at the initial penetration of the maize cell, the defense reaction of maize makes it impossible for the *U. maydis* to grow further. This effect occurs due to a inhibited secretion of the invading tip [14]. For this reason EEs might either transport the effectors from the vicinity of the nucleus, where they are most probably produced, to the membrane where they form a layer around the penetrating tip, or they might initiate a signaling process in order to produce the effectors. No matter which of the alternatives is true, we learn that endosomal transport is essential.

At the apical tip of *U. maydis* cells an accumulation of dynein is established [74]. In this area the cell has to find a good compromise between the efficiency in the number of dynein motors which actually transport cargo and so walk away from the tip and a number of motors waiting at the tip to capture cargo there. This loading zone can also be related

to the so-called Spitzenkörper, an accumulation of vesicles which is often modeled as a vesicle supply center [12]. Already in 1924 it was observed as a dark spot under a light microscope [18]. Nowadays it is known that the Spitzenkörper gives the direction for hyphal growth (see [112] for a review on hyphal growth).

# Chapter 3

# Introduction to driven lattice gases

## Contents



*In this chapter I will give an overview of (driven) lattice gases. For this class of models the collective effects which alter the behavior of a single particle are studied. From these microscopic interactions one wants to conclude on the macroscopic quantities, like the overall mass/heat/charge flux. I will first introduce stochastic processes in a very general way and explain how one can calculate how a system evolves in time. Then I will show this on particular models, starting with a one-dimensional simple exclusion process. From this I will increase the degree of complexity by analyzing the effects of disorder, several lanes or several particle types.*

## 3.1 Stochastic processes

In statistical mechanics, the probability of finding a system which is in equilibrium with a thermal reservoir in a particular micro state is well known. The Boltzmann-Gibbs law is used to define this probability $P^{eq}(i)$ as a function of the energy $E_i$ of a given state $i$ (or more generally by the system's Hamiltonian)

$$P^{eq}(i) = Z^{-1} e^{-E_i/(k_B T)} \tag{3.1}$$

with the partition function $Z$, the temperature $T$ and the Boltzmann constant $k_B$. In this section I will concentrate on lattice gas models. In that case, it is possible to define some kind of "energy" for each configuration $\mathcal{C}$ on the lattice. If at each time $t$ the probability to observe configuration $\mathcal{C}$ is given by the probability density $P_t(\mathcal{C})$, this density evolves according to its *master equation*

$$\partial_t P_t(\mathcal{C}) = \sum_{\mathcal{C}' \neq \mathcal{C}} \big( W(\mathcal{C}', \mathcal{C}) P_t(\mathcal{C}') - W(\mathcal{C}, \mathcal{C}') P_t(\mathcal{C}) \big). \tag{3.2}$$

Here, $W(\mathcal{C}, \mathcal{C}')$ is the entry of the transition matrix giving the transition rate for going from configuration $\mathcal{C}$ to configuration $\mathcal{C}'$ [56]. To conserve probability in the system the transition matrix has to fulfill the relation

$$W(\mathcal{C}, \mathcal{C}) = - \sum_{\mathcal{C}' \neq \mathcal{C}} W(\mathcal{C}', \mathcal{C}). \tag{3.3}$$

If the transition rates fulfill the *detailed balance condition*

$$W(\mathcal{C}', \mathcal{C}) P^{eq}(\mathcal{C}) = W(\mathcal{C}, \mathcal{C}') P^{eq}(\mathcal{C}') \tag{3.4}$$

equation 3.2 is equal to zero. In that case the probability densities $P_t(\mathcal{C})$ converge towards the equilibrium distribution in the long time limit since each microscopic transition is balanced by its reverse transition.

In this chapter, I will give an overview of results found for driven systems. Many physical phenomena can be modeled in the frame of non-equilibrium processes. Popular representatives are used in car [24,87], pedestrian [51,51] or ant traffic [53], for surface growth [69], biological transport [81, 86, 91] or ionic conductors [58]. In these systems a flux of mass, energy, charge, and so on, exists which can either be imposed by the boundary conditions, by an external field which affects the bulk dynamics or a combination of the two. In that case the system is no longer in thermal equilibrium and so the detailed balance condition is in general not fulfilled. The probability for each micro state evolves with time and only might converge to a stationary (or steady) state which is characterized as the state in which the probability density $P^s(\mathcal{C})$ of leaving a configuration is the same as entering the configura-

tion $\mathcal{C}$

$$\sum_{\mathcal{C}'} W(\mathcal{C},\mathcal{C}')P^s(\mathcal{C}) = \sum_{\mathcal{C}'} W(\mathcal{C}',\mathcal{C})P^s(\mathcal{C}'). \tag{3.5}$$

In the following those states are called non-equilibrium stationary states (NESS).

Unfortunately, for those states one cannot give the stationary distribution *ad hoc* since in general this stationary probability distribution does not follow the Boltzmann-Gibbs law. Especially, in the case of a system far from equilibrium, there is no general theory known so far which gives the stationary distribution. Therefore every single model has to be studied on its own and only a few of them are exactly solvable.

In this thesis, the reason for studying this kind of models is given by the fact that living organisms are not in equilibrium. Especially in the case of active transport, the continuous consumption of energy (mainly in form of ATP) drives the system far from equilibrium. But also from a purely theoretical point of view, non-equilibrium systems are highly interesting and so the field attracted many researchers recently [29,30,50,58]. Already in rather simple driven systems remarkable effects occur, such like phase transitions due to spontaneous (in contrast to explicit) symmetry breaking - even in low dimensions - or long-range correlations [38,68]. Many models are studied within a mean-field approximation i.e. one assumes that there are no two-point correlations between two quantities like for instance the density at neighboring lattice sites. In that case the two-point correlation function becomes the product of two one-point correlation functions.

In this chapter, I will discuss a popular class of systems far from equilibrium - simple exclusion processes (SEP). All systems of this class are defined by an occupation number on a lattice of either zero or one, depending on the presence or absence of a particle at a lattice site $i$ and the dynamics of these occupation numbers. By changing for instance the boundary conditions, different phases can be observed. Even though interesting effects occur for different update rules, in the following I will always assume that we propagate the system in continuous time (see [93] for further details).

## 3.2 Simple exclusion process

At first, let me focus on the easiest case of a lattice gas, a one-dimensional system of length $L$. Since boundary conditions are crucial for this class of models, two popular choices are shown in Figure 3.1. On the left hand side one sees a model with periodic boundary conditions (pbc), on the right hand side the model with open boundaries.

If one assumes periodic boundary conditions such that the sites $i$ and $i+L$ are the same, the system is initialized with a fixed number of $N$ particles that are randomly distributed on the lattice. In the case of an open system, particles enter the system with rate $\alpha$ from the left if site 1 is vacant and with rate $\gamma$ from the right if site $L$ is vacant. In the case that a particle

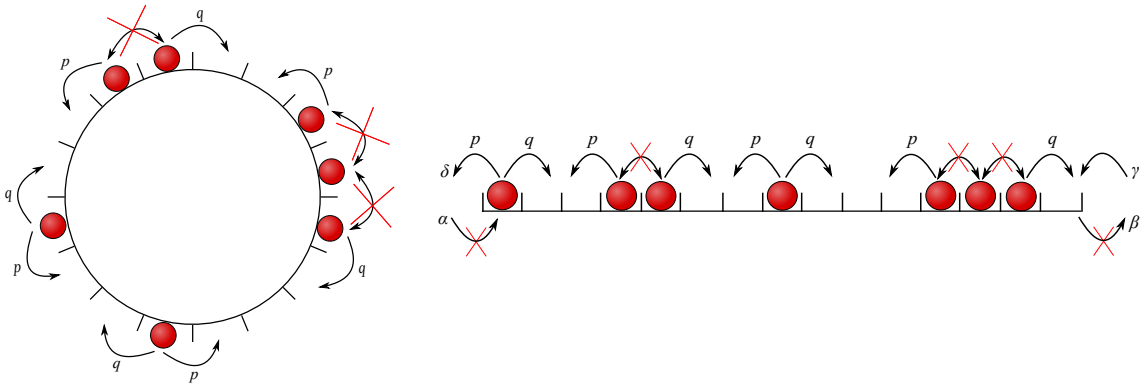


**Figure 3.1:** Sketch of the general SEP with hopping direction probabilities $p$ and $q$ to hop to the left and the right, respectively, in the case that the adjacent site is vacant **(a)** on a ring and **(b)** for an open system. In the case of an open system, particles enter the system with rate $\alpha$ from the left if site 1 is vacant and with rate $\gamma$ from the right if site $L$ is vacant. In the case that a particle occupies site 1 or $L$ it can leave the system with rate $\delta$ and $\beta$, respectively.

occupies site 1 or $L$ it can leave the system with rate $\delta$ and $\beta$, respectively. While the case with pbc corresponds to a canonical model, the open boundaries are like a grand-canonical description with an average number of particles $N$ depending on the injection and exit rates.

A particle sitting at position $i$ at time $t$ hops at time $t + \mathrm{d}t$ with probability $p\ \mathrm{d}t$ to the site $i - 1$ and with probability $q\ \mathrm{d}t = (1 - p)\ \mathrm{d}t$ to site $i + 1$, given that the adjacent site is vacant. With this exclusion rule we can introduce a Boolean variable $\tau_i$ which either takes the value 0 if site $i$ is empty or the value 1 if it is occupied by a particle. One can equivalently see the exclusion model with pbc as a kinetic Ising-model with Kawasaki dynamics where a conserved number of particles corresponds to a fixed magnetization [32]. With the help of the occupation number (or spin state) the $2^L$ possible configurations can be described by the set $\{\tau_1, ...., \tau_L\}$. Since the time evolution of the system depends on the current configuration only, the system is Markovian and its dynamics are described by a master equation as it is given in eq. (3.2).

The simplest version of an exclusion model is a SEP with symmetric hopping direction probabilities $q = p$ (SSEP) with pbc. In this case the transition matrix is symmetric and therefore the system is not driven. Every single configuration $\mathcal{C}$ is equally probable. The detailed balance condition (3.4) holds for this system since every allowed transition occurs with the same probability as its reverse transition. For this reason the system's stationary distribution is the equilibrium distribution. One can show that the mean square displacement of a tracer particle in a SSEP is still Gaussian but compared to pure diffusion the variance now grows as $\sqrt{t}$ with time $t$ [7].

### 3.2.1 (Totally) Asymmetric simple exclusion

While the symmetric simple exclusion process is still an equilibrium system, the situation changes as soon as one considers asymmetric hopping rates $q \neq p$ (ASEP) with the special case of $p = 0$ which is called totally asymmetric simple exclusion process (TASEP). The latter was introduced as a model to describe the kinetics of biopolymerization of ribosomes on a mRNA strand [81] and studied in a more mathematical sense by Spitzer only two years later [111]. TASEP-like models were used lately among other topics as a growth model for crystals [75] and random surfaces [69], or car traffic [87]. With the choice of asymmetric hopping the left-right symmetry is broken and so a phase transition occurs, which belongs to the class of non-equilibrium transitions.

One of the best-studied systems is a TASEP with open boundary conditions and $\delta = \gamma = 0$ corresponding to a particle injection on the left with rate $\alpha$ and a particle outflow at the right boundary with rate $\beta$. In the bulk particles hop with rate 1 to the right. It was shown that the steady state distribution can be calculated exactly and that the dynamics are governed by $\alpha$ and $\beta$ only [30]. Derrida *et al.* use a Matrix Product Ansatz (MPA) in their work [30]. For large systems, they define the average occupation number $\rho = \langle \tau_i \rangle$ and find that in the bulk three different phases exist:

- Phase I: $\alpha > \frac{1}{2}$ and $\beta > \frac{1}{2}$
  $\rho = \frac{1}{2}$

- Phase II: $\alpha < \frac{1}{2}$ and $\alpha < \beta$
  $\rho = \alpha$

- Phase III: $\beta < \frac{1}{2}$ and $\beta < \alpha$
  $\rho = 1 - \beta$.

The particle current is given by $J = \langle \tau_i(1 - \tau_{i+1}) \rangle)$ which is the contribution of each configuration ... $\bullet \circ$... corresponding to an occupied lattice site followed by a vacant one in hopping direction. Phase I is characterized by reaching the maximal particle current $J = 1/4$, Phase II corresponds to a low density phase and Phase III to a high density phase. The phase diagram is given in Figure 3.2**(a)**. For the case $\alpha = \beta < \frac{1}{2}$ the high and low density phases co-exists and so a first order phase transition occurs. One observes a shock that moves diffusively through the system with reflecting boundaries as shown in Figure 3.2**(b)**. The transitions from Phase II/III to Phase I are continuous ones [29].

For a large system with periodic boundary conditions it is possible to determine the average particle velocity $v$ and the diffusion constant $D$ of a tagged particle by means of the

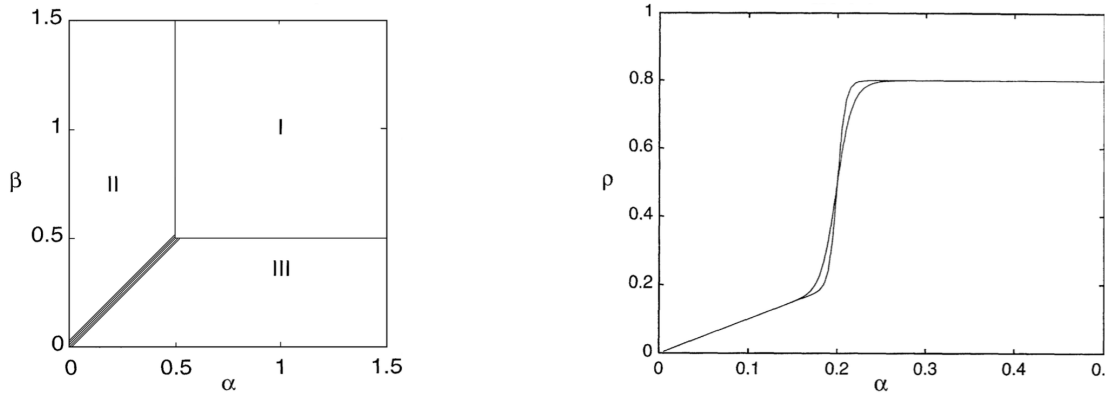


**(a)** **(b)**

**Figure 3.2: (a)** The phase diagram of the TASEP. **(b)** The average occupation $\rho = \langle \tau_{(N+1)/2} \rangle$ of the central site versus $\alpha$ for $N = 61$ and $N = 121$ when $\beta = 0.2$.
Reprinted by permission from B. Derrida, *Physics Reports* 301 (1998) 65-83

Bethe-Ansatz [29] or the MPA [30]:

$$v = \frac{L - N}{L - 1} \tag{3.6a}$$

$$D = \frac{(2L-3)!}{(2N-1)!(2L-2N-1)!} \left( \frac{(N-1)!(L-N)!}{(L-1)!} \right)^2 . \tag{3.6b}$$

Note that the system shows a particle-hole symmetry: a particle moving to the right with probability $q$ in the bulk is the same as a hole moving to the left with probability $1 - p = q$. Due to this symmetry the TASEP (in one dimension) can be mapped exactly onto a zero range process (ZRP) [37] and onto a spin chain [31]. The different mappings can be more convenient to calculate different quantities. For example, it was shown that assuming an infinitely long 1D-lattice the TASEP is equivalent to a simple random interface growth model. Here the hopping of one particle in the TASEP corresponds to the adding of a particle to the surface in the growth model. One can show that the TASEP belongs to the Kardar-Parisi-Zhang (KPZ) universality class [57, 97].

### 3.2.2 Mapping to a ZRP

As mentioned above the ASEP with a periodic lattice of length $L$ and $N$ particles can be equivalently described by a zero range process. In the zero range process one does not characterize a configuration by the particle positions on the lattice but by the amount of holes $n_i$ in front of a particle $i$. With this rule, the occupation number on the lattice with a length $N$ is no longer zero or one but ranges between zero and $L - N = M$, the number of vacant sites in the system.The hopping direction of particles in the ASEP is reversed to those in the ZRP since the hopping of holes is under consideration. The mapping is depicted in

Figure 3.3.

For the ZRP it is often considered that the hopping rates $u(n_i)$ depend on the number of particles $n_i$ at each site $i$ which corresponds to a hopping rate in the TASEP which depends on the distance to the next particle in front. This is relevant for instance in order to model highway traffic, e.g. in the Nagel-Schreckenberg model [87]. If the hopping rate depends on both, the number of particles at the current site and also on the target site, the process is called Misanthrope process [37].

The ZRP shows several non-trivial effects of non-equilibrium systems like a phase separation or long-range correlations. But at the same time the ZRP is exactly solvable in the steady state which has a factorized form (see [37] for a detailed review). The probability $P(\{n_l\})$ to find a particle configuration $\{n_l\}$ is therefore given by the product of the unnormalized weights $f(n_i)$

$$P(\{n_l\}) = Z_{N,M}^{-1} \prod_{i=1}^{N} f(n_i) \tag{3.7}$$

with the partition sum

$$Z_{N,M} = \sum_{\{n_l\}} \prod_{i=1}^{N} f(n_i) \delta\Big( \sum_{i=1}^{N} n_i - M \Big). \tag{3.8}$$

The partition sum ensures that the probability density $P(\{n_l\})$ is normalized and the $\delta$-function gives contributions only for configurations containing exactly $M$ particles. This factorized form allows one to study any model which has integer site variables and a conservation of particles in the framework of a ZRP. Finally, the single site weights are given by the single hopping rates as

$$f(n) = \prod_{i=1}^{n} u(i)^{-1} \quad \text{for } n > 0 \text{ and } f(0) = 1. \tag{3.9}$$

That the expression given in eq. 3.7 gives the steady state can be easily shown by comparing the motion of the particles in the ZRP to a random walker with random hopping rates.

By means of the above results [37] one can calculate the probability $p(n)$ that a given lattice site contains $n$ particles

$$p(n) = f(n) \frac{Z_{N-1,M-n}}{Z_{N,M}} \tag{3.10}$$

and the average hopping rate

$$\langle u(n) \rangle = \frac{Z_{N,M-1}}{Z_{N,M}}. \tag{3.11}$$

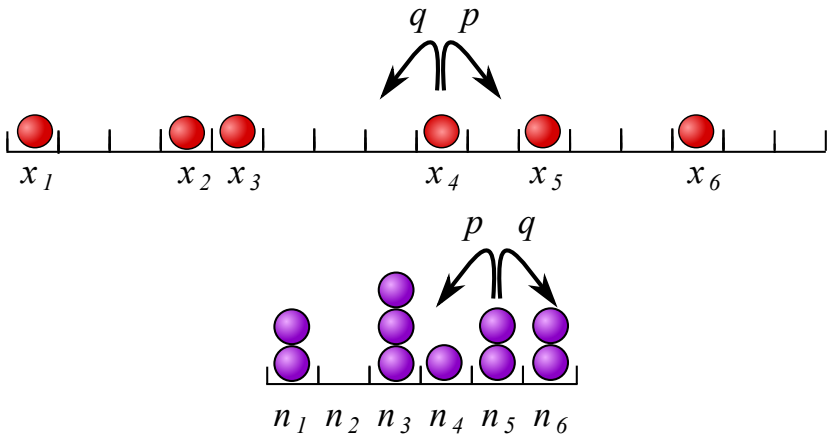


**Figure 3.3:** Mapping between the ASEP and the ZRP. Instead of the particle positions on the lattice $x_i$ the new variable is $n_i$, which corresponds to the number of holes in front of particle $i$ in the ASEP frame. If particles in the ASEP move with rate $p$ to the right and with rate $q$ to the left, exactly the opposite is true for the ZRP. Here, particles move with rate $q$ to the right and with rate $p$ to the left due to the particle-hole symmetry.

Note, that the ZRP is in general not restricted to a one-dimensional lattice but that the factorized form is valid for arbitrary connected, homogeneous and symmetric lattices [37].

### 3.2.3 Systems with quenched disorder

In the model described above, the particles all had the same albeit asymmetric hopping rates. For applications it is often necessary that the hopping rates exhibit some (quenched) disorder. This disorder can either be particle-dependent which is of special interest to model car and pedestrian traffic [4, 24] or site-dependent which is, among other models, used to describe ant traffic where ants induce some spatial disorder by excreting pheromones along a trail [53]. But also from a purely theoretical point of view, these models exhibit particularly interesting effects.

Given are $N$ particles on a one-dimensional lattice of length $L$ with periodic boundary conditions. The same rules as in the ordinary ASEP apply but additionally one assumes the hopping rates to the left and to the right $q_\mu$ and $p_\mu$ ($\mu = 1...N$), respectively, of the $\mu$-th particle as independent random variables drawn from the distributions $\mathcal{P}(p)$ and $\tilde{\mathcal{P}}(q)$ [38, 70]. In this case, it is also convenient to use the distance between the particles $u_\mu = x_{\mu+1} - x_\mu - 1$ since then a mapping on a ZRP is possible, similarly as it is described in section 3.2.2. It is easy to see that this mapping corresponds implicitly to a transformation from particle-wise to site-wise disorder.

The steady state weight for the single configurations for the disordered case can be calculated analytically and are given in a factorized form [38]. If one now considers only the case that the particles hop to the right, so $q_\mu = 0$ for all $\mu$, one finds that the system undergoes a phase transition with increasing particle density. In the easiest case in which only one single

particle has a smaller hopping rate than the remaining particles, it is easy to understand why this transition from a condensation of holes at low particle densities to a high density phase occurs: In the low density case the single slow particle hinders the remaining particles. In vehicular traffic this scenario is comparable to a (infinitely long) one-lane road with some cars and a single truck which impedes the remaining cars to drive with their desired velocity. With increasing particle density the probability that the adjacent site is vacant decreases exponentially and therefore also the fast particles prevent their follower from hopping due to the exclusion rule. This makes clear that the phase transition occurs due to fluctuations in the distance between the particles.

The same effect is observed for a general distribution of hopping rates $p_\mu$. Depending on the hopping rate distribution one can determine a critical density at which the phase transition occurs. In the work by Evans [38] a distribution which is similar to a $\Gamma$-distribution with a lower limit at $p = 1$ is chosen. He shows that the phase transition occurring is exactly equivalent to that between a Bose-Einstein condensate and a gas phase. In the model described here the condensate corresponds to a macroscopic number of vacant sites *condensed* in front of the slowest particle. Please note that even though the transition is the same it is not trivial to find the steady state distribution for this system since the dynamics are not related to an energy function. In the work of Evans [38] a MPA is used in order to obtain this steady state distribution. Furthermore, one can analyze the density fluctuations in the steady state. It can be shown for a density-dependent flux $J(\rho)$ that the fluctuations move as a kinematic wave with speed $c = \mathrm{d}J(\rho)/\mathrm{d}\rho$ in time $N/c$ [77].

Similarly to the case of disorder in the particle hopping rates one can consider the particles to be equal but moving in a complex energy landscape represented by site-dependent hopping rates. One associates to each lattice site a pair of hopping rates which are random numbers drawn from some probability distributions. In this case the single particles don't have their own specific hopping rates anymore but the hopping depends on their position on the lattice. A sketch is given in Fig. 3.4. One can differentiate the unidirectional from the bidirectional case. In the latter the hopping rates in both directions are drawn from a distribution while for unidirectional motion the hopping rate in one direction is equal to zero. For low densities and unidirectional hopping one finds a finite flux and a homogeneous distribution of particles along the lattice. With increasing density a phase transition occurs to a state in which a high and a low density region along the lattice co-exist. Still, a finite flux is measurable [11].

Considering now a bidirectional motion such that the hopping rates in both directions are non-zero random variables drawn from the *same* distribution, the overall behavior changes. The lattice exhibits local minima but no bias is realized such that for big enough systems the steady state flux is equal to zero. The density profile along the lattice is strongly dependent on the single realization of the random variables but one always observes a finite fraction of lattice sites with a high particle density. On the other hand in the case of

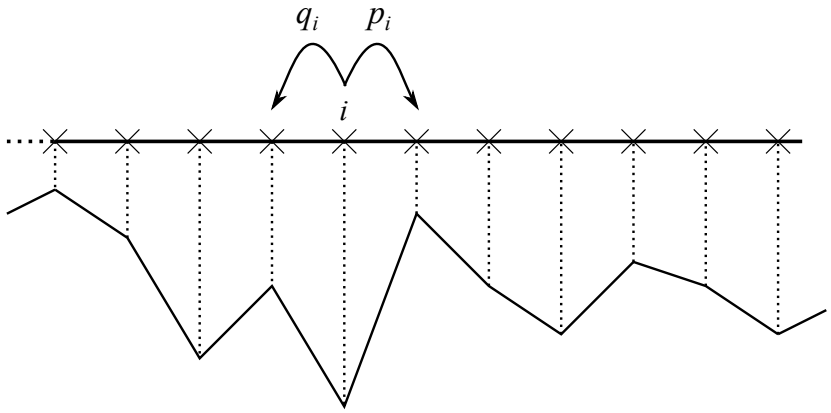


**Figure 3.4:** Sketch of an ASEP with spatial disorder. To each lattice site $i$ a pair of hopping rates $(q_i, p_i)$ is associated. By the ration of these two hopping rates an effective potential is created. If $p_i \ll q_{i+1}$ and at the same time $q_i \ll p_{i-1}$, a deep local minimum exists at site $i$.

a tilted energy landscape in a sense that the two probability distributions for the hopping rates are not equal, one observes a non-zero flux in favor of the *stronger* direction. For the particle density one finds two regions, one very close to zero density and a second one close to a density of one [11, 55]. For models with spatial disorder it can be convenient to use a renormalization ansatz [55].

## 3.3 Two species models

Going one step further in the direction of intracellular transport, one has to think about systems where more than one species walks along the lattice. Those species could either hop with different velocities in the same direction or even hop in opposed direction. Especially the latter case is quite often observed in long-range intracellular transport as discussed in section 2.2.3. If one simply assumes a periodic system with two species, which hop in opposed direction and cannot overtake each other, the system evolves until particles are blocked by at least one particle of the other species. This leads to macroscopic clustering where the average cluster length depends on the initial conditions of the system.

The easiest way to solve this problem is given by a model which considers some site exchange between particles of different species. In their works Evans *et al.* [35, 36] define two types of particles which perform a TASEP with opposed hopping direction with open boundary conditions. For that reason each out of $N$ lattice sites can either have the values $(+)$, $(-)$ or $(0)$, which means that either a positive particle which moves to the right or negative particle which moves to the left occupies the site or that the site is empty. Additional to the ASEP hopping rules they allow some exchange process such that the systems dynamics at an infinitesimal time d$t$ are given by

$$\begin{aligned}
(+)_i(0)_{i+1} &\to (0)_i(+)_{i+1} \qquad \text{with probability } \mathrm{d}t \\
(0)_i(-)_{i+1} &\to (-)_i(0)_{i+1} \qquad \text{with probability } \mathrm{d}t \\
(+)_i(-)_{i+1} &\to (-)_i(+)_{i+1} \qquad \text{with probability } \gamma\ \mathrm{d}t.
\end{aligned} \tag{3.12}$$

At the two ends of the lattice a particle is either removed or injected according to the following rules

$$\begin{aligned}
(0)_1 &\to (+)_1 \qquad \text{with probability } \alpha\ \mathrm{d}t \\
(-)_1 &\to (0)_1 \qquad \text{with probability } \beta\ \mathrm{d}t
\end{aligned}$$

for the left end ($i = 1$) and

$$\begin{aligned}
(0)_N &\to (-)_N \qquad \text{with probability } \alpha\ \mathrm{d}t \\
(+)_N &\to (0)_N \qquad \text{with probability } \beta\ \mathrm{d}t
\end{aligned}$$

at the right end ($i = N$) of the system.

These rules ensure that the system does not end up in a stuck configuration as it occurs in the model without site-exchange but that a measurable flux of both particles types is observed. One expects due to the left-right symmetry in the system that the total flux $J = J_+ + J_- = 0$ should vanish in the thermodynamic limit. However, the system exhibits for some combinations of $\alpha,\ \beta$ and $\gamma$ a spontaneous symmetry breaking which results in unequal fluxes of positive and negative particles [35,36].

In the limit $\alpha \to \infty$ the system is devoid of holes since they are directly removed at the two boundaries. In that case the system can be reduced to a one-species TASEP with a hopping rate $\gamma$. Otherwise, it can be shown in the plane $\beta = 1$ again by the matrix method that in the case of finite $\alpha$ the two-species exclusion process exhibits a boundary-induced phase transition for $\gamma < 2$. It can be distinguished between a low-density phase and a maximal current phase. The latter is characterized by a power-law decrease in the density of holes. It goes to zero with the distance to the boundary, which is similar to the decay in the one-species model. Therefore, it is called power-law phase.

For all other values of $\beta$ and $\alpha$ the model has not been solved exactly yet. In these cases a mean-field method was used and solved analytically for $\gamma = 1$ where the existence of two broken symmetry phases was demonstrated. In the case of $\gamma = 1$ the mean-field equations for the flux decouple in the bulk and can so be solved separately. The only coupling now exists via the boundary fluxes. In the work by Evans *et al.* [35] the mean-field phase diagram is given. There, it is shown that the current is symmetric if the system is either in a low-density phase or in a power-law phase. Otherwise, there are two phases, a low-density/low-

density and a high-density/high-density one, where the fluxes are not equal and therefore the system is not symmetric.

## 3.4 Stability analysis

In the section above a model with two-species but with local particle exchange is discussed which shows a non-zero current in both hopping directions. Another way to realize a flux in two directions is given by introducing a second lane. Here one can distinguish between models where the particles are associated to a given lane depending on their direction of motion [5, 54, 78] and models where particles with both hopping direction use both lanes equally [33, 34, 79]. In this section I do not want to go too much into detail about the single results that were found for this class of model but rather introduce a generic way to obtain the phase diagram.

In the work of Evans *et al.* [39] a new way of stability in the steady state is discussed, which corresponds to a generalization of the extremal current principle as it was used in the one-dimensional TASEP with open boundaries. In their work a class of models with two-lanes of length $L$ and open boundary conditions is discussed. They explicitly allow the particles to hop between two lanes but the following criteria have to be fulfilled

R1 The particle hopping is local, such that the hoping rules within each lane are not altered by the other lane, plus a possibility to change between lanes at the *same* site.

R2 The hopping rate within the same lane does not depend on the occupancies in the neighboring lane but only on those in the same lane.

R3 On average, the transverse flux of particles from one lane to the other increases with the occupancy of the departing lane and decreases with that of the arriving one.

R4 The densities of the reservoir are assumed to be equilibrated, that is the densities are always chosen such that they produce zero transverse flux.

R5 The bulk dynamics are translationally invariant.

Even with these restrictions a wide class of particles can be described within this framework. One possible model is depicted in Figure 3.5. There the rules on the two lanes are chosen differently: The lower lane corresponds to a TASEP model with bulk hopping rate $p$. On the upper lane on contrary the particles move in a diffusive manner, no exclusion is considered on that lane and the particles hop with rates $D^-$ and $D^+$ to the left and to the right, respectively. The particle reservoirs at the boundaries have the densities $\tau_l$ and $\tau_r$, at the left and right boundary of the lower lane, respectively. On the upper lane the densities given by $\sigma_r$ and $\sigma_l$, also here the indices correspond to the left and right boundary. The injection and exit rates are chosen in a way that they fulfill rule R4. With rate $k_d$ and $k_a$ the particles

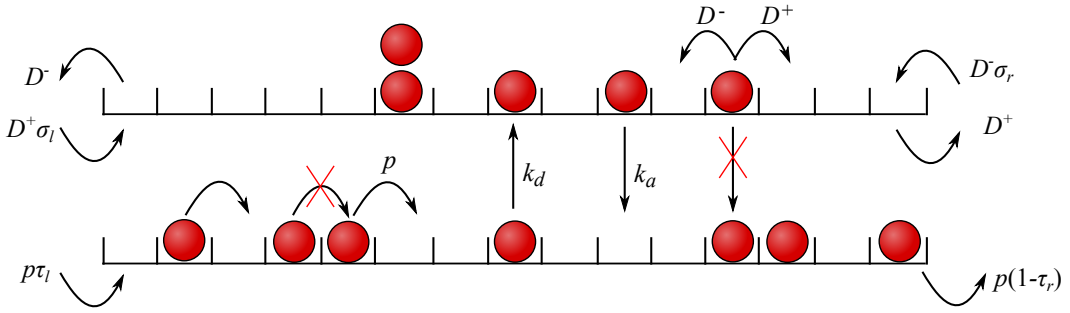


**Figure 3.5:** Example for a model which fulfills the rules R1-R5. The lower lane corresponds to a TASEP with bulk hopping rate $p$. On the upper lane particles move diffusively such that no exclusion is considered and the hopping rates to the left and to the right are $D^-$ and $D^+$, respectively. The particles from the lower (upper) lane change to the upper (lower) one with rate $k_d$ ($k_a$). The boundary conditions are chosen in way that they fulfill rule R4.

can change between the two lanes. The average densities at site $i$ on the lower (upper) lane given by $\tau_i$ ($\sigma_i$).

The idea how to construct a general phase diagram for models fulfilling the rules R1-R5 is rather simple: One assumes that a constant plateau is a solution which is in agreement with the boundary conditions and then adds some temporal and spatial perturbations to these plateau densities. By studying how these perturbations evolve in time and space it is possible to give stability criteria. By means of these criteria one finds the steady state density profiles. Lets discuss this for the model described above as it was done in [39].

At first one can use a mean-field approximation to find expressions for the currents within the single lanes $\mathcal{J}_i^\tau$ and $\mathcal{J}_i^\sigma$ from lattice site $i$ to $i+1$ and for the one between the two lanes $\mathcal{K}_i$ at site $i$

$$\mathcal{J}_i^\tau = p\tau_i(1-\tau_{i+1}) \tag{3.13a}$$
$$\mathcal{J}_i^\sigma = D^+\sigma_i - D_-\sigma_{i+1} \tag{3.13b}$$
$$\mathcal{K}_i = -k_d\tau_i + k_a\sigma_i(1-\tau_i). \tag{3.13c}$$

Using the fluxes it is easy to give the time evolution of the average densities $\tau_i$ and $\sigma_i$

$$\frac{\mathrm{d}}{\mathrm{d}t}\tau_i = -\mathcal{J}_i^\tau + \mathcal{J}_{i-1}^\tau + \mathcal{K}_i \tag{3.14a}$$
$$\frac{\mathrm{d}}{\mathrm{d}t}\sigma_i = -\mathcal{J}_i^\sigma + \mathcal{J}_{i-1}^\sigma - \mathcal{K}_i \tag{3.14b}$$

For the following calculations it is easier to write the equations in a continuous space variable $x = \frac{i}{L}$. One finds for the average densities by means of a Taylor expansion up to second order

$$\partial_t\tau = -\partial_x\left[J_\tau - D_\tau\partial_x\tau\right] + K(\tau,\sigma) \tag{3.15a}$$

$$\partial_t \sigma = -\partial_x \left[ J_\sigma - D_\sigma \partial_x \sigma \right] - K(\tau, \sigma). \tag{3.15b}$$

This representation directly separates the advective parts $J_\tau$ and $J_\sigma$ from the diffusive parts $-D_\tau \partial_x \tau$ and $-D_\sigma \partial_x \sigma$. The equations for the boundaries

$$\tau(0) = \tau_l \qquad \tau(1) = \tau_r \qquad \sigma(0) = \sigma_l \qquad \sigma(1) = \sigma_r \tag{3.16}$$

are determined by the densities of the reservoirs. Since it assumed that the boundary densities are equilibrated (R4) the inter-lane flux has to fulfill $K(\tau_l, \sigma_l) = K(\tau_r, \sigma_r) = 0$. Furthermore, one gets from rule R3 for the density-dependence between the two lanes of hopping rates the inequation

$$\partial_\tau K < 0 < \partial_\sigma K. \tag{3.17}$$

The idea [39] is now to perturb constant profiles $\tau(x) = \tau_0$ and $\sigma(x) = \sigma_0$ which fulfill the bulk relation $K(\tau_0, \sigma_0) = 0$. One can show that flat solutions are always dynamically stable to temporal perturbations. In order to obtain the phase diagram it is of particular interest to check for spatial perturbations. Assume that the left and right boundary densities are not equal and that $(\tau_l, \sigma_l) < (\tau_r, \sigma_r)$. In that case one sees that the two constant profiles which match the right boundary values are higher than those coming from the left boundary. In order two match the two plateaux on the left and on the right a perturbation added to the left constant profile has to diverge with increasing $x$.

In order to calculate the perturbations for the model above one introduces the pair $(\epsilon(x), \eta(x))$ which are added to the plateau values $(\tau_0, \sigma_0)$. Assuming that $\epsilon$ and $\eta$ are small and putting the expressions $(\tau_0 + \epsilon(x), \sigma_0 + \eta(x))$ into equations (3.15) gives in the steady state a set of first order equations [39]

$$D_\tau \partial_x \epsilon = (\partial_\tau J_\tau) \partial_x \epsilon - (\partial_\sigma K) \eta - (\partial \tau K) \epsilon \tag{3.18a}$$

$$D_\sigma \partial_x \eta = (\partial_\sigma J_\tau) \partial_x \eta + (\partial_\sigma K) \eta + (\partial \tau K) \epsilon. \tag{3.18b}$$

Note that the derivatives with respect to $\tau$ and $\sigma$ are taken at $\tau_0$ and $\sigma_0$, respectively and similarly $D_\tau$ and $D_\sigma$ are evaluated at $\tau_0$ and $\sigma_0$, respectively. Solutions for this set of equations can be written in an exponential form

$$(\epsilon(x), \eta(x)) = \exp(\lambda x)(\epsilon_0, \eta_0). \tag{3.19}$$

With this ansatz one can write the set of equations in (3.18) in a matrix form

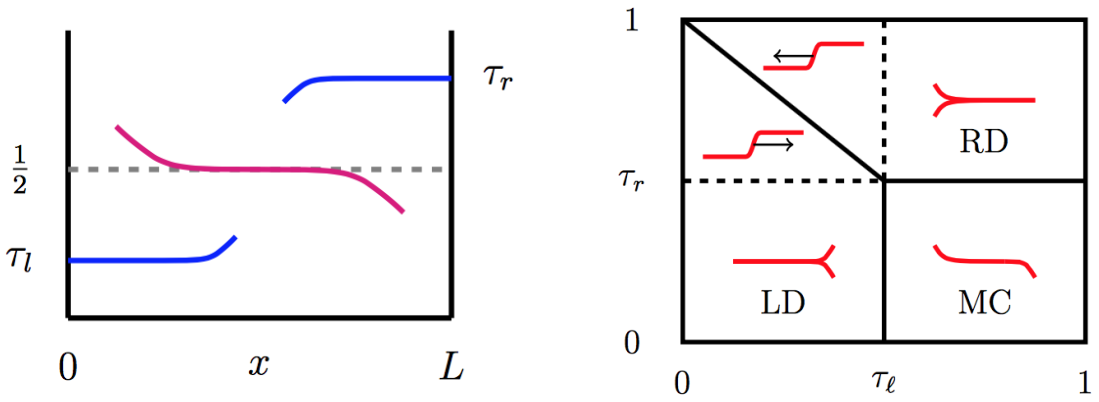


**(a)** **(b)**

**Figure 3.6: (a)** From the left and right reservoirs boundary densities $\tau_l$ and $\tau_r$ are induced. Various possible steady profiles are presented, together with their stability. **(b)** Phase diagram constrained by the stability of the equilibrated plateaux presented on the left panel.
Reprinted under CC BY licence from M.R. Evans, *et al. Journal of Statistical Mechanics: Theory and Experiment*, 2011(06):P06009, 2011

$$0 = \begin{pmatrix} \lambda^2 D_\tau - \lambda \partial_\tau J_\tau + \partial_\tau K & \partial_\sigma K \\ -\partial_\tau K & \lambda^2 D_\sigma - \lambda \partial_\sigma J_\sigma - \partial_\sigma K \end{pmatrix} \begin{pmatrix} \epsilon_0 \\ \eta_0 \end{pmatrix}. \tag{3.20}$$

In order to find non-trivial solutions one needs to find the values of $\lambda$ for which the determinant $\lambda^{-1}\xi(\lambda)$ of the matrix in eq. (3.20) is equal to zero. One can show that four roots exist but that only one of them is relevant for constructing the phase diagram [39]. In their work Evans *et al.* [39] find that those perturbations which connect different plateaux change stability at an extremum of the total advective current $J_{\text{tot}} = J_\tau + J_\sigma$. Perturbations converge if $\frac{\mathrm{d}}{\mathrm{d}\tau_0} J_{\text{tot}} < 0$, while they diverge for $\frac{\mathrm{d}}{\mathrm{d}\tau_0} J_{\text{tot}} > 0$.

For the model with $D^+ = D^- = 0$ the calculation is particularly simple. In that case no advective current exists on the upper lane such that the total current depends on $\tau_0$ only, namely

$$\frac{\mathrm{d}}{\mathrm{d}\tau_0} J_{\text{tot}} = p(1 - 2\tau_0). \tag{3.21}$$

With the criteria for the stability of the perturbations one finds for $\tau_0 < 1/2$ diverging profiles and converging ones for $\tau_0 > 1/2$. The special case of $\tau_0 = 1/2$ is marginal as negative perturbations diverge whereas positive ones converge. These cases are depicted in Figure 3.6 **(a)**.

In order to obtain the phase diagram one now simply has to analyze the four possible matchings between the regions for the plateaux given by the left and right boundary densities. The full phase diagram resulting from this analysis shown in Figure 3.6 **(b)**.

The four phases found for the model are

- A maximal current phase (MC) for which the left reservoir density $\tau_l > 1/2$ while the right one is $\tau_r < 1/2$. In that case particles can easily move through the bulk.
- For $\tau_l < 1/2$ and $\tau_r < 1/2$ the stability analysis allows to obtain a flat with $\tau(x) = \tau_l$ connected to the right boundary by a short boundary layer (LD).
- For $\tau_l < 1/2$ and $\tau_r < 1/2$ the situation is similar but with the plateau density $\tau(x) = \tau_r$ and the boundary layer at the left end of the system (RD).
- Finally, for $\tau_l < 1/2$ and $\tau_r > 1/2$ the stability analysis predicts a moving shock profile connecting two constant plateaux $\tau(x) = \tau_l$ to $\tau(x) = \tau_r$. The shock velocity can be determined by mass conservation.

The model described above is rather simply. But the phase diagram for more complex can also be predicted by this method (see e.g. Figure 4 in [39]). In a later publication Curatolo *et al.* [27] generalize this method for two lanes to one for multiple lanes.

## 3.5 Chapter conclusion

In the last decades a variety of driven lattice gas models has been introduced in the field of non-equilibrium statistical mechanics. From the easiest model of a symmetric SEP on a ring to multiple lane and multiple species models an impressive collection of effects has been observed. And surprisingly, even for many models exact analytic results were found. In this overview, which is far from being complete, my focus was on those models which are related to my own research. The family of exclusion processes became much wider in the last years, with both numerical and analytic results, even though for the latter the results are often found in a mean-field approximation.

It is important to remember that many of the effects which were discovered, are often induced by the boundary conditions rather than from the bulk dynamics, as for example the phase transitions in the TASEP with open boundary conditions. Note, that these effect find no counterpart in equilibrium stationary state since by definition no microscopic currents exist. Furthermore, disorder plays an important role. Due to disorder, both particle-wise and site-wise, the spatial symmetry can be broken and condensation can occur.

In order to analyze bidirectional motion it may become necessary to either allow particles to overtake each other, which may require more lanes, or to change their hopping direction. Both allow the system to establish a finite particle flux in each direction.

By means of a stability analysis it is possible to predict phase diagrams for several multi-lane models. One assumes spatial or temporal perturbations around a flat density profile which depends solely on the reservoir densities. By means of these flat profiles one finds

conditions on the flux at the boundaries which determine the allowed density profiles for different combinations of reservoir densities.

# Chapter 4

# Bidirectional cargo transport

## Contents



*First, I summarize the results found by a mean-field model for bidirectional cargo transport [86]. In this framework symmetric bimodal distributions for the cargo velocity and the number of motors attached to the filament were found. I introduce a model which takes force fluctuations into account in order to clarify whether bimodal distributions are biologically relevant. By analyzing the dynamics of the system I find that distributions of this particular form are irrelevant for describing intracellular cargo transport. In a second step the differences between two teams of motors are taken into account and non-trivial effects are observed. The influence of the surrounding environment changes the motion characteristics in a counter-intuitive way. Furthermore, the impact of intracellular thermal fluctuations and an effective confinement are analyzed. The results found are, if possible, compared to experimental ones.*

As discussed in section 2.2.3 the case that a cargo is transported bidirectionally is often observed even though the cargo might aim a particular position in the cell. In this chapter the knowledge gained by experiments is used in order to achieve a model which is able to make predictions on this bidirectional cargo transport.

In a first section I will devote myself to a mean-field (MF) model by Müller *et al.* [86]. This model became quite popular among physicists as well as biologists. It predicts for a broad range of parameters the existence of states in cargo transport characterized by a symmetric bimodal (or trimodal) distribution of cargo velocities around both single motor velocities (and zero velocity). In this particular case also the distribution of the number of attached motors exhibits a bi-/trimodal form. Those results are surprising since the first presumption for a cargo transported by symmetric teams of motors would be a stalemate. In the following of this work we shall refer to this bimodal type of distributions as *symmetric bimodal distributions* (SBDs). In the MF model, these distributions are created solely by stochastic fluctuations.

Via introducing an explicit position-based model (EPB-model) in the second section of this chapter we will question the existence of those SBDs in view of biological relevance. In this model each motor's filament position is taken into account and consequently force fluctuations between motors and cargo occur as they are expected in a cell [6]. We show that in the case of equal teams SBDs cannot be observed anymore when the MF assumption is released. It is discussed which effects in the MF model are responsible to obtain those SBDs. As a result an artificial mutual motor activation is introduced and it becomes obvious that, even if a (in biological systems not expected) partial motor synchronization could be induced, the MF assumption would then be relevant only in the case of (biologically improbable) huge teams of motors.

In a third part the restriction to equal teams is released and the differences that are known for kinesin and dynein referring to the motion characteristics are modeled in detail. Already small changes of the environment can influence the cargo-dynamics in a non-trivial way such that the direction of the cargo's bias can even be inverted. In the EPB model the crowdedness of the cellular environment is implicitly modeled as an effective viscosity. One then observes a non-trivial response to this generalized force which indicates that complex interactions between the attached molecular motors exist even though they are only coupled via their linkage to the same cargo. Additionally, the EPB model generates super-diffusive cargo motion on biological relevant time scales [22, 95]. In the case of an additive stochastic force representing the thermal fluctuations of the environment one observes a cross-over from sub- to superdiffusion at very small times as it was found experimentally *in vivo* [71]. In a final step we analyze under which circumstances active bidirectional transport is more efficient than normal diffusion.

The content of this chapter is discussed in our publications [62–65].

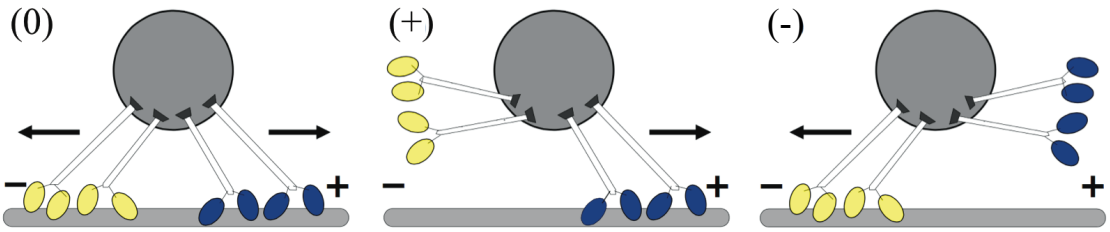


**Figure 4.1:** Cargo transport by 2 plus (blue) and 2 minus (yellow) motors: possible configurations (0), (+), and (-) of motors bound to the MT. For configuration (0), the motors block each other so that the cargo does not move. For configuration (+) and (-), the cargo exhibits fast plus and minus motion, respectively.


## 4.1 MF model

In the last years various theoretical models have been suggested with the aim to describe the origin of the complex dynamics of bidirectionally transported cargo [47,72,86].

Müller *et al.* [86] introduced a few years ago a mean-field model for bidirectional cargo motion driven by two teams of molecular motors consisting of $N_+$ plus- and $N_-$ minus-motors, respectively. They assume that two equal teams of motors are bound to the cargo at the same time as it is depicted in Figure 4.1. By detaching from and re-attaching to the filament the number of actively pulling motors is changed with time.

The cargo motion is then determined via the force balance between the two motor-teams without explicitly taking the motor positions into account. A mean-field assumption stating that forces $F_\pm$ are equally shared among bound plus-motors ($n_+$) and minus-motors ($n_-$) gives the basis for the model

$$n_+ F_+ = -n_- F_- =: F_c. \tag{4.1}$$

$F_c$ is then the effective force exerted on the cargo which determines its velocity.

An equivalent formulation of the MF assumption is that the motors of the same team are all at the same distance from the cargo. In order to share the force equally among the motors within one team for the motors must move synchronously. This allows one to formulate the MF model without any explicit reference to the motor positions, but simply via the number of bound motors per team. The cargo's velocity depends only on these forces and is uniquely determined for a given number of attached plus- and minus-motors and is

assumed to decrease linearly with the applied force

$$v_(F_c) = \begin{cases} v_F(1 - F_c/F_S) & \text{for } F_c \leq F_S \\ v_B(1 - F_c/F_S) & \text{for } F_c > F_S \end{cases} \tag{4.2}$$

with the force-free forward (backward) velocity $v_F$ ($v_B$). Here, $F_S$ is the so-called stall force which determines the threshold force for a motor to still be able to walk in their preferred direction. For forces bigger than the stall force the motors are assumed to move in opposite direction.

The forces $F$ exerted on the motors by the cargo determine also their detachment rate $k_d(F)$ increases exponentially

$$k_d(F) = k_d^0 \exp\left(\frac{F}{F_D}\right) \tag{4.3}$$

with the force-free detachment rate $k_d^0$ and the detachment force $F_D$. Once the motors are detached they can attach again with a force-independent attachment rate $k_a$.

In the frame of the MF assumption, the model by Müller *et al.* predicts two entirely different motility states for different parameter ranges. The intuitive state where the cargo is stalled most of the time due to a situation where the two teams balance each other, is obtained when the stall force $F_S$ is much smaller than the detachment force $F_D$. The teams cannot rip each other off from the filament and will be referred to be *weak* in the following. The states are characterized by a velocity distribution which is peaked around zero velocity and for the distribution of attached motors the majority of the weight is on the diagonal where $n_+ = n_-$. The cargo barely moves as one can observe in Figure 4.2, column A.

The motion characteristics for $F_S > F_D$ are significantly different (Figure 4.2, column B). Those *strong* motors can take over and one teams usually wins the tug-of-war situation. In that case only one team is bound to the filament which results in a distribution of attached motors which is peaked around $(0, N_-)$ and $(N_+, 0)$. If solely one team is bound to the filament, the cargo velocity is equal to the force-free velocity of the single motors $v_F$ which is reflected by a bimodal velocity distribution - thus states which exhibit SBDs.

In the MF-model, these states originate from mechanical interactions without requiring any further regulatory mechanism. The presence of those SBDs arises due to a dynamic instability which has its origin in the non-linear force dependence of the motor's detachment rate [86].

A third scenario is a mix of the two above described ones, the velocity distribution, and the distribution of the number of attached motors in shown in Figure 4.2, column C. In that case the distributions are trimodal as they are combining the bimodal distribution with the single peak around zero velocity found for weak motors.

In their work Müeller *et al.* also discuss the case of asymmetric motors. The aim was to

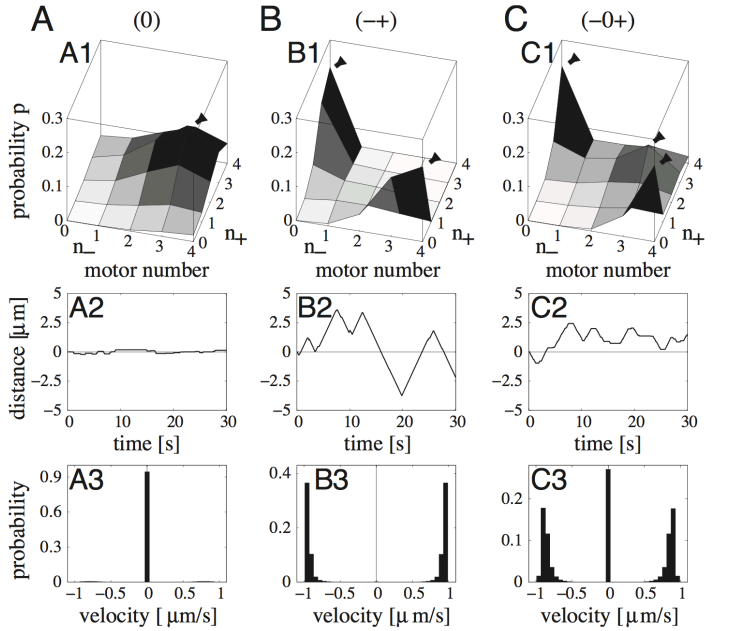


**Figure 4.2:** Motility states for the symmetric tug-of-war of $N_+ = N_- = 4$ plus and minus motors. The three columns A, B, and C correspond to the three motility states (0), $(-/+)$, and $(+0-)$, respectively. (A) The no-motion motility state (0) is characterized by motor number probabilities $p$ with a single maximum at an equal number of active plus and minus motors (A1), trajectories with almost no motion (A2), and velocity distributions with a single maximum at zero velocity (A3). (B) The motility state $(+/-)$ of fast bidirectional motion is characterized by probabilities $p$ with two maxima with only plus or only minus motors active (B1), trajectories which exhibit switching between fast plus and minus motion (B2), and bimodal velocity distributions with two peaks close to the single-motor velocities of $\pm$ 1 $\mu$m/s (B3). (C) The motility state $(+0-)$ is characterized by probabilities with three maxima corresponding to fast plus and minus and no motion (C1), trajectories that exhibit fast plus and minus motion and pauses (C2), and velocity distributions with three peaks (C3).

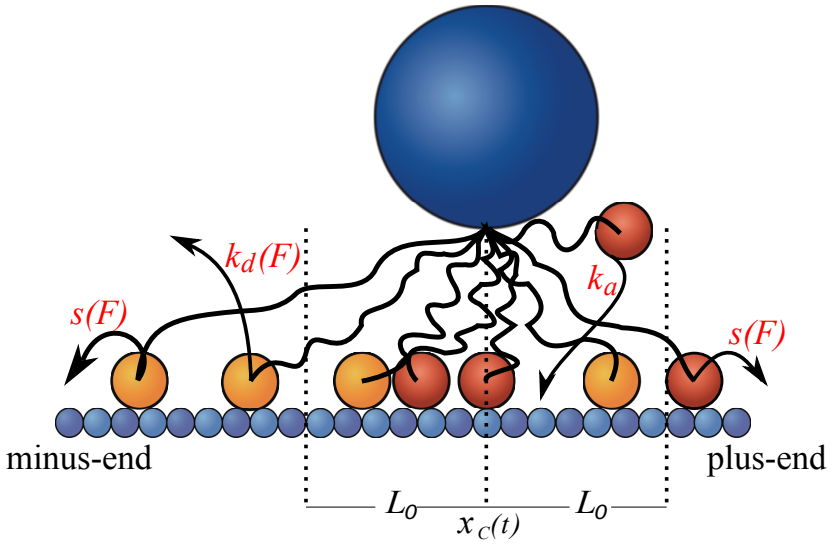


**Figure 4.3:** Sketch of the motor kinetics. A cargo (dark blue) is moved by two teams of motors pulling in "+" (red) and "-" (orange) direction, respectively. The single motors can walk on and detach from the filament. Once they are detached, they can attach again within the force free area $[x_C(t) - L_0, x_C(t) + L_0]$.

reproduce the run length distribution and the average run velocity depending on the run length found in a experiment with *Drosophila*-embryos [46]. Here they fit the parameter for the minus-motors to the data for the run length distribution and then compare the values for run length against run velocity with those found in the experiment. They find some good agreement for those quantities. Even though one has to question whether the run length is a stable quantity to measure. It depends strongly on arbitrary thresholds, both in space and time, for the minimum length of a run, a pause and a pause.

## 4.2 EPB model with symmetric motors

The MF-model of Müller *et al.* received a lot of attention because it predicts states with SBDs without any control mechanism. Especially for biologists this was a surprising and promising result. In this chapter a model inspired by Kunwar *et al.* [72] which takes every single motor position into account is analyzed, called EPB-model in the following. The aim of this analysis is to test whether SBDs exist even by taking each single motor as an individual into account.

### 4.2.1 Model definition

In the EPB-model the motors take steps along the filament as depicted in Figure 4.3. The single motors are modeled as cable-like springs with stiffness $\mathcal{K}$ such that they behave like linear springs once their stretched at a length bigger than the rest length $L_0$ and do not resist

compression [6,72]. This results in the force-position relation for the $i$-th motor

$$F_i(x_i - x_C(t)) = \begin{cases} \mathcal{K}(x_i - x_C(t) + L_0), & x_i - x_C(t) < -L_0 \\ 0, & |x_i - x_C(t)| < L_0 \\ \mathcal{K}(x_i - x_C(t) - L_0), & x_i - x_C(t) > L_0. \end{cases} \tag{4.4}$$

We want the model to be as similar as possible to the MF-model to make unambiguous conclusion about the existence of SBDs. For that reason a stepping rate $s(F_i)$ for the $i$-th motor to be linearly decreasing with increasing force is chosen in the following form

$$s(F_i) = \begin{cases} \frac{v_F}{d}(1 - F_i/F_S) & \text{for } F_i \leq F_S \\ \frac{v_B}{d}(1 - F_i/F_S) & \text{for } F_i > F_S \end{cases} \tag{4.5}$$

with the motor's step length $d$ and the same values for $v_F$, $v_B$ and $F_S$ as in the MF-model (compare eq. 4.2). Since in the EPB-model the motors step in a stochastic manner instead of the constantly moving cargo, the velocity $v_F$ is divided by the step length $d$ in order to receive a rate.

Furthermore, the detachment rate $k_d(F_i)$ is adopted from the MF-model such that it increases exponentially with increasing force

$$k_d(F_i) = k_d^0 \exp\left(\frac{|F_i|}{F_D}\right) \tag{4.6}$$

with the same detachment force $F_D$ and the force-free detachment rate $k_d^0$. It is assumed that the motors do not feel any force if they are detached from the filament. As in the MF-model a constant attachment rate $k_a$ is assumed for the EPB-model as well.

If not explicitly stated, we don't consider exclusion of the motors on the filament. The heads of the molecular motors bind to particular sites on microtubules and so it would in principle be necessary to consider exclusion effects. However, for microtubule based cargo transport the number of possible binding sites in close proximity of the cargo is much bigger compared to the number of attached motors [16, 20]. A brief discussion on the effects of exclusion as well as the influence of the force-free region $L_0$ on the cargo's motion can be found in the end of section 4.2.

Remember, that in the MF-model [86] the cargo velocity is simply a function of attached motors $n_\pm$ and is thus constant between two at-/detachment events. This implies that one team feels exactly the same force as the other one in opposed direction as long as no external force acts on the cargo.

In contrast, as we here take the individual motor steps into account the resulting force on the cargo is determined as the sum exerted by each single motor (eq. (4.4)). In the EPB-model a spherical cargo of mass $m$ with radius $R$ is propagated along its equation of motion

in a medium with viscosity $\eta$.

$$m\frac{\partial^2 x_C(t)}{\partial t^2} = -6\pi\eta R\frac{\partial x_C(t)}{\partial t} + \sum_{i=1}^{n_+ + n_-} F_i(x_C(t), \{x_i\}). \tag{4.7}$$

We keep for the reasons of generality the mass term in our model since it doesn't aggravate the numerical requirements even though it is not necessarily needed.

See Table A1 in the appendix for the set of parameters used in the simulations.

### 4.2.2 Results and discussion

The main question to be answered in this section is whether the EPB-model produces the same state with SBDs as it was seen for strong motors in the MF-model [86].

In contrast to the MF-model where the cargo velocity is constant, the cargo in the EPB model moves according to its equation of motion and, therefore, not with constant speed. This is why we discretize the trajectory and define $\overline{v}(t) = \frac{x_C(t+\Delta t) - x_C(t)}{\Delta t}$. to be able to compare the velocity distributions. Here we use $\Delta t = 0.16$ s [45, 86].

With the chosen set of parameters given in in the appendix in Table A1 the strong motors of the MF-model produce fast cargo motion with states that are characterized by SBDs (Figure 4.4**(a)**). However, taking all motors explicitly into account these states with SBDs are no longer observed (Figure 4.4**(b)**). We checked that this result is robust and does neither depend on the particular realization of the motor-cargo coupling nor the details of the motors' response to external forces or the chosen set of parameter.

For the EPB-model, the distribution of bound motors $p(n_+, n_-)$ in Figure 4.4**(b)** has a peaked structure on the diagonal which corresponds to states when the same number of motors of each team is bound to the filament. In the frame of the EPB-model, we can determine how many of those bound motors actually feel a force and so are engaged in the tug-of-war. We assume that also in real cells some motors do not experience any force (eg. Figure 2.4 (a)). This quantity $\tilde{p}(n_+, n_-)$ shown in Figure 4.4**(c)** demonstrates that in the EPB-model at a given time not all motors which are bound to the filament exert a force on the cargo. This contradicts the mean-field assumption where the motors within one team share the force equally. Once a motor detaches in the MF-model it results into a new cargo velocity and an new instantaneous equal sharing of the higher load between the remaining motors of the team, which most probably will also detach within a very short time due to the exponential detachment rate. In the EPB-model we assume that motors (can) have different positions. Figure 4.5 shows a trajectory of a cargo for which in the initial state only the team of minus-motors is attached to the filament. One reveals that this states is not stable in the EPB-model and that the motor that detaches most probably is the one most distant from the cargo. But in the frame of the EPB-model the remaining motors can establish a reservoir of bound motors of the same team behind. After a motor detachment, the cargo

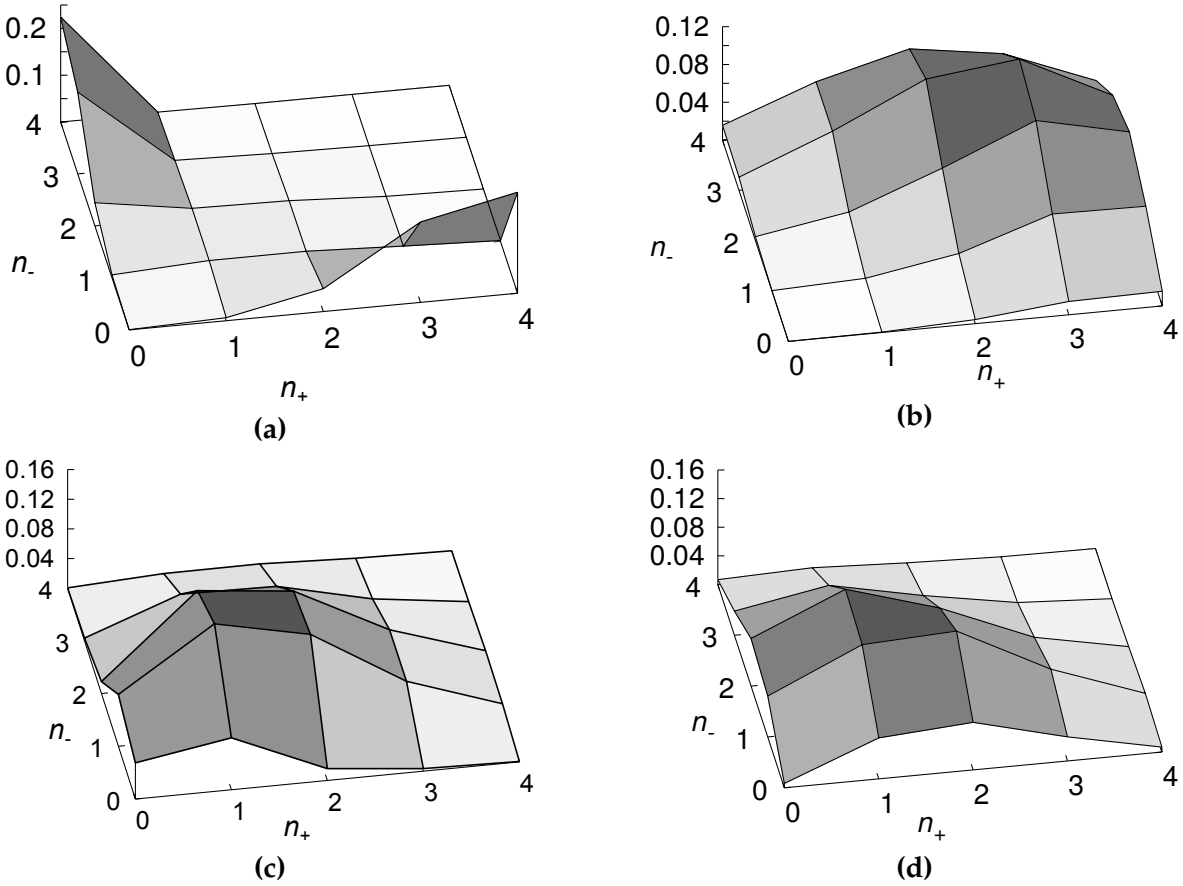


**Figure 4.4:** The probability $p(n_+, n_-)$ of $n_+$ "+"-motors and $n_-$ "−"-motors bound to the filament **(a)** in the MF-model and **(b)** for the EPB-model in the case of no activation and for $N = 4$. The probability $\tilde{p}(n_+, n_-)$ of +"-motors and $n_-$ "−"-motors which are actually engaged in the tug-of-war (i.e. which apply a non-zero force on the cargo) in the EPB-model is shown without activation in **(c)** and with a mutual activation with $a = 5$ and $R_A = 32$ nm in **(d)**.
Reprinted by permission from *Motility states in bidirectional cargo transport* EPL, 111(68005), 2015.

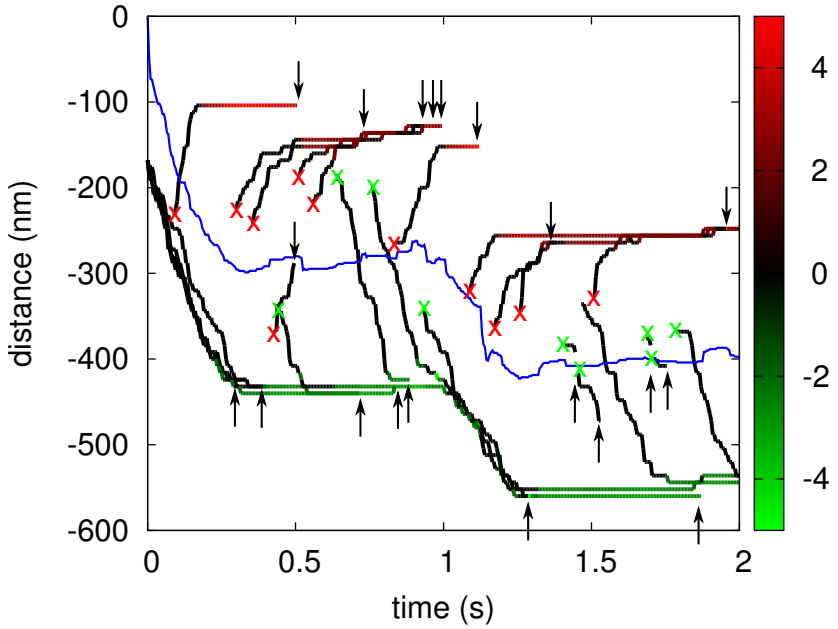


**Figure 4.5:** One specific realization of the trajectories of the cargo (blue) and of all "+"- (red) and "−"- (green) motors. The arrows indicate a detachment event and the crosses an attachment of a "+"- (red) or a "−"- (green) motor. The color code gives the ratio $k_d(F_i)/s_\pm(F_i)$. We choose as initial state a state that would have been stable in the MF case, with only "−"motors pulling on the cargo. We see here that this state is not stable for the EPB-model.
Reprinted by permission from *Motility states in bidirectional cargo transport* EPL, 111(68005), 2015.

can move backwards which results first in a new load sharing between both teams that is partly relaxed. Second, due to the backward motion of the cargo, some bound motors in the reservoir can become involved in the pulling of the cargo. Those motors can then replace the detached one. This effect makes obvious why we do not detect the detachment cascades as they are observed within the mean-field description, and why states with SBDs can be sustained only if equal load sharing is considered.

### Motor activation

In the previous discussion we pointed out that, in a reasonable parameter range, the MF-model can exhibit some states with SBDs which vanish once one takes the motor positions explicitly into account[1]. This is because the MF-assumption implicitly corresponds to a perfectly synchronous stepping between all attached motors within one team. In order to analyze the degree of synchronization needed to observe states with SBDs, some mutual motor activation is considered in the EPB-model. Here motors of the same team can activate each other and in this way introduce some artificial synchronous stepping.

This mutual motor activation is introduced as follows: If the $i$-th motor of one team takes

[1]We exclude the cases where only one motor at a time is pulling, for example in the case of a detachment rate much higher than the attachment rate. In these trivial cases no collective effect occurs anyhow.

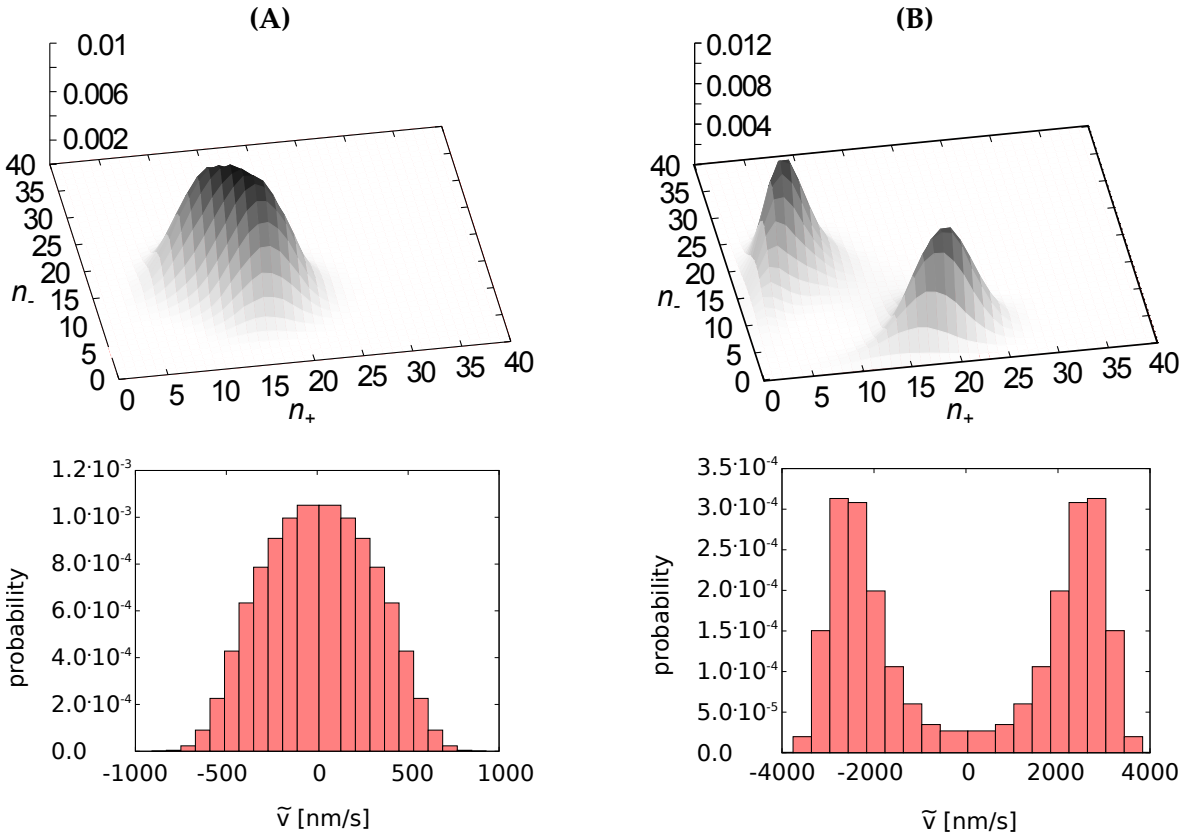


**Figure 4.6:** The probabilities $\tilde{p}(n_+, n_-)$ (top) and $p(\overline{v})$ (bottom) are shown for $a = 1$ (without activation) on the left hand side and for $a = 5$ and $R_A = 32$ nm on the right hand side. Note that the cargo's maximal velocity is now $a \cdot v_F$. Here $N = 40$.
Reprinted by permission from *Motility states in bidirectional cargo transport* EPL, 111(68005), 2015.

a step, the stepping rate of the motors of the same team within the the activation radius $[x_i - R_A, x_i + R_A]$ is multiplied by the activation factor $a$. For the simulations the completely arbitrary values $a = 5$ and $R_A = 32$ nm, i.e. 4 tubulin subunits are chosen. In subsection 4.2.2 the influence of $a$ shall be discussed in more detail.

First, we analyze the influence of this artificial activation for a rather small team ($N = 4$). We find that mutual activation does not significantly change the distribution of attached motors as depicted in Figure 4.4**(d)**. The probability to have no motor pulling $\tilde{p}(0, 0)$ decreases to almost zero. The "two against one"-scenarios $\tilde{p}(2, 1)$ and $\tilde{p}(1, 2)$ are slightly more probable. However, this is still far away from a double-peaked distribution.

In order to approach the mean-field limit the number of motors bound to the cargo is increased from $N_\pm = 4$ to $N_\pm = 40$. In column **(A)** of Figure 4.6 the probability of engaged motors $\tilde{p}(n_+, n_-)$ (top) and the velocity distribution $p(\overline{v})$ (bottom) without activation ($a = 1$) are shown. As before, the velocity distribution is peaked around zero and the configuration with the same number of motors pulling at the same time is still the most probable. If we now introduce a mutual motor activation with $a = 5$, we observe SBDs as shown in column

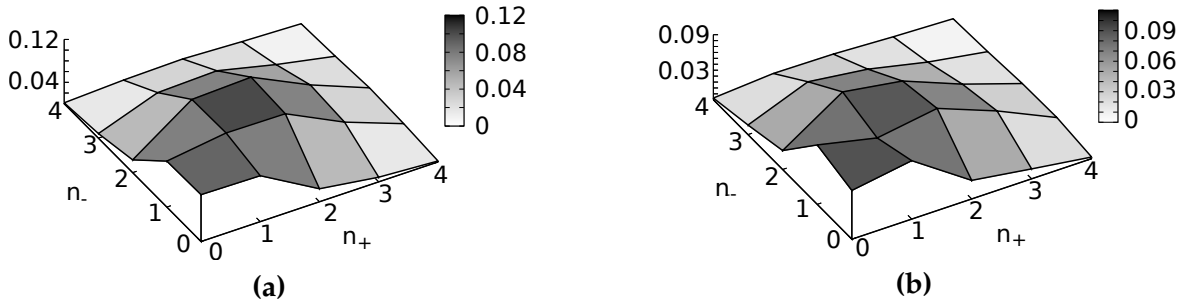


**Figure 4.7:** Probability of $n_+$ and $n_-$ motors engaged in the tug-of-war **(a)** without and **(b)** with mutual motor activation ($a = 5$, $R_A = 32$ nm) with exclusion on the filament.
Reprinted by permission from *Motility states in bidirectional cargo transport* EPL, 111(68005), 2015.

**(B)** of Figure 4.6 similarly as it was found in the MF-model. This hints that the mean-field assumption is relevant only in the limit of a high number of motors (much higher than observed in experiments) and if, in addition, a synchronization mechanism between the motors would exist. Thus we don't expect this case to be relevant for real cells.

### Influence of exclusion

For the results shown above no exclusion for the motors along the filament is considered. Since the heads of the molecular motors bind to particular sites on microtubules it would in principle be necessary to consider exclusion effects. For microtubule based cargo transport, however, the number of possible binding sites in close proximity of the cargo is much bigger compared to the number of attached motors [16,20]. However, its influence on the existence of SBDs shall be discussed here.

In Fig. 4.7 one sees easily that exclusion does not change the behavior qualitatively. Due to exclusive filament positions it is impossible for the motors to share the force equally since they cannot share the same filament position. Since the force is determined via the distance between the cargo and the motor head the motors all exert a different force. Within this scenario the probability to have several motors engaged in the tug-of-war at the same time even decreases which brings the system even further from the MF limit.

### Influence of $L_0$

Further we discuss the influence of the parameter $L_0$ on the cargo motion. This area around the cargo position $x_C(t)$ is crucial for the way the motors share forces since it acts as a reservoir of force-free motors which can jump in the breach for the other motors within the same team. In the following we consider two situations: $L_0 = 0$ and $L_0 = L_0^*/2$ where $L_0^*$ is the value of $L_0$ given in table A1 in the appendix.

In the case of $L_0 = L_0^*/2$ the distribution of attached motors does not change significantly. It slightly broadens but the main weight is still on the diagonal and so on configurations with

the same number of motors per team engaged in the tug-of-war. This changes for $L_0 = 0$ (Figure 4.8 (c,d)). We find a non-vanishing probability for configurations where one team gains the upper hand. For this reason we also give the velocity distribution (Figure 4.8 (e),(f)) for $L_0 = 0$. One observes that they are no longer Gaussian but still unimodal and with fat tails.

We can, additionally to the reduced rest length, consider mutual motor activation. The distribution of attached motors in the case $L_0 = L_0^*/2$ is not significantly altered (Figure 4.8 (b)). On the contrary, the distribution becomes double peaked for $L_0 = 0$ and an activation of $a = 5$ (Figure 4.8 (d)). However, even in this case the effect on the velocity distribution is marginal (see Figure 4.8 (f)). The distribution remains unimodal with a major peak around zero velocity but two shoulders around 2000 nm/s appear. Note that the increase in cargo velocity compared to the force-free motor velocity results from the activation factor $a$ which is multiplied with the stepping rate $s(F)$ as defined in eq. (4.5).

Taking $L_0 = 0$ brings the system closer to the MF limit since the motors cannot build up a reservoir of motors which do not feel any force. Also the fact that the motors are all closer to each other reinforces the effect of activation. This explains the appearance of shoulders in the velocity distribution. But even in this more favorable case for a MF-limit the system does not recover SBDs.

**Influence of (strong) activation**

To approach the MF-limit some mutual activation was introduced above as an artificial synchronization between the motors. In this subsection it it analyzed how much the number of motors and the activation factor influence the cargo's motion. We define $M$ as the sum of the probabilities to have the same number of motors per team engaged in the tug of war

$$M := \sum_{i}^{N} \tilde{p}(i, i). \tag{4.8}$$

This gives a rough estimation of the weight of double peaked distributions. In Fig. 4.9 we show $M$ against $N$ for different activation factors $a$ and also the value found in the MF-model. One sees that the effective synchronizations is mainly governed by the number of motors and not on the (arbitrarily chosen) value of $a$. For modeling real intracellular transport a small number of motors is relevant. We show that even for a very strong activation ($a = 35$) the MF-limit of $M = 0.034$ for $N = 4$ is not reached. With the EPB-model we cannot reach this small value, not even for $N_\pm = 18$ .

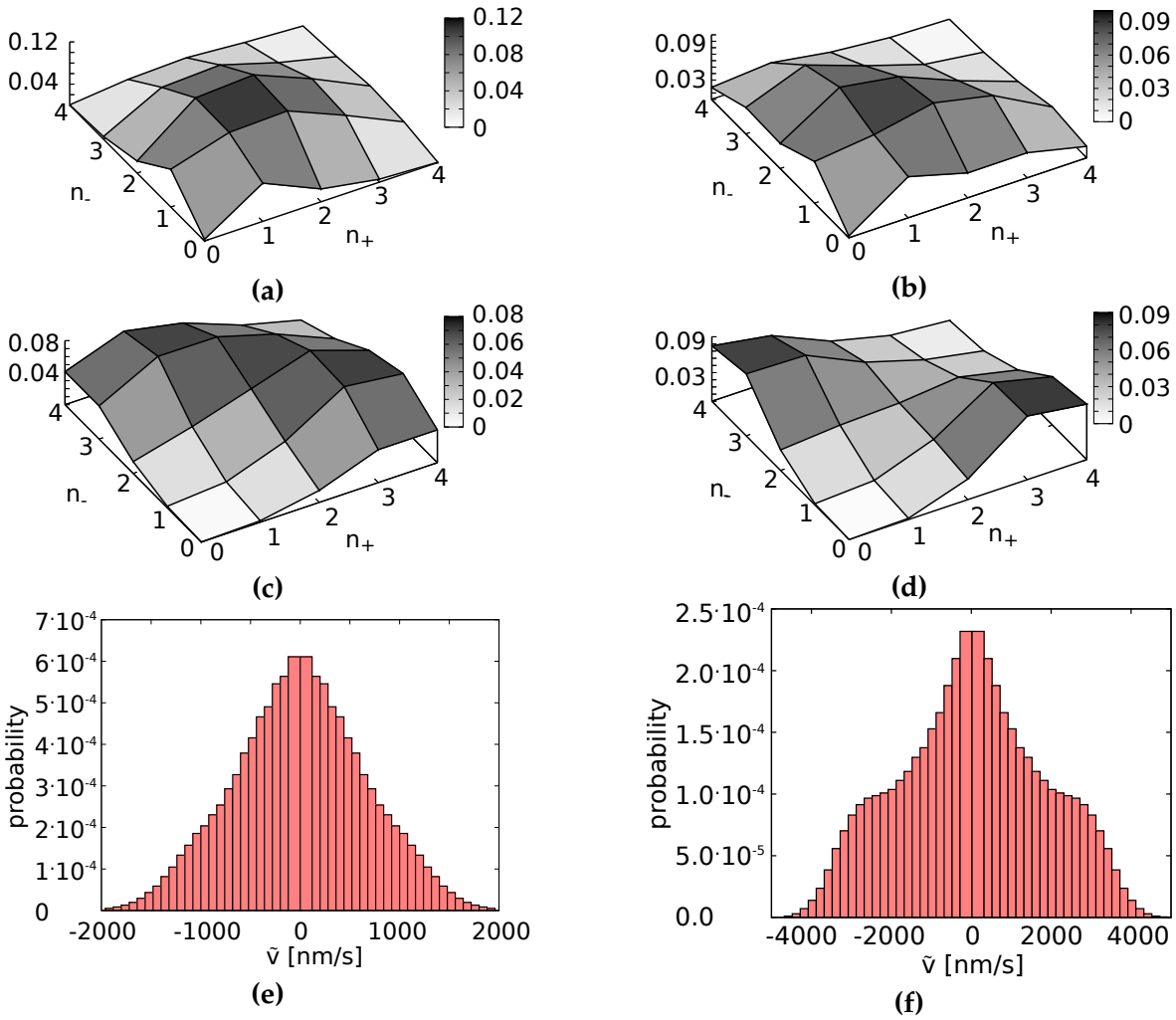


**Figure 4.8:** Probability of $n_+$ and $n_-$ motors engaged in the tug-of-war **(a,c)** without and **(b,d)** with mutual motor activation ($a = 5$, $R_A = 32$ nm) with **(a,b)** $L_0 = 55$ nm and **(c,d)** $L_0 = 0$ nm. Probability of a cargo velocity $\tilde{v}$ **(e)** without and **(f)** with mutual motor activation ($a = 5$, $R_A = 32$ nm) with $L_0 = 0$ nm. All these figures are for $N = 4$.
Reprinted by permission from *Motility states in bidirectional cargo transport* EPL, 111(68005), 2015.

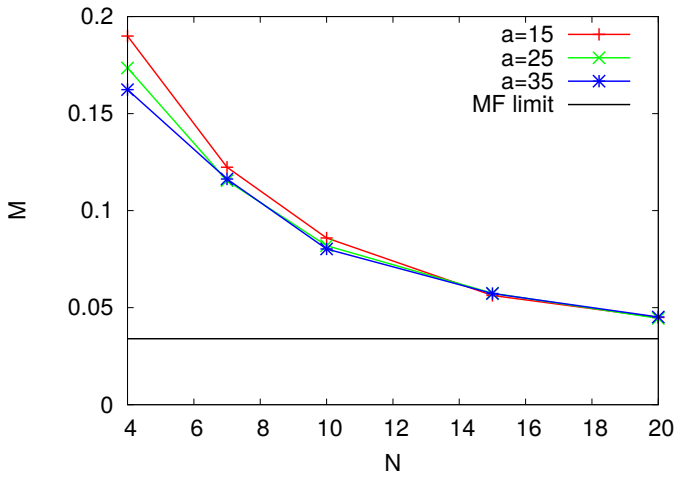


**Figure 4.9:** Probability weight on the diagonal $M$ as defined in eq. (4.8) against number of motors for different activation factors $a$. For comparison, the black curve gives the value obtained for $N = 4$ in the MF model.
Reprinted by permission from *Motility states in bidirectional cargo transport* EPL, 111(68005), 2015.

## 4.3 EPB model with "biological" motors

As it was shown in the section above, position fluctuations are crucial in order to describe cargo transport by teams of molecular motors. In order to obtain biologically relevant predictions for cargo transported by two teams of motors, we will take the differences for kinesin and dynein motors into account and discuss their influence in the frame of the EPB-model [62]. Hence, the parameters for the two teams of motors will not be chosen symmetrically anymore but the experimentally measured characteristics will be used.

### 4.3.1 Model definition

In section 2.2 it is discussed that ATP has a crucial influence on the dynamics of molecular motors. For this reason we consider now the influence on the motors' motility of the cellular ATP level additionally to the force they feel.

If two competing teams are bound to one cargo, the force is usually acting against the preferred stepping direction of the motor such that it may slow down, stop or even invert its direction. In general we divide the force scale in two regimes for the stepping and detaching behavior, depending whether the applied force is smaller than the stall force $F_S$ (regime I) or larger (regime II). We first concentrate on the stepping rate. Schnitzer *et al.* [100] introduced a model for regime I which bases on a Michaelis-Menten equation. The original one

$$v = C \cdot \Phi \cdot \frac{[S_e]}{[S_e] + k}, \tag{4.9}$$

as it was first introduced by Michaelis and Menten in 1913 aimed to describe enzymatic reaction processes [2] [85]. This particular shape for the reaction rate is characteristic for processes in which reactions are catalyzed by a catalyst $S_e$ and therefore the associated reaction rates increase with increasing catalyst concentration until it saturates and reaches the value $C \cdot \Phi$. The same happens for the molecular motor. They reach a maximum velocity at saturating ATP concentration ($v_F$). As long as the force is equal to zero the above given formula describes well the motor stepping in dependence of the ATP concentration.

However, in the EPB-model it is crucial to take the force exerted on the motor into account as well. With increasing force the motor's stepping rate decreases. One way to describe these competing counterparts is a coupled Michaelis-Menten equation [100]

$$s(F_i, [ATP]) = \frac{k_{\text{cat}}(F_i)[ATP]}{[ATP] + k_{\text{cat}}(F_i) \cdot k_{\text{b}}(F_i)^{-1}}, \tag{4.10}$$

where $k_{\text{cat}}$ is the rate constant for the ATP catalysis, $k_{\text{b}}$ is a second-order rate constant for ATP binding. Both rates depend on the load force. As the stepping rate decreases with increasing absolute force $|F_i|$, $k_{\text{b}}(|F_i|)$ declines faster with force than $k_{\text{cat}}(|F_i|)$. Schnitzer *et al.* [100] introduce a Boltzmann-type force relation for the rate constants

$$k_j(F_i) = \frac{k_j^0}{p_j + q_j \exp(\beta F_i \Delta)} \qquad j = \{\text{cat, b}\} \tag{4.11}$$

with constants $k_j$, $p_j + q_j = 1$ and $\beta = (k_{\text{b}}T)^{-1}$. It was shown for kinesin [100] and dynein [117] that the stepping rate as given in (4.10) gives good agreement with experimental data.

For the model here it is further assumed that dynein's stall force varies with the ATP concentration in an affine linear manner until it saturates [83]. This determines $\Delta$ defined in (4.11). To ensure that the stepping rate is much smaller than 1, once the stall force is reached, we define as a lower boundary

$$\frac{k_{\text{cat}}(F_S)[ATP]}{[ATP] + k_{\text{cat}}(F_S) \cdot k_{\text{b}}(F_S)^{-1}} = 10^{-13}\ \text{s}^{-1}, \tag{4.12}$$

where $k_{\text{cat}}^0$, $k_{\text{b}}^0$, $q_{\text{cat}}$ and $q_{\text{b}}$ from Schnitzer *et al.* [100] are used, and given in the appendix in Table A2. In contrast we keep kinesin's stall force constant in the experimentally relevant regime [67].

In regime II (+end motors: $F_i \geq F_S$ / -end motors $-F_S \geq F_i$) the force is (in absolute value) bigger than the stall force and so the motors walk against their preferred stepping direction with constant velocity $v_B$

$$s(F_i) = \frac{v_B}{d}, \tag{4.13}$$

[2] $v$: reaction rate, $C$ proportionality constant, $\Phi$: total molar enzyme concentration, $[S_e]$: concentration of free sucrose, $k$: dissociation constant which was later on called the *Michaelis-Menten constant*

which is at least one order smaller than the force-free forward velocity $v_F$.

In this version of the EPB-model with biologically more relevant motility characteristics we also divide the detachment rate in the two above mentioned regimes. We choose the detachment behavior according to [72]

$$k_d^+(F_i) = \begin{cases} k_d^0 \exp\left(\frac{|F_i|}{2.5f}\right) & F_i < F_S \\ k_d^0 \left(0.186\frac{|F_i|}{f} + 1.535\right) & F_i \geq F_S \end{cases} \tag{4.14}$$

for kinesin and

$$k_d^-(F_i) = \begin{cases} k_d^0 \exp\left(\frac{|F_i|}{2.5f}\right) & F_i > -F_S \\ k_d^0 \left[1.5\left(1 - \exp\left(\frac{-|F_i|}{1.97f}\right)\right)\right]^{-1} & F_i \leq -F_S \end{cases} \tag{4.15}$$

for dynein. We introduce here a standardization force $f = 1$ pN which determines the force scale. Note that the two types of motors behave quite differently above stall. While kinesin's detachment rate increases linearly with the force in regime II we implement a catch-bond like rate (decreasing with $F_i$) for dynein.

The cargo propagates again along its equation of motion given in eq. (4.7).

### 4.3.2 Environmental influence

At first the distribution of the cargo displacement for one-minute intervals (see Fig. 4.10) is measured in order to examine whether the two teams are balanced with the chosen set of parameters given in the appendix in Table A2. The obtained results show that by changing the ATP concentration the mean velocity (or cargo displacement per time unit) of the transported cargo can be tuned continuously. Remarkably, the cargo effectively *slows down with increasing* ATP-concentration until the bias vanishes (at an ATP concentration of $0.62$ mM for our choice of the parameters). By increasing the ATP concentration the bias is inverted and its absolute value increases again which results in an effective speed up. In cells often signaling processes up- or down-regulate the activity of one single motor species. In the model presented here both motors are affected in the same way by changing the the ATP concentration. However, the reaction to this increase in the ATP concentration shifts the balance of power in favor of dynein. It is less probable that it detaches with increasing ATP concentration and so the mean displacement is towards the minus-end. Furthermore, one notices that an unbiased motion of the cargo can only be obtained in a rather narrow interval of ATP-concentration. For this reason one should in general expect a biased motion as long as two teams of different motors are attached to one cargo.

As already explained above, the stepping rate of the motors does not only depend on the ATP concentration but also on the force the motor feels. Additionally to the forces exerted by the other team of motors, an external force can occur in a cell. This can be an active force, e.g. myosin motors which are attached to the actin filament could pull on the cargo ass well.

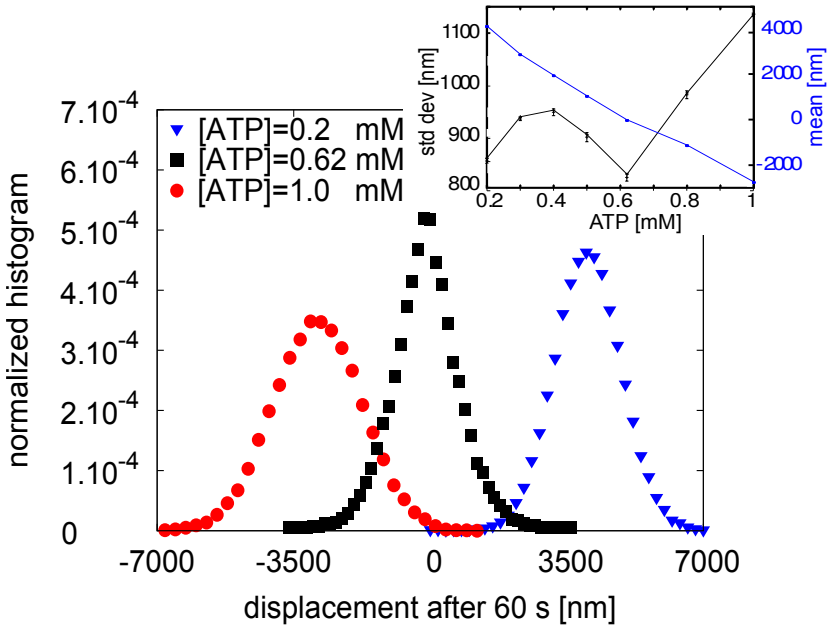


**Figure 4.10:** Normalized histogram of the displacement after 60 s of cargo propagation. The red circles correspond to [ATP]$= 0.2$ mM, the black squares to [ATP]$= 0.62$ mM and the blue triangles to [ATP]$= 1.0$ mM. We get for the mean displacement $\mu_{0.2} = 4028.3 \pm 1.14$ nm and the standard deviation $\sigma_{0.2} = 855.9 \pm 1.13$ nm for [ATP] = 0.2 mM, $\mu_{1.0} = -2887.5 \pm 3.17$ nm and $\sigma_{1.0} = 1139.9 \pm 2.59$ nm for [ATP] = 1.0 mM and $\mu_{0.62} = -27.8 \pm 14.08$ nm and $\sigma_{0.62} = 836.9 \pm 11.5$ nm for [ATP] = 0.62 mM. Obviously, the displacement changes direction from plus-end bias for stronger plus motors at low [ATP] to minus-end bias at saturating [ATP]. The inset shows the non-monotonous curve of the standard deviation of the displacement (black) against the ATP concentration while the mean displacement (blue) decreases monotonously.
Reprinted by permission from *Environmental control of microtubule-based bidirectional cargo transport*, EPL, 107(1):18004, 2014.

But also passive forces due to the crowded environment can influence the cargo's motion. Here, this crowded situation is modeled via an effective viscosity $\eta$. In Fig. 4.11 the mean displacement is shown for different ATP concentrations and different viscosities. Obviously, the influence of the bias on the viscosity is non-trivial. Counter-intuitively, an increasing viscosity can effect an increase in the absolute value of the bias. Another interesting effect occurs at intermediate ATP concentrations (see, e.g., 0.7 mM in Fig. 4.11 ): the cargo changes the direction of the mean displacement with increasing viscosity. For intracellular transport this effect can be used in order to leave crowded areas. Via this mechanism the efficiency of the motor-driven transport is enhanced. Here we find that the bias can be inverted for a limited range of ATP concentration. Note, that a change in $N_+$, $N_-$ modifies the values of the external control parameters at which the reversal of the bias is observed in the EPB-model.

As already discussed in the section 4.2 the discrete motor stepping with the cable-like force relation induces a time-correlated motion of the cargo. In Fig. 4.10 one sees that these correlations lead to non-Gaussian displacement distributions of the cargo at short finite time

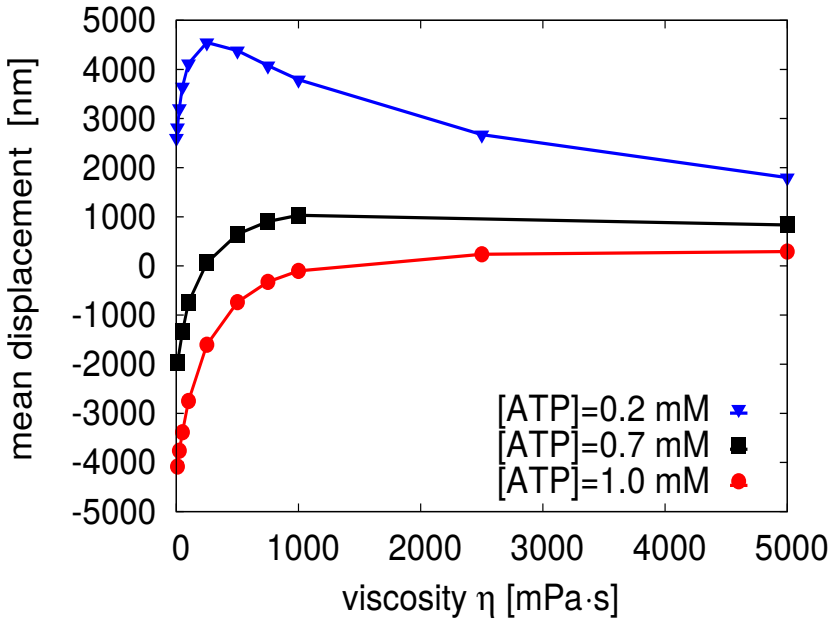


**Figure 4.11:** Mean displacement after 60 s of cargo propagation for different cytoskeleton viscosities $\eta$. The red circles corresponds to the [ATP]$= 0.2$ mM, the black squares to [ATP]$= 0.7$ mM and the blue triangles to [ATP]$= 1.0$ mM. For small [ATP] the mean displacement-viscosity relation shows a non-monotonous behavior. In the case of [ATP]=0.7 mM we observe a change in direction with increasing viscosity.
Reprinted by permission from *Environmental control of microtubule-based bidirectional cargo transport*, EPL, 107(1):18004, 2014.

intervals. One possible way to estimate the length of these temporal correlations is by means of the cargo's displacement variance against time. From our simulation results in Figure 4.12 one see that a transition from enhanced diffusion at short times to normal diffusion occurs. For the set of parameters used here one observes that the variance is growing as $t^{3/2}$ at short time scales. This superdiffusive behavior indicates cooperation between motors induced by the cargo-mediated coupling. This can be explained by assuming that a stretched plus-motor takes a step. In that case the cargo moves towards the plus end and so increases the force on the minus-motors while at the same time the force acting on the remaining plus-motors decreases. For that reason it is more likely that also the next motor step goes in direction of the plus end corresponding to a persistent random walk. Furthermore, the inset of Figure 4.12 shows that the exponent is not universal as it was assumed in several publications [22, 96]. Simply by varying the attachment rate, which can be changed for instance by microtubule-associated proteins [105], it is possible to observe exponents in the range from 1.4 to 1.6. Those exponents are in the same range as observed experimentally [22, 71].

In the unconfined one-dimensional model a purely (biased or unbiased) diffusive behavior is observed asymptotically. This regime is generic for our model as long as we do not assume cargo motion on a network since the correlation times are finite. By contrast, on a

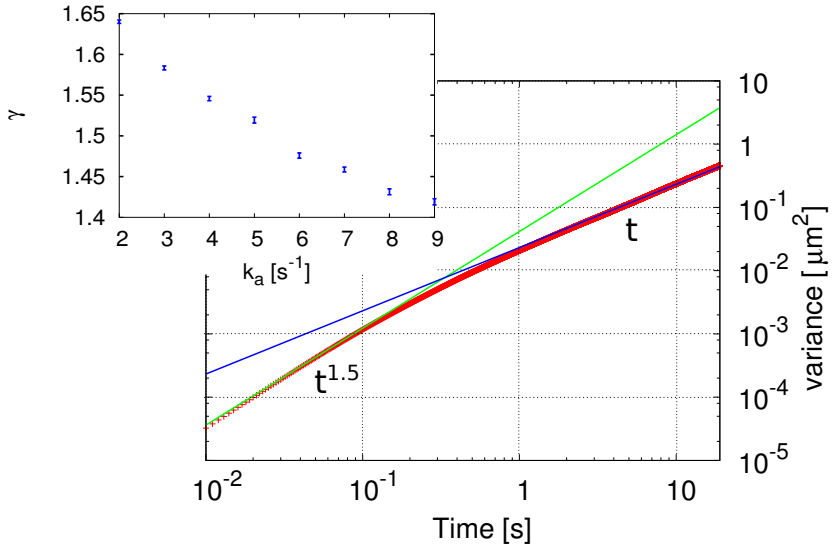


**Figure 4.12:** Variance of the numerically generated trajectories with [ATP]=1 mM. One observes at 0.5 s a crossover from enhanced diffusion going with $t^\alpha, \alpha = 1.5$ (green line) to normal diffusion proportional to $t$ with a diffusion coefficient $D = 0.04\mu\text{m}^2\text{s}^{-1}$ (blue line). The inset shows how the exponent varies with the attachment rate $k_a$.
Reprinted by permission from *Environmental control of microtubule-based bidirectional cargo transport*, EPL, 107(1):18004, 2014.

branched microtubule network the asymptotic behavior may be influenced by the structure of the network as shown in case of the microtubule-network of giant fibroblast [22], where sub-diffusive behavior has been observed. Theoretically, this effect has also been shown by Shaebani *et al.* [106].

### 4.3.3 Influence of thermal fluctuations

In the previous sections the cargo motion was deterministic between two motor events. In this section we will discuss in which way thermal fluctuations influence the cargo motion and which effects occur due to this stochastic force. Instead of the equation of motion we then need to solve the Langevin equation

$$m\frac{\partial^2 x_C(t)}{\partial t^2} = -\beta\frac{\partial x_C(t)}{\partial t} + F(x_C(t), \{x_i\}) + F_{\text{therm}}(t) \tag{4.16}$$

which contains additionally the stochastic force $F_{\text{therm}}(t) = \sqrt{2k_BT\beta}\xi(t)$ due to thermal fluctuations inside a cell. Here $k_B$ is the Boltzmann constant, $T$ the temperature and $\xi(t)$ a normalized white-noise process, hence

$$\langle\xi(t)\rangle = 0 \quad \text{and} \quad \langle\xi(t)\xi(t')\rangle = \delta(t-t') \quad \forall\, t, t'. \tag{4.17}$$

Note, that $\beta = 6\pi\eta R$ is still the friction coefficient and not the inverse temperature.

The aim is still to describe the cargo motion in continuous time to know its position at every single time $t$. This ensures that we do not miss any force fluctuation exerted on the motors. In contrast to the previous sections this evolution equation requires a specific treatment due to the thermal noise term. In [42,90] a stochastic procedure was developed in order to generate at discrete times some fluctuations in the cargo trajectory, with the same amplitude as would result from the integration of the Langevin equation. We follow this procedure and additionally to the motor events we define the times at which these thermal fluctuations are included as "shot events".

At each shot event $E_i$ at time $t_{E_i}$, two independent random numbers $\varphi_i$ and $\zeta_i$ are drawn from a Gaussian distribution with zero-mean and unit-variance. Between two shot events some time-dependent contributions to the position $x_C^{\text{therm}}$ and to the velocity $v_C^{\text{therm}}$ occurring due to the thermal noise build up, according to the expressions [42,90]

$$x_C^{\text{therm}}(t-t_{E_i}) = \sigma_{xx}(t-t_{E_i})\varphi_i \tag{4.18a}$$

$$v_C^{\text{therm}}(t-t_{E_i}) = \frac{\sigma_{xv}(t-t_{E_i})^2}{\sigma_{xx}(t-t_{E_i})}\varphi_i + \sqrt{\sigma_{vv}(t-t_{E_i})^2 - \frac{\sigma_{xv}(t-t_{E_i})^4}{\sigma_{xx}(t-t_{E_i})^2}}\zeta_i. \tag{4.18b}$$

In order to give the expressions for $\sigma_{xx}(\epsilon)$, $\sigma_{xv}(\epsilon)$ and $\sigma_{vv}(\epsilon)$ given in eq. (4.18a) we define the diffusion coefficient $D = k_B T/\beta$, the cyclic frequencies of the damped and the undamped harmonic potential $\omega = (\beta^2/4m^2 - \alpha/m)^{\frac{1}{2}}$ and $\omega_0 = (\alpha/m)^{\frac{1}{2}}$ respectively and the characteristic time in the presence of frictional forces $\tau = m/\beta$ is. The $\sigma_{i,j}$ (here $i,j = \{x,v\}$) depend explicitly on time $\epsilon \in [t_{E_i}, t]$. We have

$$\begin{aligned}\sigma_{xx}(\epsilon)^2 =& \frac{D}{4\omega^2\omega_0^2\tau^3}\cdot\Bigg(4\omega^2\tau^2 - \frac{1}{2}\Big[\exp\left(-\epsilon_i\tau^{-1} + 2\omega\epsilon_i\right)(1+2\omega\tau) \\ &+ \exp\left(-\epsilon_i\tau^{-1} - 2\omega\epsilon_i\right)(1-2\omega\tau)\Big] + (1-4\omega^2\tau^2)\exp(-\epsilon_i\tau^{-1})\Bigg)\end{aligned} \tag{4.19}$$

$$\begin{aligned}\sigma_{xv}(\epsilon)^2 =& \frac{D}{4\omega^2\tau^3}\cdot\Bigg(4\omega^2\tau^2 - \frac{1}{2}\Big[\exp\left(-\epsilon_i\tau^{-1} + 2\omega\epsilon_i\right)(1-2\omega\tau) \\ &+ \exp\left(-\epsilon_i\tau^{-1} - 2\omega\epsilon_i\right)(1+2\omega\tau)\Big] + (1-4\omega^2\tau^2)\exp\left(-\epsilon_i\tau^{-1}\right)\Bigg)\end{aligned} \tag{4.20}$$

and

$$\sigma_{vv}(\epsilon)^2 = \frac{D}{\omega^2\tau^2}\Big(\exp\left(-\epsilon_i\tau^{-1} + 2\omega\epsilon_i\right) + \exp\left(-\epsilon_i\tau^{-1} - 2\omega\epsilon_i\right) - 2\exp\left(-\epsilon_i\tau^{-1}\right)\Big). \tag{4.21}$$

Here, $\sigma_{xx}$, $\sigma_{xv}$ and $\sigma_{vv}$ are the elements of the variance-covariance matrix which fully characterizes a Gaussian distribution [42,90]. One checks easily that the relations $x_C^{\text{therm}}(0) = v_C^{\text{therm}}(0) = 0$ hold to ensure continuous cargo motion. Assuming that no motor event took

place before the next shot event at time $t_{E_{i+1}}$ the contributions to the position and velocity due to thermal fluctuations are added to the cargo components. We split the time-dependent contributions in two parts: the first one occurs because of the deterministic propagation due to the motor configuration $x_C^d$ while the second part comes from the thermal noise terms $x_C^{\text{therm}}$. The same counts for the cargo velocity.

$$x_C(t_{E_{i+1}}) = x_C^d(t_{E_{i+1}}) + x_C^{\text{therm}}(t_{E_{i+1}} - t_{E_i}) \tag{4.22a}$$

$$v_C(t_{E_{i+1}}) = v_C^d(t_{E_{i+1}}) + v_C^{\text{therm}}(t_{E_{i+1}} - t_{E_i}) \tag{4.22b}$$

After each shot event two new random numbers $\varphi_i$ and $\zeta_i$ are drawn.

The cargo trajectory is then interspersed by two types of events: motor events and shot events. In order to predict the next event time with Gillespie's algorithm [41] we need to know the cargo position in continuous time. With the algorithm introduced above, however, we know the cargo position and velocity at the shot events only. For this reason we interpolate the trajectory between shot events by generalizing the expression (4.22a) to

$$x_C(t) = x_C^d(t) + x_C^{\text{therm}}(t - t_{E_i}) \tag{4.23}$$

for all times $t_{E_i} \leq t < t_{E_{i+1}}$ between the two successive shot events $E_i$ and $E_{i+1}$. Note, that the interpolation is the only approximation we use here to propagate the cargo while all other steps are exact. The thermal contributions themselves added at discrete times have the same statistics as those that would be obtained from the direct solution of the Langevin equation, as proved in [42,90]. In order to ensure that this approximation does not affect the statistics we need to chose a shot frequency which is high enough. Even though the long time behavior of the cargo shall be analyzed we must use a shot rate $k_s$ which is still numerically treatable. In the following we use $k_s = 10^5$ s$^{-1}$ which is at least hundred times bigger than the average single motor event rate. We checked that our choice for $k_S$ is sufficient to avoid discretization effects.

First, the focus is on how the variance of the cargo displacement evolves with time and to check whether differences to the behavior described in section 4.3.2 occur. Secondly, the system will be confined via a viscous barrier in order to investigate its influence on the transport efficiency.

For completeness all simulation parameters are given in the appendix in Table A2.

**Cargo's displacement Variance**

In section 4.3.2 we found that the variance of the cargo displacement shows some superdiffusive behavior at times between 10 ms and 1 s. In the following we analyze the effect of thermal noise on even smaller time scales. We calculate in the same way as before the vari-

ance of the cargo trajectories as given in eq. (2.1). We carefully checked that the results do not depend on the initial conditions and the choice of $k_s$. Using the set of parameters given in the appendix in Table A2 we observe for times smaller than 10 ms that the cargo shows subdiffusive behavior with an exponent $\alpha = 0.6$. For longer times a cross-over from sub- to superdiffusion with an exponent $\alpha = 1.3$ is found as shown in Fig. 4.13. The thermal noise acting on a cargo without any motors attached would generate purely diffusive motion with $\alpha = 1$. Here, as the motors contribute with a harmonic potential created by the linear springs, the exponent $\alpha$ decreases. The superdiffusion occurs for the same reason as before - the motor steps create positive temporal correlations. Compared to a value of $\alpha \approx 1.5$ in the superdiffusive regime of section 4.3.2 a smaller exponent is obtained here due to the thermal noise. This stochastic contribution affects the correlations that are built up by the motors.

In order to check the relevance of our results we compare them to experimental results. Kuliç *et al.* [71] calculated the time-dependent MSD from particle trajectories in *Drosophila* S2 cells. In their work a crossover from sub- to superdiffusive has been reported at $\Delta t \approx 30$ms. For short times they obtained a subdiffusive exponent $\alpha = 0.59 \pm 0.28$. This exponent varied for different trajectories from 0.2 to 1.2. In the superdiffusive regime ($\Delta t > 30$ ms), the mean exponent $\alpha = 1.62 \pm 0.29$ has been measured, where also here the results for single trajectories varied in the range of 1.2 to 2. These *in vivo* results are in a remarkable good agreement with the theoretical ones from the EPB-model with thermal noise in the subdiffusive regime. For those small times we checked that variance and MSD do not differ significantly. In section 2.2.3 we have already discussed that measuring the MSD does not give unambiguous results in a regime where the MSD goes with an exponent $1 < \alpha < 2$. Especially, with the results we presented in section 4.3.2 which show that only for a very small parameter range the motion is unbiased, an exponent bigger than one could simply result from a biased bidirectional motion and not from correlations. For this reason the exponent of $\alpha = 1.3$ does not contradict the bigger exponent found in the study by Kuliç *et al.* [71].

As mentioned in section 2.2.3 in [71] it was claimed that enhanced diffusion occurs due to the bending and relaxation of MTs. They observed in the cargo trajectories non-constant velocities, indicating the involvement of microtubule elastohydrodynamics. By means of the EPB-model the same type of relaxation is observed in the cargo trajectories, indicating that the elastic relaxation of the MTs is not necessarily needed to observe this motion.

**Viscous barrier**

As discussed in section 2.1 the cell has a highly complex internal structure. For this, different regions can be differently crowded. In a very crowded compartment of the cell the effective viscosity can be much bigger than viscosity of pure water which corresponds to the viscosity

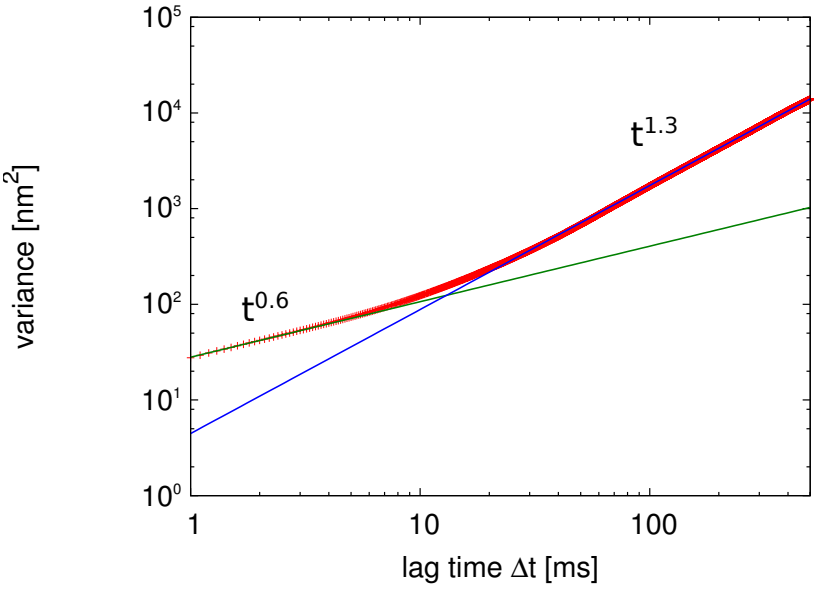


**Figure 4.13:** Variance of the cargo pulled by $N+ = N_- = 5$ motors through a viscous medium. At short times the cargo shows subdiffusive behavior $\sim \Delta t^{\alpha}$ with an exponent $\alpha = 0.6$. For times $t > 10$ ms the cargo moves superdiffusively with $\alpha = 1.3$.
Reprinted by permission from *Fluctuation effects in bidirectional cargo transport* EPJST, 223(14):3215–3225, 2014.

of the cytosol. We have seen in section 4.3.2 that the effective viscosity strongly affects the overall bias of a cargo transported by two teams of motors. Therefore, we introduce in this section a symmetric structure along the one-dimensional track. A crowded cellular region is considered here as a region of high effective viscosity. In order to quantify the efficiency of bidirectional active transport we compare its motion to a purely diffusive particle of the same size in the same environment.

In order to realize those crowded areas we use two viscous barriers with increased effective viscosity $\eta^*$ and with a given length $L_B$ at positions $\pm x_B$ (depicted in Figure 4.14). In Figure 4.15 the mean first passage time (FPT) $\langle t_{\text{FPT}} \rangle$ of a particle to reach the position $\pm x_B \pm L_B$ starting at position $x_0 = 0$ is shown. To be able to come to a conclusion about the time needed to cross the barrier the mean FPT is compared on the one hand for the purely diffusive case (green curve in Fig. 4.15) and on the other hand to the barrier-free case that corresponds to $\eta^* = \eta$ as well (Fig. 4.15**(a)**).

Interestingly, in the case of low barrier viscosities $\eta^*$ and unbiased cargo dynamics (Fig. 4.15**(a)**) pure diffusion outperforms the active transport of cargo. Irrespective of the chosen barrier length our results for the mean FPT are much longer in case of actively transported cargos as compared to diffusion, for which exact results for the mean FPT

$$\langle t_{\text{FPT}} \rangle = \frac{\beta}{2k_B T}(x_B + L_B)^2 \tag{4.24}$$

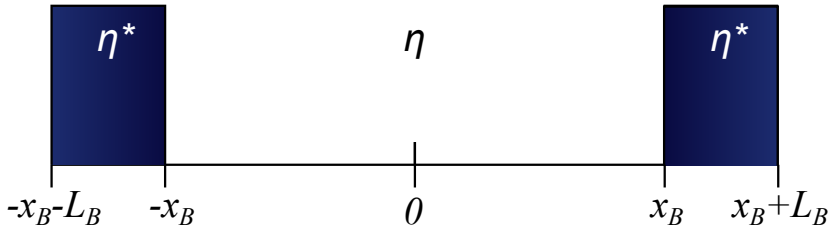


**Figure 4.14:** Sketch of the arrangement of the barriers. The blue rectangles represent the area of increased viscosity $\eta^*$.
Reprinted by permission from *Fluctuation effects in bidirectional cargo transport* EPJST, 223(14):3215–3225, 2014.

are known [94], with $\beta = 6\pi\eta R$. With slightly increased viscosity in the barrier ($\eta^* = 10\eta$) the diffusion is still faster, especially for small barriers but one can already recognize that for $L_B = 90$ nm the mean FPT for diffusion and active transport are already the same in the range of error. If the effective viscosity is further increased inside the barrier ($\eta^* = 100\eta$), the active transport is significantly faster (4.15**(c)**) and the mean FPT does not show the quadratic behavior with the interval length $2 \cdot (x_B + L_B)$ anymore concluding that for large crowded compartments active motor pulling is crucial to obtain stable and efficient transport.

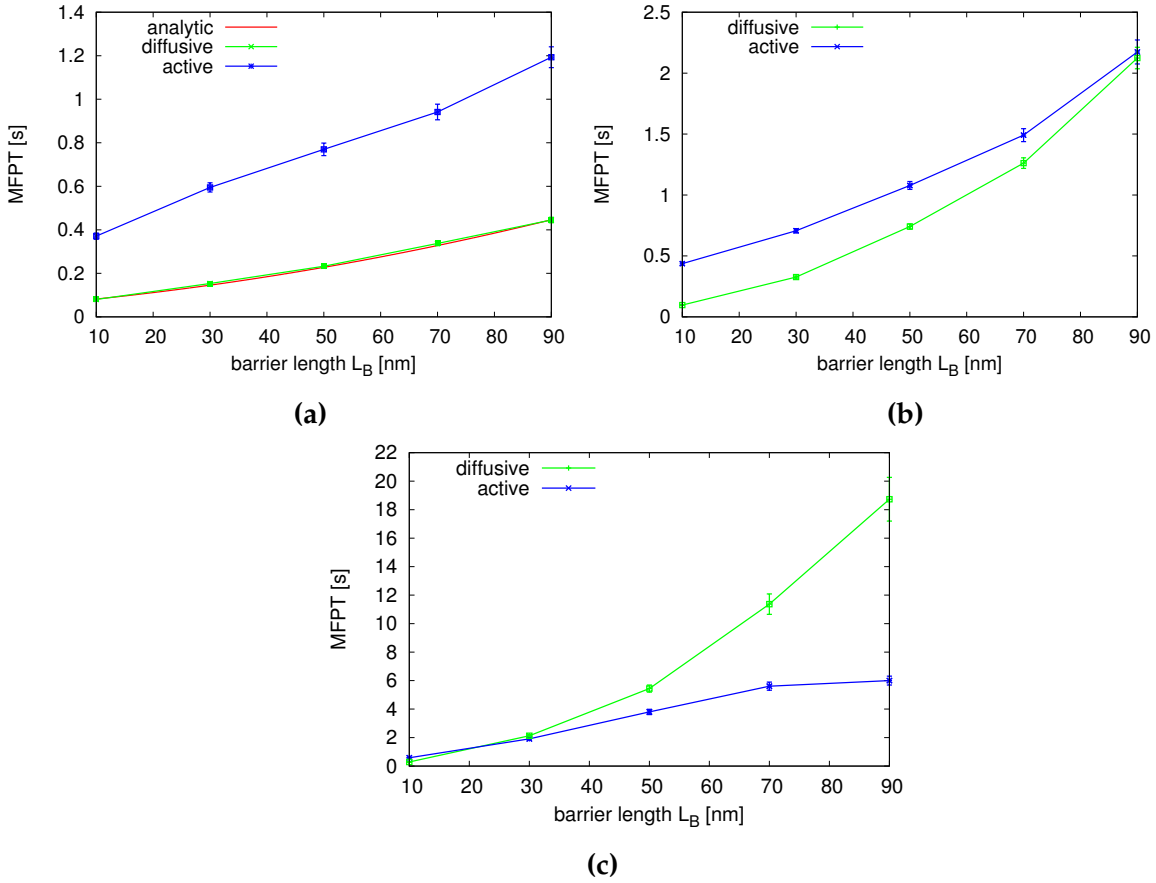


**Figure 4.15:** MFPT for different barrier viscosities (**(a)** $\eta^* = \eta$, **(b)** $\eta^* = 10\eta$, **(c)** $\eta^* = 100\eta$) and different barrier lengths $L_B$. We show the cases with active transport (blue) and pure diffusion (green). In some regimes it is more efficient to diffuse through the cell, especially for small distances and low viscosities. If the effective viscosity is considerably higher, it is more productive to actively transport the cargo. The red line in **(a)** shows the analytic solution for the mean FPT for diffusion on an interval. The errorbars give the Gaussian error.
Reprinted by permission from *Fluctuation effects in bidirectional cargo transport* EPJST, 223(14):3215–3225, 2014.

## 4.4 Chapter conclusion

In this chapter I discussed several models of bidirectional cargo transport. On the one hand I presented the MF-model and its results [86]. One the other hand I described the EPB-model which takes single motor positions into account and thus doesn't neglect force fluctuations exerted on the cargo. Three different variants of this EPB-model were studied. In the first part the stochastic fluctuations in a model with symmetric motor characteristics were analyzed. Here the same set of parameters as in the MF-model was used. Second, it was taken into account that the two motor families are actually quite different and do not always react in the same way to forces. The differences were modeled in detail and it was checked how the cellular environment changes the overall cargo motion. In a final step thermal fluctua-

tions were taken into account as well in order to study the effects on short- and long-time transport. Furthermore, the efficiency of bidirectional transport compared to pure diffusion was studied.

For the symmetric EPB-model the main result was that states with SBDs are mean-field artifacts. In the MF-model a realizations with only one team of (strong) motors is highly likely and very stable. In the EBP-model on the contrary this is only a rather rare event with short lifetime (cf. Fig 4.5) as long as the motor teams' characteristics were kept equal. Even with an *ad hoc* assumption of mutual motor activation which results in strong coupling between the motors of one team states with SBDs can only be realized with a biologically irrelevant high number of motors

Note, that this result is only valid as long as the motors walk in opposite direction. One could also assume two teams of motors walking in the same direction but with different velocities. In that case the forces are assisting for slow and hindering for fast motors. In [76] Li *et al.* showed that in this case SBDs occur. Defining the ratio between the detachment forces of slow and fast motors gives a range for which two solutions exist. In the whole range the detachment force of slow motors is bigger than the one of fast motors.

In the case that the features of kinesin and dynein were modeled more in detail it was found that trajectories of such motor-cargo complexes exhibit different dynamic regimes. In general, the cargo motion was biased and it was shown that only for a very small set of control parameters the activity of dynein and kinesin motors could be balanced. The mechanical coupling of the motors induced a cargo motion that is correlated in time - once the motor makes a step in a given direction the resulting forces on the motors within the same team decrease while the forces exerted on the other team increase. That is why the probability to continue moving in the same direction as before is higher than to turn. These correlations lead in the comoving frame to super-diffusive behavior at times from 10 ms to 1 s with the chosen set of parameters. Furthermore, it was shown that the exponent $\alpha$ which gives the algebraic time-dependence of the cargo's displacement variance is not universal as it was stated before [22] but depends on the motor parameters. Once thermal fluctuations were taken into account a subdiffusive behavior at shorter time scales as it was found experimentally [71] can be reproduced in the frame of the EPB-model. This subdiffussive motion occurs due to the superposition of the two potentials given by the linear springs of the motors and the thermal fluctuations.

Naively one would expect faster cargo transport for higher concentrations of ATP and lower viscosities. In this work it was shown that this is not the case in general. The response to both environmental parameters is non-monotonous and highly counter-intuitive. The ATP concentration rescales dynein's force scale such that for low concentrations the minus motors are stalled already at comparably low forces. At the same time kinesin's detachment force is still rather small such that the teams of plus motors can take over the cargo. With increasing ATP concentration dynein's stall force increases such that the minus-motors can

exert a higher total force on the cargo. Considering that kinesin's detachment rate grows exponentially in that force regime dynein can take over due to its catch-bond-like detachment behavior at forces above stall. The effect is similar for increasing viscosities representing effective forces exerted on the cargo. Nevertheless, we don't expect that the ATP concentration in the cell itself exhibits a spatially heterogeneous distribution but that rather the binding sites for ATP at the motors might be adjustable by the cell.

The recent progress in dynein motility assays [84] allows one to test the model predictions *in vitro*. Due to this achievement it should soon be possible to study bidirectionally transported motor-cargo complexes *in vitro* . With the help of such an experiment it could could be possible to validate this modeling approach described in this chapter. Additionally both, experiment and model, could then be modified to account for more complex situations as for instance the influence of well-defined filament network structures.

# Chapter 5

# Collective effects in multiple cargo transport

**Contents**



*This chapter combines the results from the EPB-model with the modeling experience of exclusion processes in order to develop a model analyzing the effects occurring due to multiple cargo moving along a filament. The characteristics found with the EPB-model for a single cargo are used to define particles with internal states. First the single particle dynamics are discussed and good agreement with the turning time distribution from the EPB-model is found. Then several of these particles are put on a one-dimensional lattice moving under an exclusion principle. For those, a density-dependent condensation occurs and is analyzed in a mean-field approach.*

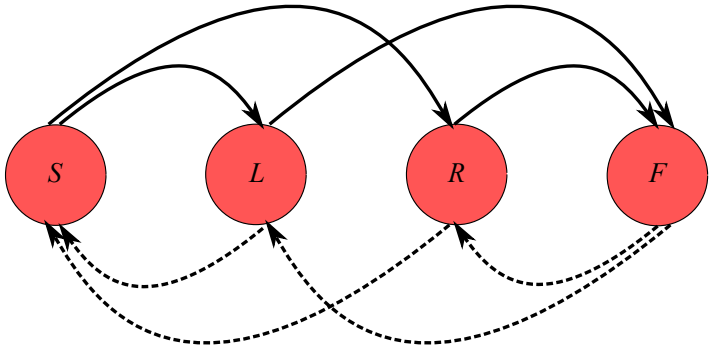


**Figure 5.1:** Depiction of the possible transitions between the different states which allow one to define the system as a ZRP. Transitions with a full line occur with rate $k_F$, those with a dashed line with rate $k_S$.

In chapter 3 lattice gas models were discussed, which are well suited in order to analyze the collective effects in many particle motion. In this chapter these results shall be used to study the collective effects of many cargos moving along a microtubule. If one would use the full EPB-model for several cargos, the set of parameter would be huge and also the numerical analysis would be very demanding. For that reason the cargos are represented by particles with internal states. In former works the idea of internal states was discussed in order to take the kinetic cycle of molecular motors [25] or possible inactive states [91] into account. In our approach the internal states, which determine the particle dynamics, are introduced in order to preserve the motion characteristics for a cargo moved by two teams of motors in the EPB-model as it is discussed in chapter 4.

In order to analyze the many-particle interaction on a filament, many of these particle are put on a lattice. Along the lattice position exclusion holds, such that only one particle can occupy a given site. With this definition the time-dependent hopping rates define a particle-wise disorder in the hopping. And further, even though the particle order along the lattice itself remains fixed with time, the order of states is not conserved.

## 5.1 Single particle dynamics

For the EPB-model with symmetric motors as described in section 4.2 it is found that the turning time distribution has two time scales, indicating the existence of short and long runs as it was also found experimentally [46]. In order to reproduce this effect with a single particle without taking the motor steps into account, internal states are introduced. The states are characterized by a pair of hopping rates, for left and right hopping, respectively. Additionally, the particles can at every time change their state, corresponding to the rules given in Fig. 5.1.

Each of the four states is characterized by a pair of rates $p_i$ and $q_j$, corresponding to the

left and right hopping rates, respectively. We define the pairs as

- S: $(p_1, q_1)$
- R: $(p_1, q_2)$
- L: $(p_2, q_1)$
- F: $(p_2, q_2)$.

In order to have an effectively unbiased particle it is convenient to use $p_1 = q_1$ and $p_2 = q_2$, such that state $S$ exhibits slow diffusive motion, $L$ a bias to the left, $R$ a bias to the right and $F$ a fast diffusion, assuming that $p_2 > p_1$. At first, we concentrate on the single particle dynamics and check whether the model defined above captures the cargo motion characteristics as found with the EPB-model. In Figure 5.3 the distribution of the turning time is given from the EPB-model and also from the particle model with internal states. We find a good agreement between the two models and the also occurrence of two time scales in the particle model. The turning time distribution for the particle model can be calculated analytically. For that purpose we use a continuous time Markov chain (CTMC), which is characterized by a discrete state space but propagating in continuous time. The transition times are exponentially distributed. In order to determine the distribution of turning times, we introduce the Markov chain with an absorbing state $(*)$. Without loss of generality, we assume that the first step is to the left such that we are interested in the time passing until the first step to the right occurs. The transitions in the Markov chain are defined as shown in Figure 5.2 or in a matrix representation with matrix $\mathbf{Q}$, given by

$$\mathbf{Q} = \begin{bmatrix} A_1 & p_1 & k_S & 0 & k_S & 0 & 0 & 0 & 0 \\ p1 & A_1 & k_S & 0 & k_S & 0 & 0 & 0 & 0 \\ k_F & 0 & A_2 & p_1 & 0 & 0 & k_S & 0 & 0 \\ k_F & 0 & p_1 & A_2 & 0 & 0 & k_S & 0 & 0 \\ k_F & 0 & 0 & 0 & A_3 & p_2 & k_S & 0 & 0 \\ k_F & 0 & 0 & 0 & p_2 & A_3 & k_S & 0 & 0 \\ 0 & 0 & k_F & 0 & k_F & 0 & A_4 & p_2 & 0 \\ 0 & 0 & k_F & 0 & k_F & 0 & p_2 & A_4 & 0 \\ 0 & 0 & 0 & 0 & 0 & 0 & 0 & 0 & 0 \end{bmatrix} \tag{5.1}$$

with $A_1 = -2k_S - p_1 - q_1$, $A_2 = -k_S - k_F - p_1 - q_2$, $A_3 = -k_S - k_F - q_1 - p_2$ and $A_4 = -2k_F - p_2 - q_2$.

In order to calculate the turning time we introduce additionally to the states $S$, $L$, $R$ and $F$ the auxiliary states $S^*$, $L^*$, $R^*$ and $F^*$. They are necessary in the calculation in order to take into account that the particle not only changes its internal state but might also make an arbitrary number of steps in the same direction *before* it steps in opposite direction. The

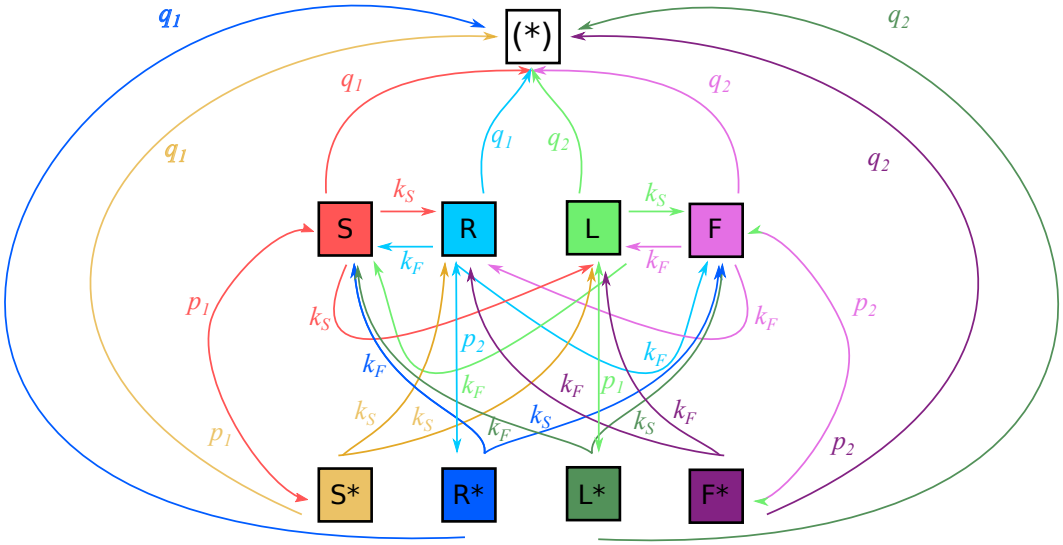


**Figure 5.2:** Sketch of the transitions to determine the turning time distribution. The arrows leaving one state are drawn in the same color than the leaving states.

transitions to these states happen with rate $p_i$ with $i$ =1,2, depending on the particular state. These eight states are transient.

The life time before absorbing in a CTMC has a phase-type distribution [19], as the transient states are often called phases. It is possible to decompose the transition matrix, or also called infinitesimal generator, $\mathbf{Q}$ in one matrix $\mathbf{D}$, containing the transitions between the transient states, and two vectors. The column vector is given by $\mathbf{0} = (0, 0, 0, 0, ..., 0)$, since no mass can leave the absorbing state and the row vector $\mathbf{d_0}$ gives the rates for the transitions from the transient states to the absorbing one. Further, we assume that the initial distribution is given by $\boldsymbol{\pi_0}$. Then the life time distribution, corresponding to the turning time distribution $\mathcal{T}(t)$ in our case, is given by

$$\mathcal{T}(t) = \boldsymbol{\pi}_0 \mathrm{e}^{\mathbf{D}t}\mathbf{d_0} \quad \text{for } t > 0. \tag{5.2}$$

This CTMC gives a good approximation for the turning time distribution for one particle. It is not exact, as we assume that the initial distribution is given by $\pi_i = 1/8$ for $i = 1, .., 8$, corresponding to the transient states and $\pi_9 = 0$, such that no mass is absorbed in the initial state. The distributions obtained by the EPB-model, the particle model with internal states and by the CTMC are shown in Figure 5.3.

In order to analyze a possible condensation or clustering, it makes sense to use the distance from particle $i$ to particle $i+1$ as a variable instead of the lattice site of a single particle. In the following we shall refer to the particles hopping under exclusion as the *position picture* and to the model defined by the distance between the particles as the *distance picture*. If one maps the system in the position picture naively onto a distance picture, the hopping rates of a particle in the distance picture depend not only on the state of the particle itself but also

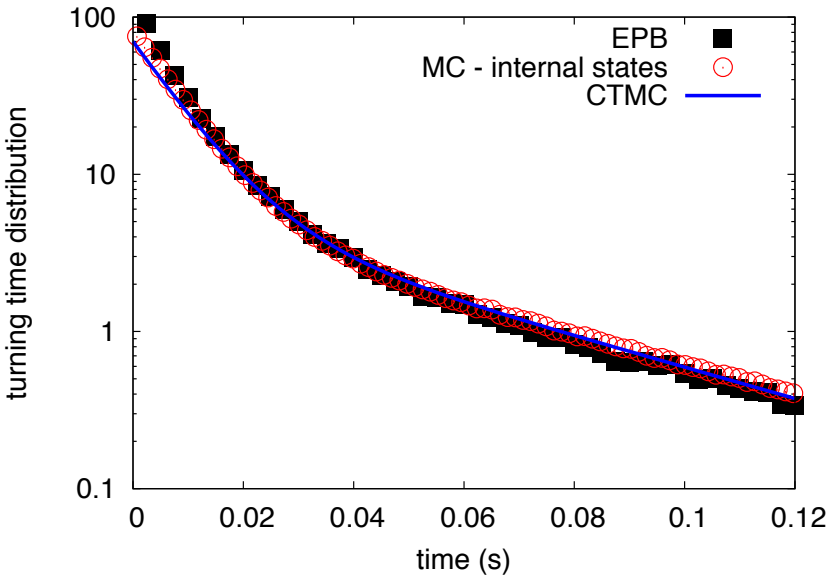


**Figure 5.3:** Normalized histogram of turning times. The black squares show the data obtained with the EPB-model, the red circles show the results obtained with the particle model with internal states and the straight line is the analytic result from the CTMC. The parameters used are $p_1 = q_1 = 20$, $p_2 = q_2 = 120$, $k_S = 1.5$ and $k_F = 1.7$.

on the neighboring sites. The scenario is depicted in Figure 5.4 where a particle at site $i$ in the position picture hops with rate $\tilde{p}_i$ to the right and the particle at position $i+1$ moves with rate $\tilde{q}_{i+1}$ to the left. This corresponds to particles in the distance picture moving to the right with a rate $\tilde{q}_{i+1}$ and to the left with rate $\tilde{p}_i$. In order to map the system correctly onto a distance picture the transition between the states have to be chosen in way that the hopping rates are independent. This is granted as long as only one of the two hopping rates changes between two states. The transitions between the internal states, as they are defined in Figure 5.1, fulfill this criteria. Hence, it is possible to define the hopping rates $q_{i+1} = q_i$ and $p_i = \tilde{p}_i$ for the particles in the distance picture. Note that in the distance picture more than one particle can occupy a single site.

## 5.2 Lattice gas model with internal states

Knowing that the particles with internal states give a good approximation of the characteristic motion of a cargo in the EPB-model, collective effects along a lattice can be studied. For that reason $N$ of these particles are put on a periodic lattice of size $L$. In the distance picture at each lattice site $i = 0, .., N$ a number of $n = 0, ..., L - N$ particles can be present. The only restriction is given by the conservation of particles, such that the sum over all particles in

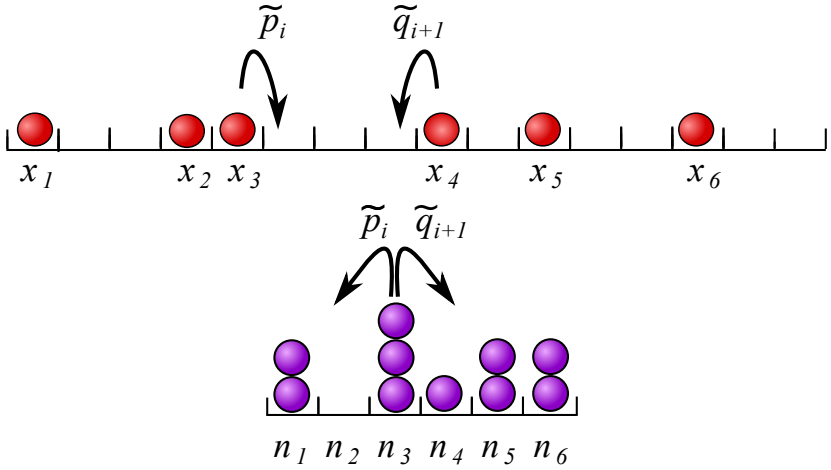


**Figure 5.4:** Mapping of the particle model with internal states from a position picture onto a distance picture. One recognizes easily that the hopping rates for a particle in the distance picture depend on the rates of two particles in the position picture.

the distance picture has to be equal to $M = L - N$. We define the probability for having $n$ particles at a site as $S_n$, $R_n$, $L_n$ and $F_n$, depending on their state. In a mean-field description, the time evolution of the densities to find $n$ of particles in state $i$ at a site is given by the following set of equations

$$\begin{aligned}
\frac{\mathrm{d}}{\mathrm{d}t}S_n =& -2k_F S_n + k_S(L_n + R_n) && \text{(5.3a)}\\
& -(q_1 + p_1 + w + v)S_n + (q_1 + p_1)S_{n+1} + (w + v)S_{n-1}\\
\frac{\mathrm{d}}{\mathrm{d}t}L_n =& -(k_S + k_F)L_n + k_S F_n + k_F S_n && \text{(5.3b)}\\
& -(q_2 + p_1 + w + v)L_n + (q_2 + p_1)L_{n+1} + (w + v)L_{n-1}\\
\frac{\mathrm{d}}{\mathrm{d}t}R_n =& -(k_S + k_F)R_n + k_F S_n + k_S F_n && \text{(5.3c)}\\
& -(q_1 + p_2 + w + v)R_n + (q_1 + p_2)R_{n+1} + (w + v)R_{n-1}\\
\frac{\mathrm{d}}{\mathrm{d}t}F_n =& -2k_S F_n + k_F(R_n + L_n) && \text{(5.3d)}\\
& -(q_2 + p_2 + w + v)F_n + (q_2 + p_2)F_{n+1} + (w + v)F_{n-1}.
\end{aligned}$$

The variables $w$ and $v$ are the effective rates for particles hopping away from a lattice site in the distance picture. This is only then possible if at least one particle is present at the neighboring sites. Therefore, we define

$$w := q_1 \sum_{m>0}(S_m + L_m) + q_2 \sum_{m>0}(R_m + F_m) \quad \text{(5.4a)}$$

$$v := p_1 \sum_{m>0}(S_m + R_m) + p_2 \sum_{m>0}(L_m + F_m). \quad \text{(5.4b)}$$

Additionally, for the boundaries one finds

$$\frac{\mathrm{d}}{\mathrm{d}t}S_0 = -2k_F S_0 + k_S(L_0 + R_0) - (w+v)S_0 + (q_1 + p_1)S_1 \tag{5.5a}$$
$$\frac{\mathrm{d}}{\mathrm{d}t}L_0 = -(k_S + k_F)L_0 + k_S F_0 + k_F S_0 - (w+v)L_0 + (q_2 + p_1)L_1 \tag{5.5b}$$
$$\frac{\mathrm{d}}{\mathrm{d}t}R_0 = -(k_S + k_F)R_0 + k_S F_0 + k_F S_0 - (w+v)R_0 + (q_1 + p_2)R_1 \tag{5.5c}$$
$$\frac{\mathrm{d}}{\mathrm{d}t}F_0 = -2k_S S_0 + k_F(L_0 + R_0) - (w+v)F_0 + (q_2 + p_2)F_1 \tag{5.5d}$$
$$\tag{5.5e}$$

for $n = 0$ and

$$\frac{\mathrm{d}}{\mathrm{d}t}S_M = -2k_F S_M + k_S(L_M + R_M) - (p1 + q1)S_M + (w+v)S_{M-1} \tag{5.6a}$$
$$\frac{\mathrm{d}}{\mathrm{d}t}L_M = -(k_S + k_F)L_M + k_S F_M + k_F S_M - (p1 + q2)L_M + (w+v)L_{M-1} \tag{5.6b}$$
$$\frac{\mathrm{d}}{\mathrm{d}t}R_M = -(k_S + k_F)R_M + k_S F_M + k_F S_M - (p2 + q1)R_M + (w+v)R_{M-1} \tag{5.6c}$$
$$\frac{\mathrm{d}}{\mathrm{d}t}F_M = -2k_S S_M + k_F(L_M + R_M) - (p2 + q1)F_M + (w+v)F_{M-1} \tag{5.6d}$$
$$\tag{5.6e}$$

for $n = M$. In order to solve this set of equations, it is convenient to introduce the generating functions of the probability densities, defined by

$$\tilde{S}(z) = \sum_{n=0}^{\infty} S_n z^{n+1} \tag{5.7a}$$
$$\tilde{L}(z) = \sum_{n=0}^{\infty} L_n z^{n+1} \tag{5.7b}$$
$$\tilde{R}(z) = \sum_{n=0}^{\infty} R_n z^{n+1} \tag{5.7c}$$
$$\tilde{F}(z) = \sum_{n=0}^{\infty} F_n z^{n+1}. \tag{5.7d}$$

Summing over all $n$ and multiplying with $z^{n+1}$ and assuming that the system is in its steady state gives

$$\tilde{S}(z) = \left[\left(\frac{p_1 + q_1}{z} - (w+v)\right)(1-z) + 2k_F\right]^{-1} \left(k_S(\tilde{L}(z) + \tilde{R}(z)) - S_0(1-z)(p_1 + q_1)\right) \tag{5.8a}$$

$$\tilde{L}(z) = \left[\left(\frac{p_1+q_2}{z} - (w+v)\right)(1-z) + k_S + k_F\right]^{-1} (k_S\tilde{F}(z) + k_F\tilde{S}(z) - L_0(1-z)(p_1+q_2)) \tag{5.8b}$$

$$\tilde{R}(z) = \left[\left(\frac{p_2+q_1}{z} - (w+v)\right)(1-z) + k_S + k_F\right]^{-1} (k_S\tilde{F}(z) + k_F\tilde{S}(z) - R_0(1-z)(p_2+q_1)) \tag{5.8c}$$

$$\tilde{F}(z) = \left[\left(\frac{p_2+q_2}{z} - (w+v)\right)(1-z) + 2k_S\right]^{-1} (k_F(\tilde{L}(z) + \tilde{R}(z)) - F_0(1-z)(p_2+q_2)). \tag{5.8d}$$

In order to solve this set of equations constraints have to be found on the densities. For physical reasons, the following equations have to be fulfilled for $\tilde{S}(z)$, $\tilde{R}(z)$, $\tilde{L}(z)$ and $\tilde{F}(z)$:

$$\tilde{S}(1) + \tilde{R}(1) + \tilde{L}(1) + \tilde{F}(1) = 1 \text{ conservation of probability} \tag{5.9a}$$

$$\tilde{S}'(1) + \tilde{R}'(1) + \tilde{L}'(1) + \tilde{F}'(1) = L/N \text{ conservation of mass} \tag{5.9b}$$

$$L_0 = R_0 \text{ no flux} \tag{5.9c}$$

where prime indicates the derivative with respect to $z$. Furthermore, one knows due to the choice of transitions with the two rates $k_S$ and $k_F$ the weight of the single states in the steady state such that

$$\tilde{L}(1) = \tilde{R}(1) = \frac{k_F k_S}{(k_F+k_S)^2} \tag{5.10a}$$

$$\tilde{S}(1) = \frac{k_S^2}{(k_F+k_S)^2} \tag{5.10b}$$

$$\tilde{F}(1) = \frac{k_F^2}{(k_F+k_S)^2}. \tag{5.10c}$$

Solving the set of linear equations (5.8) gives expressions for $\tilde{S}(z)$, $\tilde{R}(z)$, $\tilde{L}(z)$ and $\tilde{F}(z)$ depending on the unknown probabilities $S_0$, $L_0$, $R_0$ and $F_0$ to find zero particles at a site. From the zero-flux condition 5.9c we already know that $L_0 = R_0$, such that three unknowns are left. Equation 5.9a does not give any further constraints since the probability is conserved by construction and so does not reduce the number of unknowns. However, from equation 5.9b we get the following condition from the conservation of mass

$$\begin{aligned}
&\frac{L}{N}\Big[p_1(L_0+S_0) + p_2(F_0+L_0)\Big](k_F+k_S)^3 = \\
&k_F^3 p_2 + \Big((p_1+2p_2)k_S - (p_1-p_2)(p_1(L_0+2S_0) + p_2L_0)\Big)k_F^2 \\
&+ \Big((p_2+2p_1)k_S + (p_1-p_2)(p_1(1-2S_0) + p_2(2F_0-1))\Big)k_S k_F \\
&+ \Big(p_1k_S + (p_1-p_2)(p_1L_0 + p_2(2F_0+L_0))\Big)k_S^2.
\end{aligned} \tag{5.11}$$

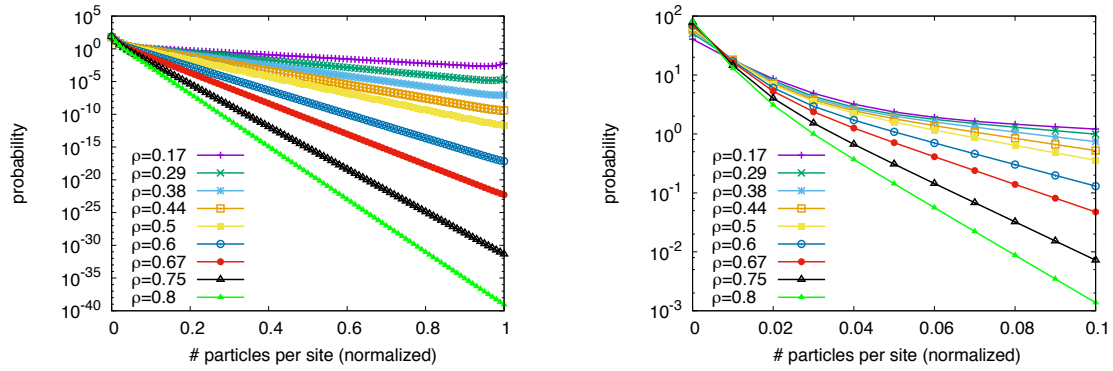


**Figure 5.5:** The probability densities $S_n,\ R_n,\ L_n,\ F_n$ from numerical integration of the set of master equations given by (5.3), (5.5), (5.6). The maximal number of particles $M = L - N$ is normalized to 1. **(a)** shows the full distribution while **(b)** gives a zoom for small $n$. The asymptotics are exponentially decreasing as expected for a ZRP but due to the internal states we find a boundary layer for small $n$. Parameters: $k_F = 1.7$, $k_S = 1.5$, $p_1 = 20$, $p_2 = 120$.

But still, two more conditions are necessary in order to obtain the probability densities analytically.

### 5.2.1 Condensation effects

Nevertheless, one can integrate the set of master equations (5.3), (5.5), (5.6) numerically. In Figure 5.5 the probability $\mathcal{P}_n$ to find $n$ particles in a box in the ZRP is shown, irrespective of the state i.e. $\mathcal{P}_n = S_n + R_n + L_n + F_n$ . Note, that the number of particles is normalized such that the maximal number $M = L - N$ is set to one.

From Figure 5.5 **(a)** it is easy to see that the asymptotic decrease of the probability densities is exponential, as it is known for a zero-range process. However, for small $n$ the densities deviate significantly from a purely exponential form. Furthermore, for increasing density $\rho$ the behavior converges towards the purely exponential case, as it is for example found for the SSEP. The internal states induce correlations between the particles and therefore, the model does not represent a zero-range process. These correlations lead to a cluster formation which especially for the low density case have a strong effect. We checked carefully that this deviation from an exponential decay is not a finite size effect. In the following we shall analyze the clustering and its consequences in more detail.

The increased probability to have $n = 0$ particles at a site is also reflected in the particle speed $u$, which is defined as

$$u = p_1\Big(\tilde{S}(1) - S_0 + \tilde{L}(1) - L_0\Big) + p_2\Big(\tilde{F}(1) - F_0 + \tilde{R}(1) - R_0\Big) \tag{5.12}$$

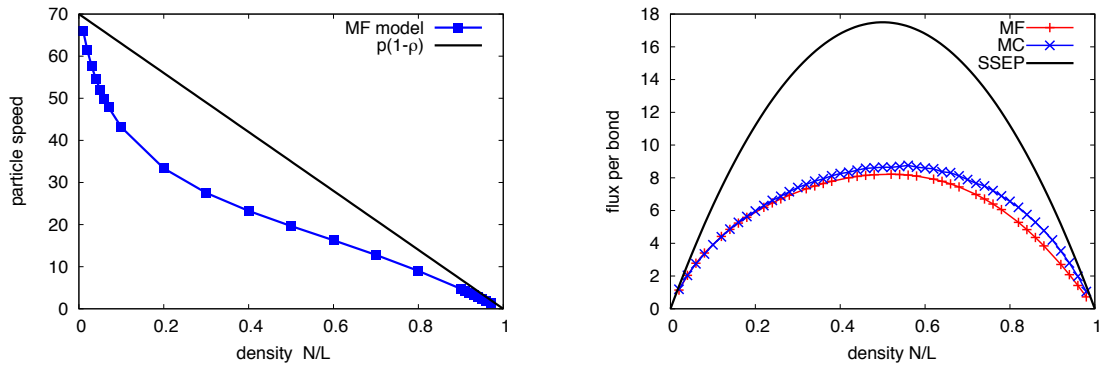


**(a)** **(b)**

**Figure 5.6:** The particle **(a)** speed and **(b)** flux against the density for the ZRP with internal states and the SSEP is shown. In the fundamental diagram **(b)** the red curve shows the flux obtained by integration the MF equations, the blue curve gives the flux as it is found by Monte Carlo simulations of the lattice model. For the speed one observes a strong deviation from the SSEP for low densities. The particle flux in the ZRP is significantly smaller than for the SSEP. Note that we show the flux in one direction only as the overall flux is zero due to the symmetrically chosen rates. Parameters: $k_F = 1.7$, $k_S = 1.5$, $p_1 = 20$, $p_2 = 120$.

in the MF model.

In the SSEP the particle speed is given by $\tilde{p}(1-\rho)$ as discussed in chapter 3. Defining the hopping rate $\tilde{p}$ in the SSEP as $\tilde{p} = (p_1 + p_2)/2$ we can directly compare the particle speed in the two models. The result is shown in Figure 5.6 **(a)**, where one observes in the ZRP with internal states for low densities a strong deviation from the SSEP. For increasing density the particle speed converges towards the exact result for the SSEP. The reduced speed, resulting from the increased probability for $n = 0$, shows that the internal states alter the system's dynamics significantly and that clustering occurs. A similar effect is naturally observed for the fundamental diagram. One observes in Figure 5.6 **(b)** that the particle flux (in either the plus or minus direction) for the ZRP with internal states is significantly smaller than for the SSEP, in which it is given by $\tilde{p}\rho(1-\rho)$. But not only that the flux is smaller, further the shape of the fundamental diagram is changed. Instead of the parabolic curve given in the SSEP, in the ZRP with internal states the curve is tilted towards higher densities, so that the maximal speed is found for densities bigger than one half. For low particle densities, the flux found by integrating the MF equations is in good agreement with the one found by Monte Carlo simulations of the particle model. However, for higher densities the mean-field flux is smaller than the one found in the lattice model.

In order to gain a better understanding of the particle clustering, the mean distance $\langle d \rangle$ between particles on the lattice is measured. On the one hand it can be determined directly from the distribution. On the other hand one can fit an exponentially decreasing function ($\sim \exp(-n/\langle d_h \rangle)$) to the tails of the distribution. The two quantities are shown in Figure

5.7 and one observes that the exponential fit to the tails overestimates the distance between particles. The tail gives the homogeneous density region along the lattice and so does not take the clustering into account. In the inset of Figure 5.7 the deviation for small distances, which characterizes the clustering, is shown. This deviations explains the different mean distances for these two ways of measurement. Due to the clustering the particle density is (in the position picture) much smaller in regions outside the cluster. Therefore, the effective density the particles feel in these regions is low and with this, the mean distance between particles big. In order to take the clustering into account a double exponential fit

$$\left(1 - \frac{r_2}{d_2}\right) d_1 \exp\left(-n d_1\right) + \frac{r_2}{d_2} \exp\left(-n d_2\right). \tag{5.13}$$

Using this double exponential approach the mixed mean distance is given by

$$\langle d_m \rangle = \left(1 - \frac{r_2}{d_2}\right) d_1^{-1} + \frac{r_2}{d_2^2}. \tag{5.14}$$

This mixed mean distance gives a good agreement with the mean distance obtained from the full distribution as shown in Figure 5.7. Note, that for high particle densities ($\rho > 0.7$) the deviation from the purely exponential form is so small (compare Figure 5.5) that a double exponential fit does not give good results anymore.

In order to analyze the deviations between the particle flux in the mean-field model and the explicit particle model, the two-point correlations in the latter are calculated and shown in Figure 5.8. The largest correlations occur for low densities. This agrees well with the higher probabilities for small $n$ (in the distance picture) at low densities. However, at the same time the particle flux measured in the mean-field model agrees almost perfectly with the flux obtained by the Monte Carlo simulations of the particle model. This indicates that at high densities the correlations are more efficient and avoid the particles from hopping but rather traps them in or between macroscopic clusters.

## 5.3 Chapter conclusion

By introducing internal states of motion for a single particle it is possible reproduce the turning time distribution of a cargo moving in the frame of the EPB-model. A good agreement is obtained if two states show a bias either to the left or to the right and the two other states move diffusively with two different diffusion constants. In contrast to the EPB-model the turning time distribution can be calculated analytically for this type of particle by means of the infinitesimal generator.

Several of these particles are then put on a periodic lattice in order to study the collective effects occurring due to spatial exclusion along the lattice. The transition rates between the states are defined in a way that the overall motion is symmetric, hence the reference sys-

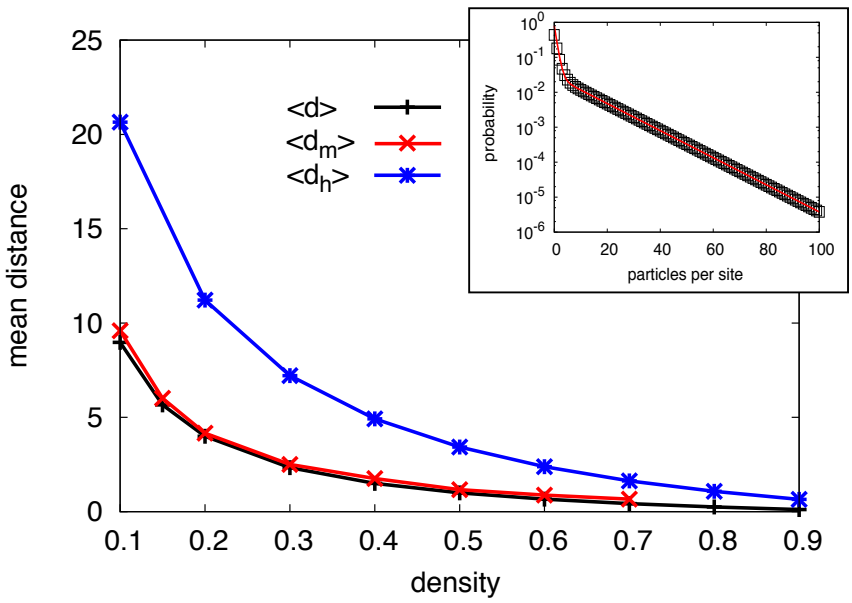


**Figure 5.7:** The mean particle distance $\langle d \rangle$ obtained from the full distance distribution in the MF model (black), from a fit to the exponential tail of the distribution $\langle d_h \rangle$ (blue) representing the homogeneous region and a double exponential fit $\langle d_m \rangle$ (red) which takes also additionally the clustered region into account. Obviously, $\langle d_h \rangle$ overestimates the mean distance between particles, whereas taking the clustered region additionally into account gives a good agreement. Inset: probability distribution the distance between particles obtained in the MF model (black) and the fit to a double exponential distiribution (red).

tem is the symmetric simple exclusion process. In the SSEP all particle configurations are equally probable. As the SSEP can be mapped onto a zero-range process, its steady state distribution of distances between particles obeys an exponential distribution. We showed in this section that with the consideration of different internal states a macroscopic clustering occurs. Therefore, the distribution of distances between particles shows an increased probability for small distances and hence the distribution deviates from a purely exponential form. Due to the clustering the particle speed and flux are smaller than in the SSEP. Furthermore, the fundamental diagram is no longer symmetric around particle density one half but is tilted with a maximum at higher densities. In order to further analyze this effect the two-point correlation function is determined. Even though the correlations are higher for lower forces, they are more efficient for higher densities. In the latter case the system has a tendency to form cluster simply due to the big number of particles. With this small perturbations due to the internal state the effect is enhanced. Furthermore, the high influence of the clustered region becomes obvious by determining the mean distance between particles (or the mean number of particles per box in the distance picture). Though the distribution for this observable shows an exponential tail, the state $n = 0$, corresponding to zero dis-

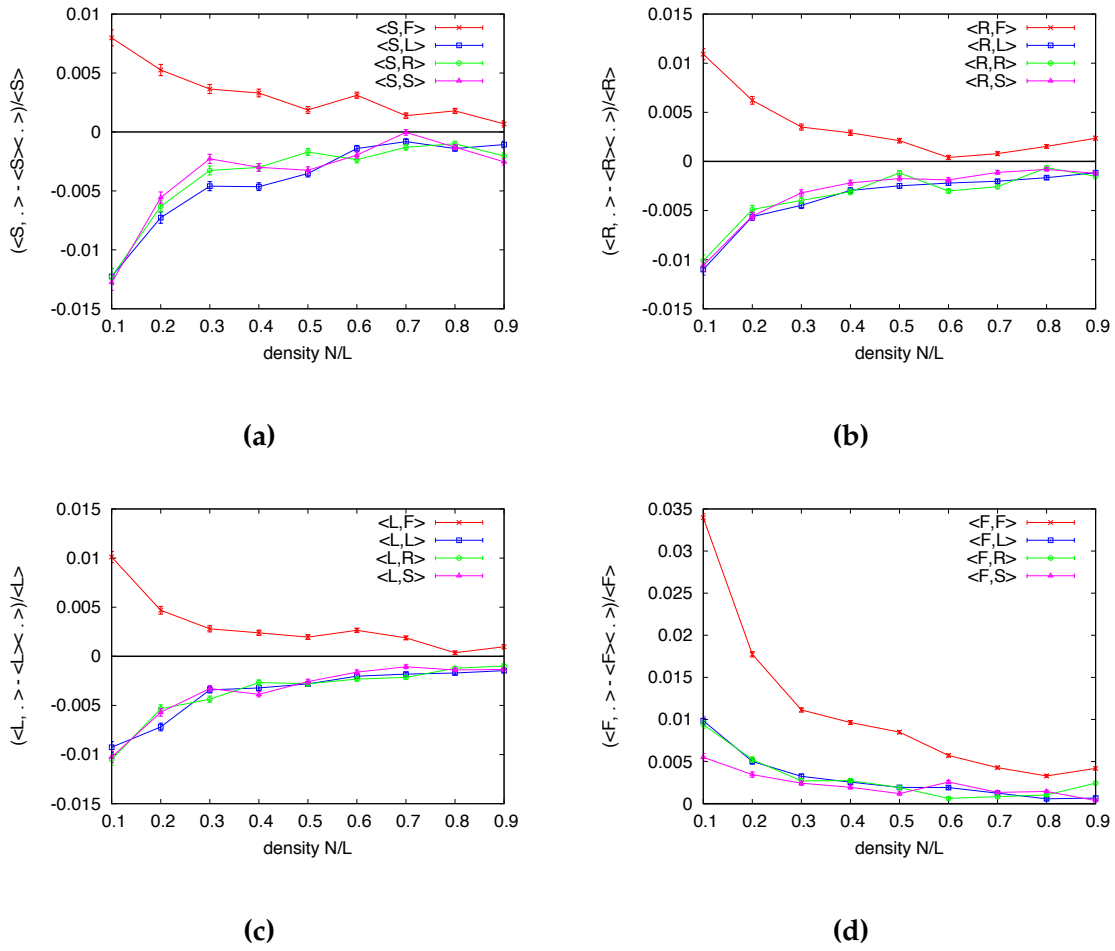


**Figure 5.8:** Two-point correlations in the ZRP with internal states obtained by Monte Carlo simulations of the explicit lattice model. The correlations decrease with increasing densities. Parameters: $k_F = 1.7$, $k_S = 1.5$, $p_1 = 20$, $p_2 = 120$.

tance to the next particle, has a rather high weight. Therefore, the mean distance obtained by fitting the exponential tail is overestimated.

We showed that the collective motion of particles obeying the same motion characteristics as a cargo in the EPB-model results in a cluster formation. This effect indicates that for an efficient flux along a filament more ingredients are necessary, as for example a direct particle exchange or a dynamic lattice [33].

# Chapter 6

# Spontaneous pulsing states in an active particle system

**Contents**

*We study a minimal model inspired by the work of Lin et al. [79] which shows a pulsing behavior in a tubular geometry. The pulsing phase is characterized by a periodic change in the particle density. We first clarify which ingredients are necessary in order to obtain a pulsing behavior in an explicit model. The actual model under study is then a mean-field approximation of this particle model. For this model we can predict the density profile in the low density phase with a very good agreement with numerical solutions. For the pulsing phase we study the filling and emptying stage separately. In the filling stage we can find a good approximation for the filling velocity. In the emptying stage we find both numerically and analytically an easy relation between positive and negative fluxes. We can predict the emptying velocity as a function of the deviation from 1/2 on the bulk densities considering mass conservation. Then we will perform a stability analysis in order to understand spatial and temporal density oscillations in the bulk. Furthermore, we will introduce a model continuous in space and an effective Markov chain to obtain the emptying velocity.*

## 6.1 Chapter introduction

In chapter 3 several models of (driven) lattice gases were introduced. This class of models was rapidly growing in the last decades and many effects are understood nowadays. In particular for the case of one-lane models with one species various analytic results were discovered for different boundary conditions and update rules.

However, also multiple lane-systems and/or models with more than one species were studied in detail in the past. In the following, I will discuss a driven lattice gas with one open and one reflecting boundary. On this lattice with an exclusion principle two species can move in opposite direction, either to the left or to the right. The model is inspired by a one from Lin *et al.* [79], which was used to describe bidirectional transportation along microtubules in fungal hyphae cells. They found in their model with 13 lanes and two species a phase with a pulsing behavior of the system.

In the following I will discuss what are the minimal requirements to obtain pulsing states in a two-species driven lattice gas model with one open and one reflecting boundary. We found that at least two lanes are necessary and that there must be an asymmetry between the two species besides the direction of motion. By means of a mean field approximation several characteristics of the model can be obtained analytically in this pulsing phase. But also some intriguing behavior occurs, as the front for instance rather hops along the lattice than moves continuously. Furthermore, we find some oscillations in the densities in time as well as in space. By a series expansion of the master equations for the densities in continuous space the system is not purely hyperbolic - they define a system of mixed type. Furthermore, we introduce an effective Markov chain as an attempt to predict the emptying velocity.

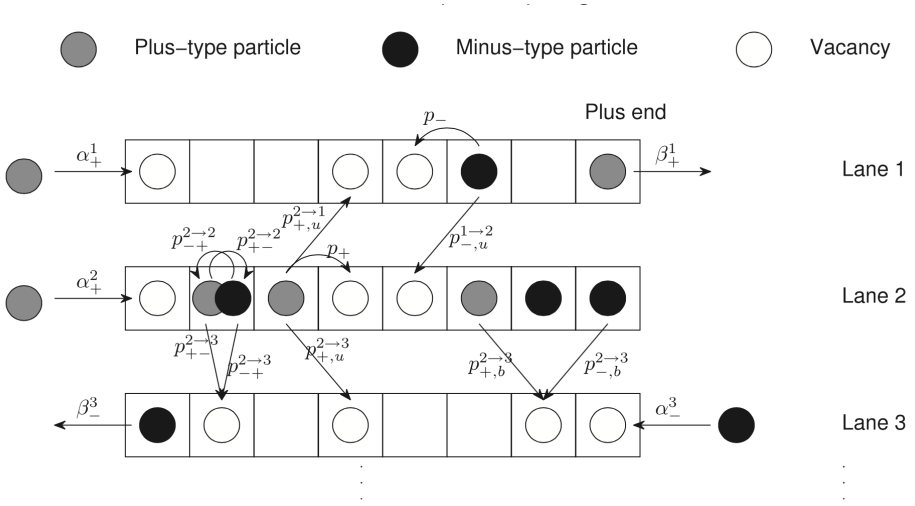


**Figure 6.1:** Sketch showing transition rates for the multi-lane bidirectional ASEP model by Lin *et al.* [79]; we consider $M$ lanes on the surface of a cylinder. The plus end (resp. minus end) of the cylinder is at the right (resp. left). Plus- type (resp. minus-type) particles move a step forward with rate $p_+$ (resp. $p_-$) while they move forward in association with a change of lane with rates $p^{l\to l\pm1}_{+,b(u)}$ ($p^{l\to l\pm1}_{-,b(u)}$) when blocked (resp. unblocked). Plus-type (resp. minus-type) particles are injected into the left (resp. right) boundary of the system at rate $\alpha^l_+$ (resp. $\alpha^l_-$) and exit at rate $\beta^l_+$ (resp. $\beta^l_-$ ) in the $l$th lane. Particles can also change from plus type to minus type (resp. from minus type to plus type) with rate $p^{l\to k}_{+-}$ (resp. $p^{l\to k}_{-+}$) in association with a possible change of lane $l$ to $k$ (if $l \neq k$); we assume that the site is preserved during a change of type.
Reprinted by permission under CC BY license from C. Lin *et al.* .,*Journal of Statistical Mechanics: Theory and Experiment*, 2011(09):P09027, 2011.

## 6.2 Multi-lane two-species model

In the work of Lin *et al.* [79] several components of the different models discussed in chapter 3 are combined. Their aim is to model bidirectional transport along microtubules in fungal hyphae cells. For that purpose they define a lattice of the size $L$x$M$ with open boundaries along $L$ and periodic ones along $M$.

Plus (minus) particles are injected at the left (right) boundary of lane $l$ with rate $\alpha^l_{+(-)}$ and have an exclusive position along the filament. Both types of particles hop along the filament with rate $p^{l\to l\pm1}_{\pm,b(u)}$. Here, the authors distinguish between particles which are unblocked (u) or blocked (b) by another particle at the adjacent site. This alters the hopping rates. A particle hops forward within the lane despite being blocked, then it changes lanes. Furthermore, particles can convert their type and therewith their hopping direction: plus particles become minus particles with rate $p^{l\to k}_{+-}$ and vise versa with rate $p^{l\to k}_{-+}$. Type conversion can be combined with a lane change at the same time. Once particles reach the opposite boundary, they leave the system with rate $\beta^l_\pm$. The dynamics are depicted in Figure 6.1.

Even though they define the model in a very general way the model studied in the pub-

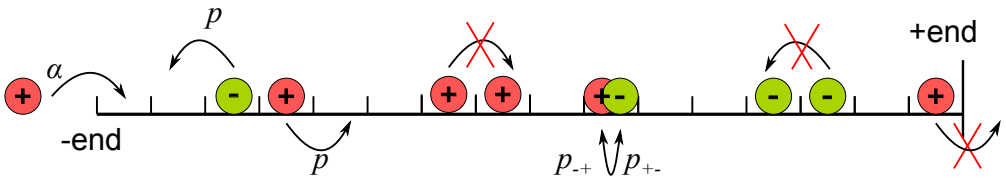


**Figure 6.2:** Sketch of the possible transitions. Red (plus) particles can hop with rate $p$ from the left to the right. Green (minus) particles hop with rate $p$ from the right to the left. Furthermore, the particles can change their type with rate $r$ from plus to minus and vice versa. Note, that particles cannot exchange along the lattice.

lication is a special case in which they assume the following as boundary conditions:

$$\alpha_+^l = \alpha_+/M \qquad \alpha_-^l = 0 \qquad \beta_+^l = 0 \qquad \beta_-^l = p_+. \tag{6.1}$$

This corresponds to no influx of minus particles and a reflecting boundary at the right.

Via Monte Carlo simulations they find for a quite big range of parameters so-called *pulsing states*. Those states are characterized by a particle density changing periodically in time. This means that the system's total flux changes its sign periodically i.e. the system fills up with particles until each lane reaches an overall particle density of almost $L \cdot M$. Due to the ability to change the hopping direction the particles can leave the system again at the left boundary. In this stage the outflow of particles dominates the dynamics and density decreases again which results in a negative flux.

## 6.3 One-lane model

For completeness, we study an one-lane system inspired on the model introduced by Lin *et al.* [79]. Here, we are mainly interested which are the necessary but minimal conditions to obtain a pulsing behavior. For that reason, we introduce a single-lane system of length $L$ with one open and one reflecting boundary as depicted in Figure 6.2. Plus particles enter the system at the left boundary with rate $\alpha$ and then hop with a rate $p$ to the right. The particles also change their type with a rate $r$ as in the model of Lin *et al.* [79] and thus invert their hopping direction. Once a plus particle becomes a minus particle it hops with the same rate $p$ as the plus particles to the left. At the time a minus particle reaches the left boundary it leaves the system with rate $p$. Just as plus particles they convert from minus to plus type with rate $r$. For both types the right boundary is a reflecting one. We assume that $p$ is of order $L$ to ensure that the particles invade the whole system.

A plausible idea is to first try to describe the system with a mean field ansatz with the particle densities $\rho_i$ for plus particles density and $\sigma_i$ for minus-particle density at site $i$. For the bulk dynamics one finds

$$\frac{\mathrm{d}\rho_i}{\mathrm{d}t} = -p\rho_i(1-\rho_{i+1}-\sigma_{i+1}) + p\rho_{i-1}(1-\rho_i-\sigma_i) - r(\rho_i+\sigma_i) \tag{6.2a}$$
$$\frac{\mathrm{d}\sigma_i}{\mathrm{d}t} = -p\sigma_i(1-\rho_{i-1}-\sigma_{i-1}) + p\sigma_{i+1}(1-\rho_i-\sigma_i) + r(\rho_i - r\sigma_i). \tag{6.2b}$$

In order to fulfill the boundary conditions the master equations for the open left boundary read

$$\frac{\mathrm{d}\rho_1}{\mathrm{d}t} = \alpha(1-\rho_1-\sigma_1) - p\rho_1(1-\rho_2-\sigma_2) - r(\rho_1-\sigma_1) \tag{6.3a}$$
$$\frac{\mathrm{d}\sigma_1}{\mathrm{d}t} = -p\sigma_1 + p\sigma_2(1-\rho_1-\sigma_1) + r(\rho_1-\sigma_1) \tag{6.3b}$$

and for the closed right one

$$\frac{\mathrm{d}\rho_L}{\mathrm{d}t} = p\rho_{L-1}(1-\rho_L-\sigma_L) - r(\rho_L-\sigma_L) \tag{6.4a}$$
$$\frac{\mathrm{d}\sigma_L}{\mathrm{d}t} = -p\sigma_L(1-\rho_{L-1}-\sigma_{L-1}) + r(\rho_L - r\sigma_L). \tag{6.4b}$$

One can now analyze the system's dynamics by numercially integrating those equations (eqs. (6.2a-6.4b)) or via Monte Carlo simulations of the explicit particle model. With both methods, one does not find a pulsing behavior for the one lane model but a high and a low density phase depending on the ration of $\alpha$ and $r$.

## 6.4 Two-lane model

As a step of increasing complexity, we introduce a second lane and so allow some lane changing to realize an efficient method for the two types of particles to pass each other. The dynamic rules are the same as for the one-lane model but additionally particles which are blocked in their current lane change to the other lane with rate $p$ if the adjacent site is empty on the other lane.

Again, one does not find pulsing states with the model depicted in Figure 6.3. Also here only a high and a low density phase are observed. In order to observe a pulsing phase one has to introduce some kind of asymmetry into the model. At least two alternatives are possible: either only one type of particles is allowed to change lanes or the type changing rates are different. In this work we focus on the case when only minus particles can change lanes. In that case the model shows three different phases: the trivial high density phase for $r = 0$, a low density phase and a pulsing phase depending on the choice of rates for injection and type conversion. Here, we want to emphasize that our minimal model has three variables only, namely $p, \alpha$ and $r$.

In order to predict the density profiles and particle fluxes analytically, the master equa-

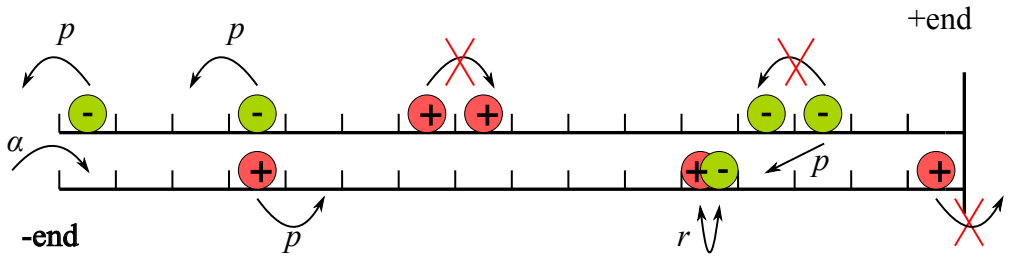


**Figure 6.3:** Sketch of the possible transitions. Red (plus) particles can hop with rate $p$ from the left to the right. Green (minus) particles hop with rate $p$ from the right to the left. Furthermore, the particles can change their type with rate $r$ from plus to minus and vice versa. Additionally, the particles now change lanes with rate $p$ if the adjacent site on the present lane is blocked on free on the other lane.

tions for the particle densities are set up. We assume that the two lanes are equivalent in the following. Therefore, the densities are the same on the two lanes for both, plus and minus particles. By the use of a mean-field ansatz the densities of plus ($\rho_i$) and minus ($\sigma_i$) particles at position $i$ evolve in the bulk according to the equations

$$\begin{aligned}\frac{\mathrm{d}\rho_i}{\mathrm{d}t} =& -p\rho_i(1-\rho_{i+1}-\sigma_{i+1}) + p\rho_{i-1}(1-\rho_i-\sigma_i) \\ & - r(\rho_i+\sigma_i)\end{aligned} \tag{6.5a}$$

$$\begin{aligned}\frac{\mathrm{d}\sigma_i}{\mathrm{d}t} =& -p\sigma_i(1-\rho_{i-1}-\sigma_{i-1}) + p\sigma_{i+1}(1-\rho_i-\sigma i) \\ & - p\sigma_i(\rho_{i-1}+\sigma_{i-1})(1-\rho_{i-1}-\sigma_{i-1}) + p\sigma_{i+1}(\rho_i+\sigma_i)(1-\rho_i-\sigma_i) \\ & + r(\rho_i-\sigma_i)\end{aligned} \tag{6.5b}$$

and

$$\frac{\mathrm{d}\rho_1}{\mathrm{d}t} = \alpha(1-\rho_1-\sigma_1) - p\rho_1(1-\rho_2-\sigma_2) - r(\rho_1-\sigma_1) \tag{6.6a}$$

$$\begin{aligned}\frac{\mathrm{d}\sigma_1}{\mathrm{d}t} =& -p\sigma_1 + p\sigma_2(1-\rho_1-\sigma_1) + p\sigma_2(\rho_1+\sigma_1)(1-\rho_1-\sigma_1) \\ & + r(\rho_1-\sigma_1)\end{aligned} \tag{6.6b}$$

at the open left and

$$\frac{\mathrm{d}\rho_L}{\mathrm{d}t} = p\rho_{L-1}(1-\rho_L-\sigma_L) - r(\rho_L-\sigma_L) \tag{6.7a}$$

$$\begin{aligned}\frac{\mathrm{d}\sigma_L}{\mathrm{d}t} =& -p\sigma_L(1-\rho_{L-1}-\sigma_{L-1}) - p\sigma_L(\rho_{L-1}+\sigma_{L-1})(1-\rho_{L-1}-\sigma_{L-1}) \\ & + r(\rho_L-\sigma_L)\end{aligned} \tag{6.7b}$$

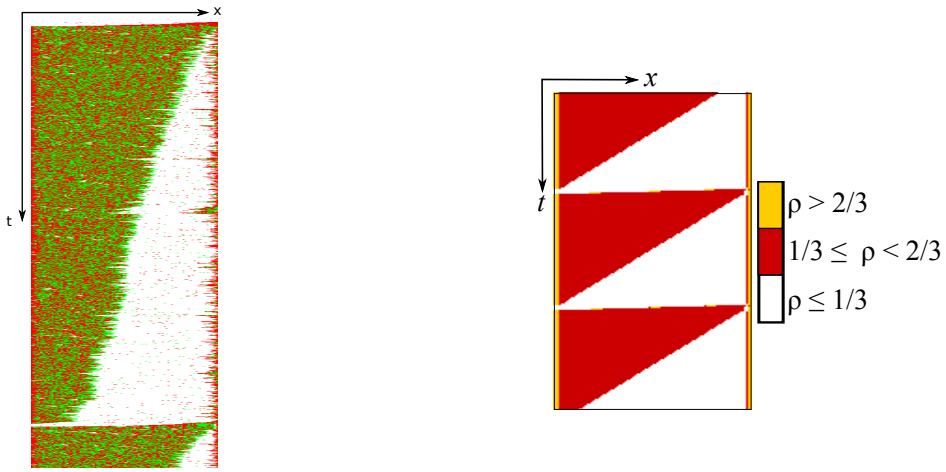


**(a)** **(b)**

**Figure 6.4:** Kymographs of the **(a)** particle model and **(b)** the direct integration of the mean field equations. In both models a pulsing behavior occurs. In the particle model **(a)** the red (green) dots are single plus (minus) particles while in **(b)** the density of plus particles $\rho$ is shown. For both models an accumulation at the right boundary is observed followed by a sparsely occupied region.

at the reflecting right boundary. It is again assumed that plus particles enter and minus particles leave the system at the left boundary, while the right boundary is reflecting for both types of particles. In this set of equations only minus particles are allowed to change lanes. The direct integration of this set of equations and the Monte Carlo simulation of the particle model show qualitatively the same behavior. The kymographs - a space-time plot of the density - are given in Figure 6.4. In both models a fast filling is followed by a slow emptying process. In particular for the MF model these two processes show a very regular behavior which is, in good approximation, linear in time. We made the choice that in this chapter the analyzed model is defined by the MF equations.

The fluxes through link $i,\ i+1$ of plus and minus particles, $J_i^+$ and $J_i^-$, respectively, are defined by the following expressions

$$J_i^+ = p\rho_i(1-\rho_{i+1}-\sigma_{i+1}) \tag{6.8a}$$
$$J_i^- = -p\sigma_{i+1}[1-(\rho_i+\sigma_i)^2]. \tag{6.8b}$$

By means of these definitions, the above defined boundary conditions can then be rewritten by

$$J_0^+ = \alpha(1-\rho_1-\sigma_1) \tag{6.9a}$$
$$J_0^- = -p\sigma_1 \tag{6.9b}$$
$$J_L^+ = J_L^- = 0. \tag{6.9c}$$

Note that the fluxes of plus and minus particles are always of opposite sign.

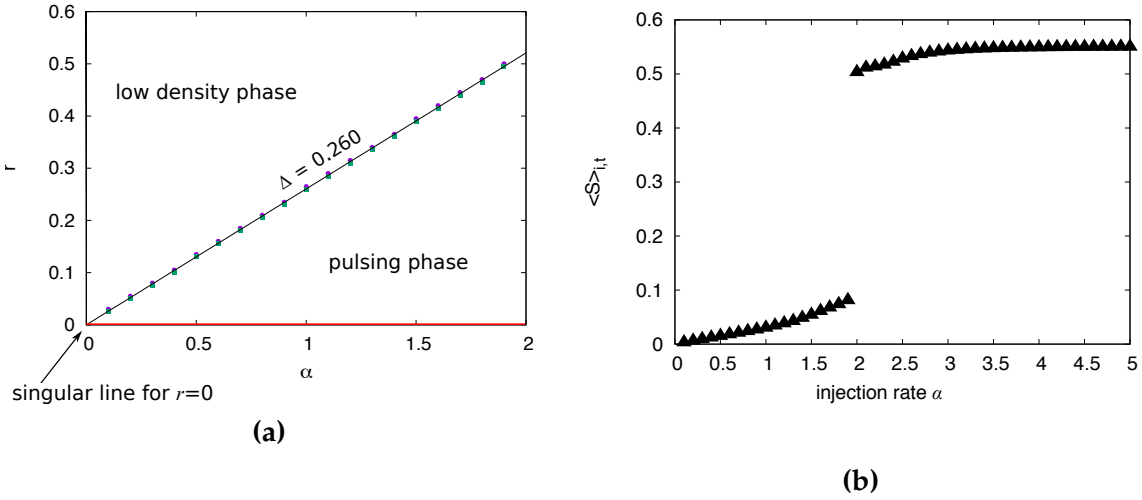


**(a)** **(b)**

**Figure 6.5:** Phase diagram **(a)** and order parameter **(b)** for the MF model. **(a)** The trivial phase for $r = 0$ is indicated by the red line. One observes that the system is in the nontrivial case $r > 0$ either in a pulsing or a low density phase. Here the purple circles belong to the low density phase and the green squares to pulsing phase. The straight line is only a guide to the eyes as the transition is so sharp that the circles and squares almost overlap. Its slope is given by $\Delta = 0.26$. **(b)** The average density $\langle S \rangle_{x,t}$ used as an order parameter shows a non-continuous transition from the low density to the pulsing phase.

## 6.5 Phase diagram

In the former section, it is stated that the system shows three different phases. In this section a more detailed description and an analysis of those phases in the MF model are given. The trivial phase is observed for $r = 0$. For that choice the density of plus particles is equal to 1 and no transition to minus particles occurs. In the following, this singular phase is not analyzed any further.

The remaining nontrivial phases are a low density phase and a pulsing phase. For both phases it is assumed that $p/r$ is at least of order $\mathcal{O}(L)$. This choice ensures that - speaking in the particle picture - the particles can invade the whole system before they change their type. In the MF model this corresponds to a finite density in all lattice sites.

In order to decide which phase the system belongs to for a given choice of parameters $\alpha$ and $r$ ($p = 2L$ is fixed in the remaining of this work), an order parameter is defined. A good choice for this is the sum of the particle densities averaged over both, time and space, $\langle S \rangle_{x,t}$. This order parameter shows a discontinuity at the phase transition from a value close to zero in the low density phase to a value bigger than one half in the pulsing phase. The phase diagram is shown in Figure 6.5. Obviously, a linear relation between $\alpha$ and $r$ gives the transition line between the two different phases. The slope of $\Delta = 0.26$ is independent of the particular choice of $L$ and $p$ as long $p = 2L$ holds.

In the remaining of this work two types of scaling for $r$ and $\alpha$ are chosen in order to

ensure that the system is either in the pulsing or in the low density phase given by

1. $\alpha = \mathcal{O}(1)$, $r = \mathcal{O}\left(L^{-1}\right)$ for the pulsing phase
2. $\alpha = \mathcal{O}\left(L^{-1}\right)$, $r = \mathcal{O}(1)$ for the low density phase.

In the following some preliminary general considerations and notations are useful. We define the constant total flux

$$K_i \equiv J_i^+ + J_i^-. \tag{6.10}$$

In the bulk, due to mass conservation, this total flux fulfills the relation

$$\frac{\mathrm{d}S_i}{\mathrm{d}t} = K_{i-1} - K_i \quad \text{with} \quad S_i \equiv \rho_i + \sigma_i. \tag{6.11}$$

In the stationary state (indicated by the superscript $^*$) $K_i^*$ is equal to zero since the right boundary is a purely reflecting one. That means that in the stationary state also the entrance equations must fulfill $K_1^* = 0$ which gives

$$K_0^* = 0 = \alpha(1 - S_1^*) - p\sigma_1^*. \tag{6.12}$$

By means of this relation one can estimate the entrance density of minus particles given by

$$\sigma_1^* = \frac{\alpha}{\alpha + p}(1 - \rho_1^*). \tag{6.13}$$

With the scalings introduced above $\frac{\alpha}{p} \ll 1$ is always granted and so one finds from (6.13) that in the stationary state

$$\sigma_1^* \leq \frac{\alpha}{\alpha + p} < \frac{\alpha}{p} \ll 1. \tag{6.14}$$

This relation is only true in the stationary state at the entrance for minus particles. The plus density $\rho_1^*$ can take any value depending on the value of $r$. Since the value for $\sigma_1^*$ is constant the net flow depends on $\rho_1^*$ only. Furthermore, one observes that for a set of parameters, for which the systems is in the low density phase, the flow converges towards a constant value, indicating a stationary value of $\rho_1^*$. In the next section the low density phase is analyzed.

## 6.6 Analysis of the low density phase

For the low density phase we know that the stationary flux is equal to zero

$$K_i^* = 0. \tag{6.15}$$

Using the approximation (6.13) one can determine the entrance density for both types of particles, which are then constant and much smaller than 1.

As discussed above the scaling of the rates for the low density phase is assumed to fulfill $r = \mathcal{O}(1)$ and $\alpha = \mathcal{O}\left(L^{-1}\right)$.

Throughout the whole section it is assumed that the system is in the stationary state such that for simplicity the superscript $*$ is omitted. In the low density phase the density profiles do not reveal steep gradients in space (apart from the reflecting boundary) and for this reason one can derive the partial differential equations describing the behavior of the system in the continuous space limit.

For the model described in section 6.2 a prediction for the densities in the low density phase is given at lowest order with symmetric lane changing rules [79] and also similarly for other models [9] where each lane was reserved for one species of particles. For that reason no blocking of particles of different species occurs. In this section the importance of higher order terms is demonstrated in order to obtain the full behavior along the lattice.

In order to calculate a Taylor expansion in space the continuous variable $x = i/L$ is introduced for which it is assumed that $L \gg 1$. For this choice one finds the propagation equations for the densities

$$\begin{aligned}\frac{\partial \rho}{\partial t} &= -r\left(\rho-\sigma\right) + \frac{p}{L}\frac{\partial}{\partial x}\left[\rho(\rho+\sigma-1)\right] \\ &\quad + \frac{p}{2L^2}\frac{\partial}{\partial x}\left[(1-\sigma)\frac{\partial \rho}{\partial x} + \rho\frac{\partial \sigma}{\partial x}\right] + \cdots \qquad (6.16a)\\ \frac{\partial \sigma}{\partial t} &= r\left(\rho-\sigma\right) + \frac{p}{L}\frac{\partial}{\partial x}\left[\sigma\left(1-(\rho+\sigma)^2\right)\right] \\ &\quad + \frac{p}{2L^2}\frac{\partial}{\partial x}\left[\frac{\partial \sigma}{\partial x}\left(1-(\rho+\sigma)^2\right) + \sigma\frac{\partial(\rho+\sigma)^2}{\partial x}\right] + \cdots \qquad (6.16b)\end{aligned}$$

Here the left hand side is equal to zero since it is assumed that the system is in a stationary state. Similarly, the expansion of the zero-flux condition eq. (6.12) is given by

$$0 \;=\; \rho(1-\rho-\sigma) - \sigma\left[1-(\rho+\sigma)^2\right] - \frac{1}{L}\left[\rho\frac{\partial(\rho+\sigma)}{\partial x} + \left(1-(\rho+\sigma)^2\right)\frac{\partial \sigma}{\partial x}\right] + \cdots$$

Since the system is in the low density phase no densities of the order of $\mathcal{O}(1)$ exist. Furthermore, from the preliminary calculations above and eq. (6.13) one knows that the density of minus particles at the entrance site is of order $\mathcal{O}\left(\frac{1}{L^2}\right)$. In the bulk no steep gradients in the densities occur, which allows one to assume that the derivatives of the densities are at most of the same orders. For this reason the first non-zero contributions can be of order $\mathcal{O}\left(L^{-2}\right)$. With this knowledge one can make the reasonable ansatz for the densities

$$\rho = \rho^{(1)} + \rho^{(2)} + \rho^{(3)} + \mathcal{O}\left(\frac{1}{L^5}\right) \qquad (6.17)$$

$$\sigma = \sigma^{(1)} + \sigma^{(2)} + \sigma^{(3)} + \mathcal{O}\left(\frac{1}{L^5}\right). \tag{6.18}$$

assuming that $\rho^{(k)} = \mathcal{O}\left(\frac{1}{L^{k+1}}\right)$ and similarly for $\sigma$. At lowest order one finds for eq. (6.17)

$$\rho^{(1)} - \sigma^{(1)} = 0 + \mathcal{O}\left(\frac{1}{L^3}\right). \tag{6.19}$$

Similarly, for the densities themselves the terms at highest order are given by

$$0 = -r\left(\rho^{(1)} - \sigma^{(1)}\right) - \frac{p}{L}\frac{\partial \rho^{(1)}}{\partial x} + \mathcal{O}\left(\frac{1}{L^3}\right) \tag{6.20}$$

$$0 = r\left(\rho^{(1)} - \sigma^{(1)}\right) + \frac{p}{L}\frac{\partial \sigma^{(1)}}{\partial x} + \mathcal{O}\left(\frac{1}{L^3}\right). \tag{6.21}$$

Remember, that throughout the whole section the system is assumed to be in the stationary state and so the left hand sides of eq. (6.16) are equal to zero. Those equations lead one to $\frac{\partial \sigma^{(1)}}{\partial x} = 0$ and $\frac{\partial \rho^{(1)}}{\partial x} = 0$. From the boundary condition at the entrance the constant densities $\rho^{(1)} = \sigma^{(1)}$ can be determined as

$$\rho^{(1)}(x) = \sigma^{(1)}(x) = \sigma^{(1)}(0) = \frac{\alpha}{p}. \tag{6.22}$$

In an analogous manner one finds for the next order that the terms do not bring new contributions to the densities and so

$$\rho^{(2)}(x) = \sigma^{(2)}(x) = 0 \tag{6.23}$$

with remaining orders

$$\rho = \frac{\alpha}{p} + \rho^{(3)} + \mathcal{O}\left(\frac{1}{L^5}\right) \tag{6.24}$$

$$\sigma = \frac{\alpha}{p} + \sigma^{(3)} + \mathcal{O}\left(\frac{1}{L^5}\right). \tag{6.25}$$

By going on to the next order and assuming that $\frac{\partial \rho^{(3)}}{\partial x} = \mathcal{O}\left(\frac{1}{L^4}\right)$ and $\frac{\partial \sigma^{(3)}}{\partial x} = \mathcal{O}\left(\frac{1}{L^4}\right)$, the conditions imposed by the reflecting boundary (eq. 6.15) give

$$0 = -2\left(\frac{\alpha}{p}\right)^2 + \rho^{(3)}(x) - \sigma^{(3)}(x) + \mathcal{O}\left(\frac{1}{L^5}\right). \tag{6.26}$$

and similarly for the bulk equations

$$0 = -r\left(\rho^{(3)} - \sigma^{(3)}\right) - \frac{p}{L}\frac{\partial \rho^{(3)}}{\partial x} + \mathcal{O}\left(\frac{1}{L^5}\right) \tag{6.27}$$

$$0 = r\left(\rho^{(3)} - \sigma^{(3)}\right) + \frac{p}{L}\frac{\partial \sigma^{(3)}}{\partial x} + \mathcal{O}\left(\frac{1}{L^5}\right) \tag{6.28}$$

Adding up those two last equations provides the expression

$$\frac{\partial \rho^{(3)}}{\partial x} = \frac{\partial \sigma^{(3)}}{\partial x} = -2\frac{L}{p} r \left(\frac{\alpha}{p}\right)^2 . \tag{6.29}$$

Here one uses eq. (6.26) in eq. (6.28).

Again, one can determine the constant of integration by the entrance conditions

$$\rho^{(3)}(0) = 0 \quad \text{and} \quad \sigma^{(3)}(0) = -2\left(\frac{\alpha}{p}\right)^2 . \tag{6.30}$$

By collecting the terms for the single orders the expressions for the densities are given by

$$\rho = \frac{\alpha}{p} - \frac{2rL}{p}\left(\frac{\alpha}{p}\right)^2 x + \mathcal{O}\left(\frac{1}{L^5}\right) \tag{6.31a}$$

$$\sigma = \frac{\alpha}{p}\left[1 - 2\frac{\alpha}{p}\right] - \frac{2rL}{p}\left(\frac{\alpha}{p}\right)^2 x + \mathcal{O}\left(\frac{1}{L^5}\right) . \tag{6.31b}$$

The expressions eq. (6.31) can now be compared to the direct integration of the MF equations. The result is plotted in Figure 6.6 and the agreement is excellent.

Note that one finds even in the low density phase an accumulation of plus particles at the closed end of the system. This effect occurs due to the chosen scaling for $p$ and $r$ where $p/r$ is at least of order $\mathcal{O}(L)$ to ensure that the system can be completely invaded by particles. We didn't have to take into account this steep increase in density but it is sufficient to consider the no-flux condition at the reflecting boundary to find an almost perfect agreement with numerics.

## 6.7 Analysis of the pulsing phase

The pulsing phase is the most interesting phase of the model defined in section 6.4. One can decompose the pulsing phase in two stages: the filling and the emptying stage. These two stages show qualitatively different behavior and are governed by different dynamics. The filling stage is controlled by the influx of particles from the left entrance. Particles hop along the lattice and (most probably) reach the reflecting right end before they change their type. The filling velocity is therefore related to the injection rate and therefore in the order of $\alpha$. When the system fills up a dense region grows from the right boundary to the left into the dilute region. Once the whole system is invaded by particles, the system switches to an emptying stage. The dense region shrinks again, with the density decreasing from the right to the left. One can understand this phenomenon as an effective injection of holes from the open boundary. This process is mainly governed by the type conversion rate $r$ such that the emptying time is about one order larger than the filling time.

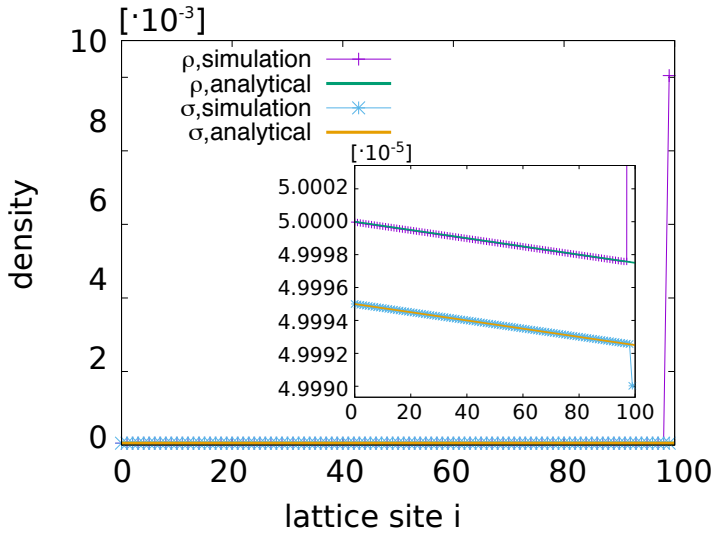


**Figure 6.6:** Density profile in the low density phase, for $\alpha = 2/L$, $r = 1$, and $p = 2L$ with $L = 100$. The inset shows the good agreement between the prediction given by eq. (6.31)) and the numerical results.

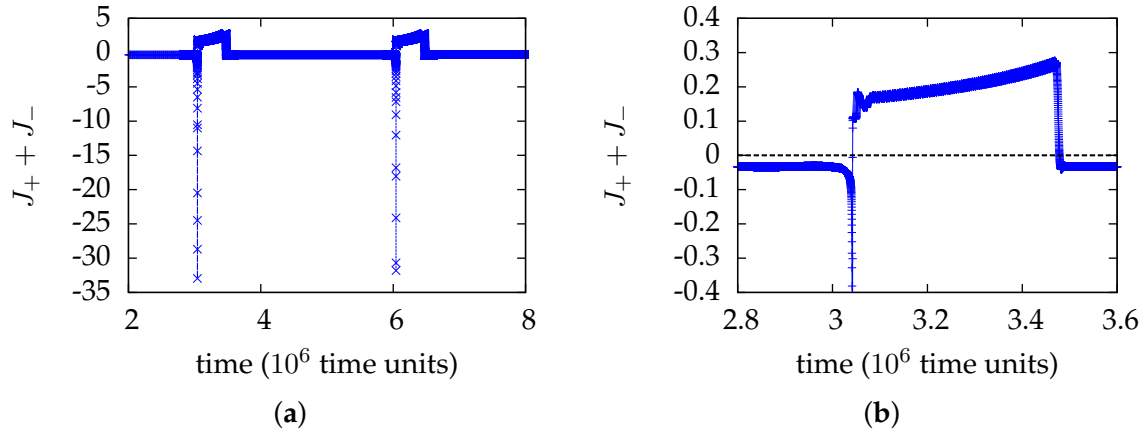


**Figure 6.7:** Net flow at the entrance ($K_0 \equiv J_0^+ + J_0^-$) as a function of time in the pulsing phase. **(a)** shows the fixed period and that the sign changes between filling and emptying stage. **(b)** is a zoom in the area of constant $K$, which is negative in the emptying stage.

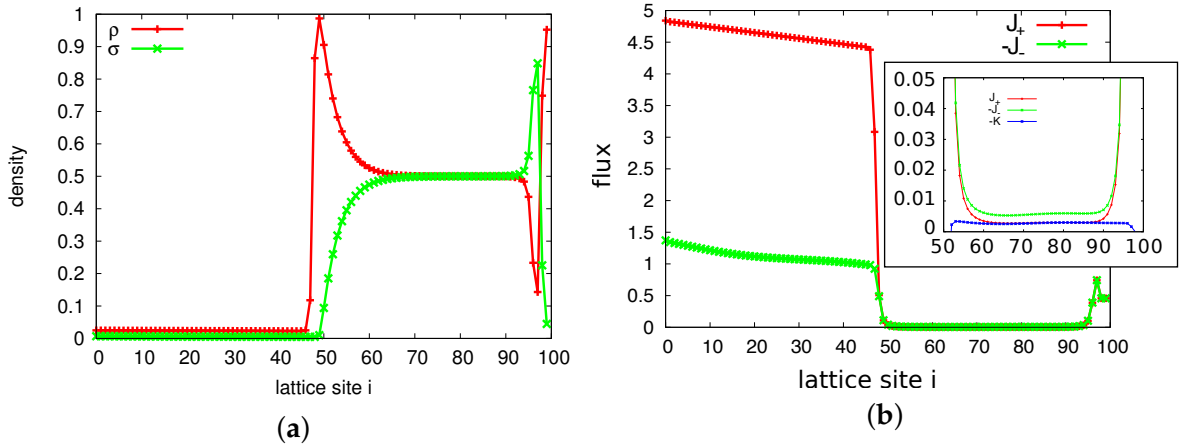


**Figure 6.8:** Density profile (**a**) and fluxes (**b**) in the filling stage. Note that actually we plot $-J^-$ to allow a direct comparison with $J^+$. The inset in (**b**) shows that the fluxes converge towards $J_- = 2J_+$ in the high density region in the filling stage. Parameter: $\alpha = 5$, $r = 0.5$

### 6.7.1 The filling stage

In this section, a different scaling for the rates than in section 6.6 is used to ensure that the system is in the pulsing phase

$$p = \mathcal{O}(L), \quad r = \mathcal{O}\left(\frac{1}{L}\right), \quad \text{and} \quad \alpha = \mathcal{O}(1). \tag{6.32}$$

In Figure 6.8 (**a**) the densities $\rho$ and $\sigma$ obtained by direct integration are shown at a given time $t$ when the system is in the filling stage of the pulsing phase. One observes that the spatial structure in the filling stage in the pulsing phase is more complex than in the low density phase. Close to the entrance the densities are low until a steep gradient in the density of plus particles occurs up to a value of $\rho(x_s) \approx 1$ at the shock position $x_s$. This high value is only reached at a single lattice site and decreases towards $1/2$ for increasing $x$. The density of minus particles increases in a smoother way towards $\sigma \approx 1/2$. Furthermore, at the reflecting boundary the density of plus particles increases since the particles are blocked. Close to the reflecting boundary both densities oscillate against each other.

Additionally, the fluxes of plus and minus particles are plotted in Figure 6.8 (**b**). In the low density region, on the left hand side of the shock position, the flux of plus particles $J_+ = p\rho_i(1-\rho_{i+1}-\sigma_{i+1})$ is bigger than the opposite flux of minus particles $J_- = -p\sigma_{i+1}[1-(\rho_i+\sigma_i)^2]$. This is necessary in order to fill the system. At the same time the situation is the other way round in the high density region on the right hand side of the shock position. Here the flux of minus particles is bigger and a relation $J_- = 2J_+$ occurs. This is characteristic for the pulsing phase. From the direct integration it is known that in the dense region the two

densities are close to $1/2$ such that the assumption

$$\rho_{\mathcal{L}} = \sigma_{\mathcal{L}} = \frac{1-\eta_{\mathcal{L}}}{2} \tag{6.33}$$

with $\eta_{\mathcal{L}} \ll 1$ is reasonable.

Using this relation now in order to calculate the flux (6.8) it is found that

$$J^{+}_{\mathcal{L}} = \frac{\eta_{\mathcal{L}}}{2} + \mathcal{O}(\eta^2_{\mathcal{L}}) \tag{6.34a}$$

$$J^{-}_{\mathcal{L}} = \eta_{\mathcal{L}} + \mathcal{O}(\eta^2_{\mathcal{L}}). \tag{6.34b}$$

This explains why in good approximation in the lowest order in $\eta_{\mathcal{L}}$ the flux of minus particles is double the flux of plus particles.

The net flow at the entrance is shown in Figure 6.7. From this figures one easily observes the periodicity in the pulsing phase. Further, it becomes obvious that the influx is higher (in absolute value) than the outflux, resulting in the much longer time needed to empty the system compared to filling.

As a first approximation of the filling velocity one can neglect the source term $r(\rho_i - \sigma_i)$. This implies that one assumes that the density of minus particles is rather small and the system fills with plus particles until a density of nearly 1 is realized along the whole lattice. With this assumption one finds

$$v_{\text{fill}} = \alpha(1-\rho(0)) = \alpha\left(1-\frac{\alpha}{p}\right). \tag{6.35}$$

For the scaling given in (6.32) a rather good agreement is observed between the predicted filling velocity and the values obtained by direct integration (compare Figure 6.9). But for increasing $r$ the measured filling velocity is smaller than the value predicted by eq. (6.35). This indicates that a measurable outflux of minus particles exists, which reduces the effective filling velocity.

In order to predict the filling velocity at a higher accuracy for increasing type changing rate $r$, we again expand the bulk equations to higher orders. Though the system is not in a stationary state, we assume that in the dilute region at the left hand side of the shock the densities are small and constant in time (compare Figure 6.8 (**a**)). Therefore, we use the following expressions for the densities

$$\rho = \rho^{(1)} + \rho^{(2)} + \rho^{(3)} + \mathcal{O}\left(\frac{1}{L^4}\right) \tag{6.36}$$

$$\sigma = \sigma^{(1)} + \sigma^{(2)} + \sigma^{(3)} + \mathcal{O}\left(\frac{1}{L^4}\right), \tag{6.37}$$

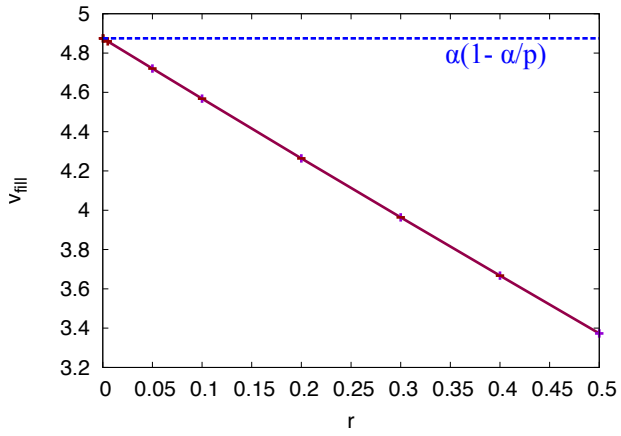


**Figure 6.9:** Type conversion rate dependence of the filling velocity $v_{\text{fill}}$ when the system is in a pulsing state (here for $L = 100$, $p = 200$, $\alpha = 5$). The dashed blue line shows the lowest order of the analytic prediction of eq. (6.35).

where we assume that $\rho^{(k)} = \mathcal{O}\left(\frac{1}{L^k}\right)$. Due to the scaling given in eq. (6.32) the densities can have contributions of order $\mathcal{O}\left(L^{-1}\right)$. The density of minus particles $\sigma$ is defined in an analogous way. In order to predict the filling velocity one has to take a non-zero particle influx $K = J_0^+ + J_0^-$ into account for the calculations. Therefore, also here we make the ansatz

$$K = K^{(1)} + K^{(2)} + K^{(3)} + \mathcal{O}\left(\frac{1}{L^4}\right). \tag{6.38}$$

$$\tag{6.39}$$

Further, we assume that for the entrance flux the relation

$$K = J_0^+ + J_0^- \tag{6.40}$$

$$= \alpha(1 - \rho_0 - \sigma_0) - p\sigma_0 \tag{6.41}$$

is fulfilled and that the system is in a stationary state.

For the first order it is found that $\rho^{(1)}$ and $\sigma^{(1)}$ are constant. Assuming for $\rho^{(1)} = \frac{\alpha}{p}$ from the preliminary calculations it is found that $K^{(1)} = \alpha$ and $\sigma^{(1)} = \frac{\alpha - K}{\alpha + p} = 0$. For the second order the equations (6.16) yield

$$\rho^{(2)} = -\frac{Lr\alpha}{p^2}x + C_\rho^{(2)} \tag{6.42}$$

$$\sigma^{(2)} = -\frac{Lr\alpha}{p^2}x + C_\sigma^{(2)} \tag{6.43}$$

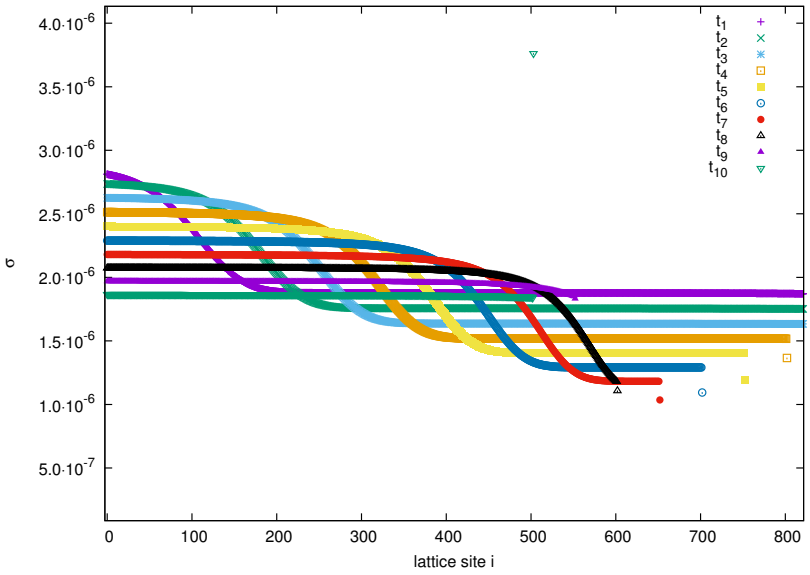


**Figure 6.10:** $\sigma(x)$ found from the numerical integration at different times. Here, a pulse propagates from the open boundary at the left to the shock position.

Again, one can use the boundary condition

$$\sigma_0^{(2)} = \frac{\alpha\rho_1^{(1)} - K_1^{(1)}}{\alpha + p} \tag{6.44}$$

$$\Leftrightarrow C_\sigma^{(2)} = \frac{\alpha^2 p^{-1} - K_1^{(1)}}{\alpha + p} \tag{6.45}$$

where the second expression comes from eq. (6.42). For the particle flux one finds by using eq 6.44

$$K^{(1)} = p\left(\rho^{(2)} - (\rho^{(1)})^2 - \sigma^{(1)}\right) = p\left(C_\rho^{(2)} - C_\sigma^{(2)}\right) - \frac{\alpha^2}{p} \tag{6.46}$$

$$= \frac{(\alpha + p)pC_\rho^{(2)}}{\alpha} - \frac{\alpha^2}{p}. \tag{6.47}$$

It is rather easy to see that one condition is missing here to find a closed form for the densities. Continuing for the next order doesn't provide any further information and no terms cancel in order to find $C_{\sigma/\rho}^{(2)}$. Comparing the results to the numerics shows that for the $\rho$ the agreement is good and that the density decreases linearly with increasing $x$. Only a constant deviation of order $\mathcal{O}\left(\frac{1}{L^2}\right)$ is observed regarding $C_\rho$. However, for $\sigma$ we find from the numerical integration of the bulk equations a non-linear density decrease along the lattice as shown in Figure 6.10. Having a look at $\sigma$ at different times one observes that it looks like a density pulse propagating from the open boundary to the shock. This emission might occur due to the moving shock which is not taken into account in this calculation.

### 6.7.2 The emptying stage

The most interesting behavior of the system unfolds in the emptying stage of the pulsing phase. It can be seen from Figure 6.4 (**b**) that the emptying stage starts with a full lattice ($\rho$,$\sigma \simeq 1/2$). Once the emptying stage begins the system splits into two regions: a dense region to the left where $\rho$,$\sigma \simeq 1/2$ is found and a dilute region to the right with $\rho$, $\sigma \ll 1$. These two regions are separated by a front structure characterized by a value close to 1 in $\sigma$ and by a density $\rho \ll 1$. This front zone occupies only a few lattice sites. As it was already observed in section 6.7.1, the net flow in the high density region is a lot smaller than in the filling stage. This is reflected by the fact that the emptying process is much smaller than the filling process as it was already seen in the kymographs (Figure 6.4).

In a first stage the system is analyzed via a direct integration of the MF equations for the densities. At a given time one finds a structure as it is shown in Figure 6.11 (**a**), which is characteristic for the emptying stage of the pulsing phase. Please note, that in the dense region the densities are slightly smaller than $1/2$ and that they are slightly bigger than zero in the dilute region just as for the filling.

Furthermore, the fluxes of plus $J_+$ and minus particles $|J_-|$ (in absolute value) as well as $|K| = |J_+ - J_-|$ are shown in Fig. 6.11 (**b**). From this figure two interesting facts are found: At first, the flux of minus particles (again in absolute value) is double the flux of plus particles in the high density region. Second, the net flux $K$ is constant in this dense region whereas it is slightly decreasing with increasing $x$ in the dilute region.

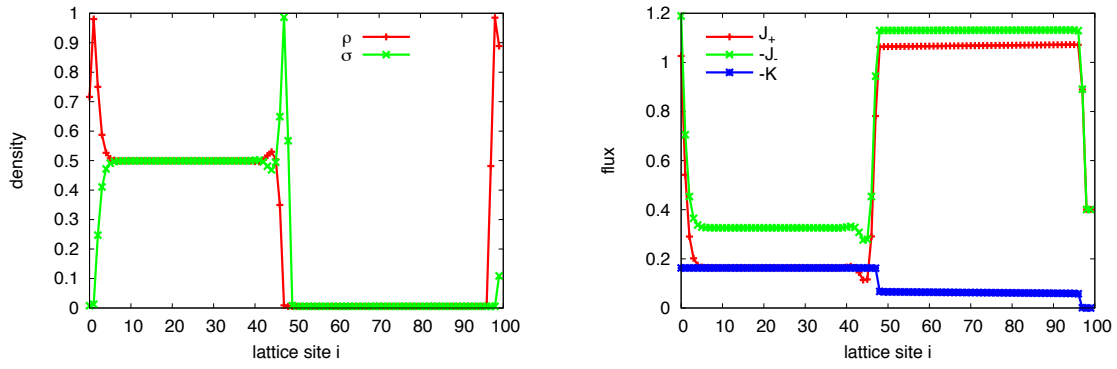


(**a**) (**b**)

**Figure 6.11:** Density profiles (**a**) and fluxes (**b**) in the emptying stage. Note that we plot $-J^-$ and $-K$ to allow a direct comparison with $J^+$. Parameters: $\alpha = 5$, $r = 0.5$

#### Shock dynamics

It is important to note that the shock seen in Figure 6.11 is not stationary but that it moves from the right closed end to the left open end in the emptying stage of the system. In order

to calculate the shock velocity one can idealize the front as a single discontinuity which separates the two regions on the left and on the right of the shock position. Then it is possible to use the Rankine-Hugoniot equations relating the densities and the fluxes on both sides of the shock. This is actually only possible in the case of mass conservation. For this reason it is necessary to neglect the source term $r(\rho - \sigma)$ in the master equations.

The fluxes of plus and minus particles on both sides of the shock shall be denoted as

$$J_X^+ = p\rho_X(1 - \rho_X - \sigma_X) \tag{6.48a}$$

$$J_X^- = -p\sigma_X[1 - (\rho_X + \sigma_X)^2]. \tag{6.48b}$$

Here the index $X = \{\mathcal{L}, \mathcal{R}\}$ indicates the flux and density on the left and right hand side of the shock, respectively. Additionally, the net current $K$ on each side of the shock is defined as

$$K_X \equiv J_X^- + J_X^+. \tag{6.49}$$

The Rankine-Hugoniot relations yield

$$J_{\mathcal{L}}^+ - J_{\mathcal{R}}^+ = v(\rho_{\mathcal{L}} - \rho_{\mathcal{R}}) \tag{6.50a}$$

$$J_{\mathcal{L}}^- - J_{\mathcal{R}}^- = v(\sigma_{\mathcal{L}} - \sigma_{\mathcal{R}}) \tag{6.50b}$$

where it is assumed that the front for both species moves at the same speed $v$.

It can now be used that $\sigma_{\mathcal{R}}$ and $\rho_{\mathcal{R}}$ are small compared to $\rho_{\mathcal{L}}$, $\sigma_{\mathcal{L}}$ such that second order terms in $J_{\mathcal{R}}^{\pm}$ can be neglected in order to determine the velocity of the moving front. Using this in the expressions (6.33-6.34) one finds

$$p\left(\frac{1}{2}\eta_{\mathcal{L}} - \rho_{\mathcal{R}}\right) = v\left(\frac{1}{2} - \frac{\eta_{\mathcal{L}}}{2} - \rho_{\mathcal{R}}\right) \tag{6.51a}$$

$$p\left(-\eta_{\mathcal{L}} + \sigma_{\mathcal{R}}\right) = v\left(\frac{1}{2} - \frac{\eta_{\mathcal{L}}}{2} - \sigma_{\mathcal{R}}\right). \tag{6.51b}$$

Eliminating $v$ from the equations (6.51) allows one to obtain a relation between $\eta_{\mathcal{L}}$ and $\rho_{\mathcal{R}} + \sigma_{\mathcal{R}}$

$$\frac{3}{2}\eta_{\mathcal{L}} = \sigma_{\mathcal{R}} + \rho_{\mathcal{R}}. \tag{6.52}$$

Inserting expression (6.52) back into equation (6.51) yields one single equation for $v$

$$v^2\left(1 - \frac{5}{2}\eta_{\mathcal{L}}\right) + v\left(\frac{\eta_{\mathcal{L}}}{2}\right) = 0 \tag{6.53}$$

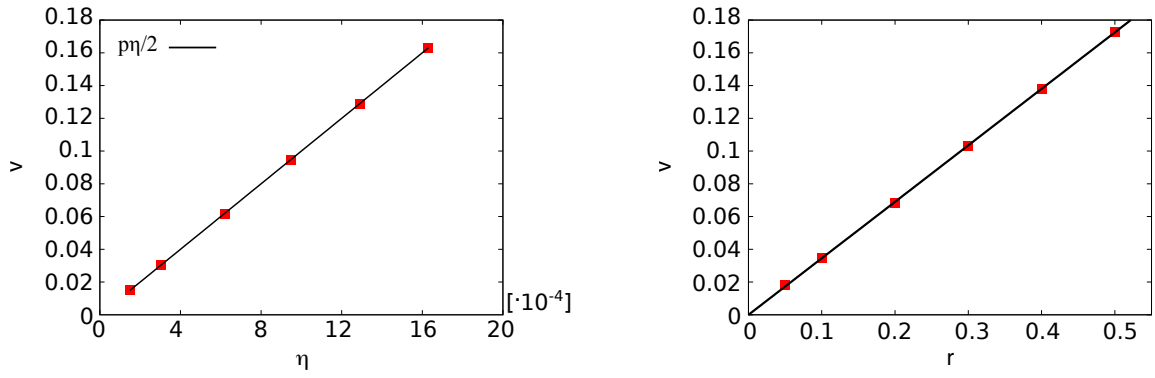


**(a)** **(b)**

**Figure 6.12: (a)** Emptying velocity $v$ vs the deviation $\eta_{\mathcal{L}}$ from density $1/2$ in the dense region and **(b)** the emptying velocity $v$ vs the type conversion rate $r$. The points on both figures correspond to the same simulations so that the value of $\eta_{\mathcal{L}}$ for the parameter values used throughout this thesis is $\eta_{\mathcal{L}} = 1.63 \cdot 10^{-3}$. In **(a)** the line corresponds to the Rankine-Hugoniot expression given in eq. (6.54) and shows very good agreement even if we neglect source terms. Furthermore, we find that the velocity is also proportional to $r$ (the line in **(b)** is a fit with slope $0.345$). Parameters: $\alpha = 5$, $p = 200$ and $r = 0.5$ in **(a)**.

such that the front moves with a velocity

$$v = 0 \quad \text{or} \quad v = -\frac{p}{2}\eta_{\mathcal{L}}. \tag{6.54}$$

In Figure 6.12 (**b**) this velocity depending on $\eta_{\mathcal{L}}$ is plotted where $\eta_{\mathcal{L}}$ has to be determined from the integration of the densities. Indeed, $\eta$ and $v$ are proportional to each other and the proportionality coefficient is well predicted by the Rankine-Hugoniot prediction. Furthermore, it was checked that $\eta_{\mathcal{L}}$ does not depend on the system size (see for example Fig. 6.13d). However, it was not possible so far to find a prediction for the value of $\eta_{\mathcal{L}}$.

Furthermore, it was observed in the numerical integration that $v$ - and thereby $\eta_{\mathcal{L}}$ as well - is proportional to $r$.

In the prediction of the shock velocity it was assumed that the domains on the left and on the right hand side of the shock are constant. In fact, this is only true at lowest order of the densities. Having a closer look at the densities in the proximity of the shock, one observes some oscillatory behavior - in the dense as well as in the dilute region.

In particular, it will be shown later that $\rho_{\mathcal{R}}$ and $\sigma_{\mathcal{R}}$ oscillate not only in space but also in time in the dilute region in the pulsing phase such that it is impossible to give a fix value for $\rho_{\mathcal{R}} + \sigma_{\mathcal{R}}$.

**Dense region**

The dynamics in the dense region are governed by the source term $r(\rho - \sigma)$, which rather moves the system to a state in which the two densities are equilibrated close to $1/2$. In the dense region one observes deviations from this bulk value only at the entrance and at the shock position. But once higher order terms are taken into account some oscillatory behavior with opposite signs in plus and minus densities occurs in a wide area of the dense region. These oscillations originate at the shock where $\sigma$ peaks to almost density 1, whereas $\rho$ drops to almost zero-density. In Figure 6.8**(a)** one can easily detect that these oscillations continue on the left hand side of the shock around the plateau value of $\rho = \sigma = 1/2 - \eta_{\mathcal{L}}$ ($\eta_{\mathcal{L}} \ll 1$) though with decreasing amplitude. In a logarithmic plot (Figure 6.13 (**b,c**)) it is easy to see that the densities decrease exponentially from the entrance towards a value $\rho_0$. Otherwise, from the shock position to the left the densities oscillate out of phase with an exponentially decreasing amplitude (cf. Figure 6.13 **b,c**).

Interestingly, the observed oscillations do not depend on the system size. In Figure 6.13 **(c)** the densities are shown for a system of size $L = 100$ and for $L = 1000$ sites with the same $\rho_0$ obtained by numerical integration. Shifting the plot for $L = 100$ such that the shocks in the two systems are at the same position shows that the agreement between the two curves is almost perfect for at least five orders of magnitude.

**Stability analysis**

To understand why oscillations occur and how the system reacts to perturbations - in space as well as in time - one can perform a stability analysis in the spirit of [39]. For this reason it is assumed in the following that the two densities have the form

$$\rho_i = \rho^* + A(t)\Lambda^i \tag{6.55a}$$

$$\sigma_i = \rho^* + B(t)\Lambda^i. \tag{6.55b}$$

Here $\rho^*$ is the stationary density which is equal for the two types of particles and in the emptying stage almost one half on the left hand side and almost zero on the right hand side of the shock. One can see those two densities as equilibrated plateaux. At the two boundaries and at the shock position $\rho$ and $\sigma$ take values of about one, respectively whereas the other one drops to almost zero. In order to analyze the effects occurring due to this small deviations from one half and zero, we perform a stability analysis.

Using the expressions given in eq. (6.55a), the bulk equations (6.2a), (6.2b) can be written in a matrix form

$$\frac{1}{p}\frac{\mathrm{d}}{\mathrm{d}t}\begin{pmatrix} A(t) \\ B(t) \end{pmatrix} = \mathbf{M}\begin{pmatrix} A(t) \\ B(t) \end{pmatrix} \tag{6.56}$$

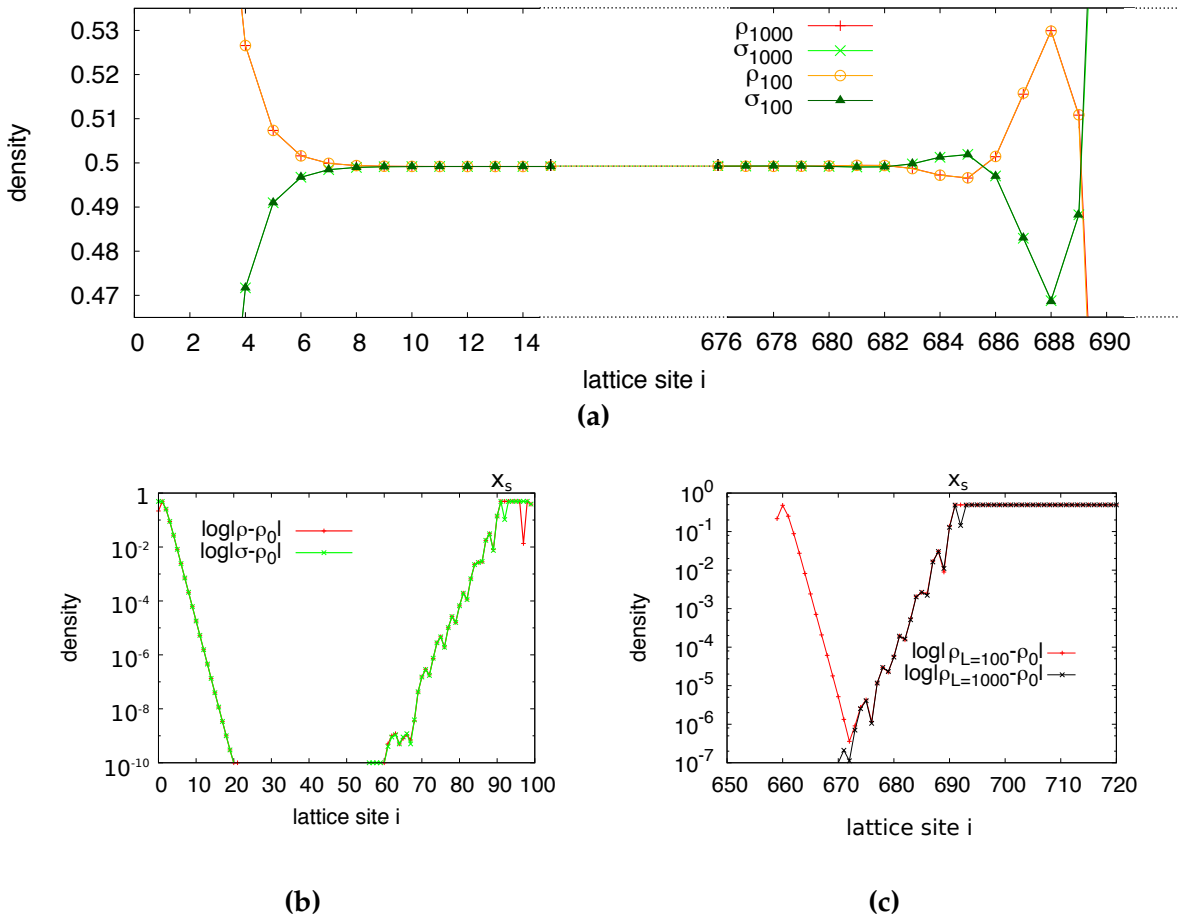


**Figure 6.13:** Oscillatory behavior in the dense region of the emptying stage. **(a)** Zoom on the density profiles $\rho$ and $\sigma$, for $L = 100$ and $L = 1000$ around $1/2$. One sees the decaying density at the entrance and the oscillatory behavior on the left hand side of the shock position $x_s$. **(b)** $\log(|\rho - \rho_0|)$ and $\log(|\sigma - \sigma_0|)$, **(c)** $\log(\rho - \rho_0)$ for $L = 100$ and $L = 1000$. Note, that we use the same $\rho_0 = \sigma_0 = 0.499182602$ for the two different lattice lengths. The four figures were obtained for $L = 100$ (or$L = 1000$ when stated) Parameters: $\alpha = 5$, $r = 0.5$, $p = 200$.

with the two dimensional matrix $M$ defined in the following way

$$\mathbf{M} = \begin{pmatrix} (\Lambda-1)\left[\rho^* - \frac{1-2\rho^*}{\Lambda}\right] - \frac{r}{p} & (\Lambda-1)\,\rho^* + \frac{r}{p} \\ (\Lambda-1)\left[\frac{-4\rho^{*2}}{\Lambda}\right] + \frac{r}{p} & (\Lambda-1)\left[1 - 4\rho^{*2} - \frac{4\rho^{*2}}{\Lambda}\right] - \frac{r}{p} \end{pmatrix}. \tag{6.57}$$

The solutions for this equation (6.56) are only non-trivial if the condition $\det\left|M - \frac{\ln\omega}{p}\mathbb{I}\right| = 0$ is fulfilled. Assuming that $A(t)$ and $B(t)$ are much smaller than 1 allows one to neglect second order terms in $A(t)$ and $B(t)$. In that case calculating the determinant leaves one with an expression which is quadratic in $\omega$ and of fourth order in $\Lambda$ given by

$$\begin{aligned} 0 = \omega^2 - \omega &\left[(\Lambda-1)\Big(1 + \rho - 4\rho^{*2} - \Lambda^{-1}(1 - 2\rho^* + 4\rho^{*2})\Big) - \frac{2r}{p}\right] \\ &(\Lambda-1)^2\left[\rho^*(1-4\rho^{*2}) - \Lambda^{-1}\left(1 - 2\rho^* - 4\rho^{*2} + 8\rho^{*3}\right) + 4\rho^{*2}\Lambda^{-2}(1-2\rho^*)\right] \\ &- (\Lambda-1)\frac{r}{p}\left[1 + 2\rho^* - 4\rho^{*2} - \Lambda^{-1}\left(1 - 2\rho^* + 8\rho^{*2}\right)\right]. \end{aligned} \tag{6.58}$$

In order to obtain analytic results we first check for spatially homogeneous perturbations corresponding to $\Lambda = 1$, which gives us an easy quadratic equation in $\omega$

$$\omega\left(\omega + \frac{2r}{p}\right) = 0 \tag{6.59}$$

with the obvious roots

$$\omega_1 = 0 \quad \wedge \quad \omega_2 = -\frac{2r}{p}. \tag{6.60}$$

These roots, which give the eigenvalues of matrix **M**, can now be used to find the corresponding eigenvectors which are given by

$$v_1 = \begin{pmatrix} 1 \\ 1 \end{pmatrix} \quad \wedge \quad v_2 = \begin{pmatrix} 1 \\ -1 \end{pmatrix} \tag{6.61}$$

under the assumption that $\Lambda = 1$. The symmetric case $v_1$ is stationary and corresponds to an equal shift in both densities. The asymmetric case $v_2$ gives a *dynamically* stable solution which converges towards $\rho^*$ from higher density in $\rho$ and from a lower one in $\sigma$.

Similarly one can check the spatial stability by assuming a *stationary* perturbation corresponding to $\omega = 0$. In that case the equation to solve is cubic in $\Lambda$ and is given by

$$\begin{aligned} 0 = &\frac{r}{p}\left[1 + 2\rho^* - 4\rho^{*2} - \Lambda^{-1}\left(1 - 2\rho^* + 8\rho^{*2}\right)\right] \\ &- (\Lambda-1)\left[\rho^*(1-4\rho^{*2}) - \Lambda^{-1}\left(1 - 2\rho^* - 4\rho^{*2} + 8\rho^{*3}\right) + 4\rho^{*2}\Lambda^{-2}(1-2\rho^*)\right]. \end{aligned} \tag{6.62}$$

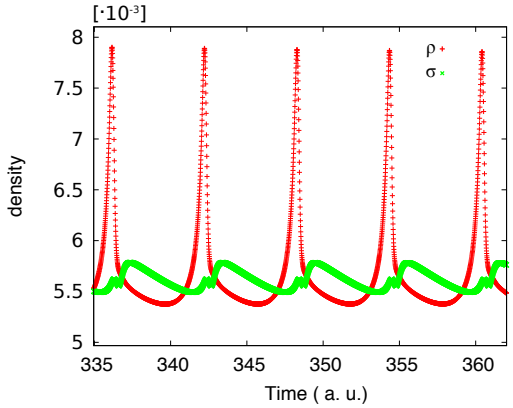


**Figure 6.14:** $\rho_{\mathcal{R}}$ and $\sigma_{\mathcal{R}}$ at a fixed lattice site $i$ evolving with time with $\alpha = 5$ and $r = 0.5$.

The character of the three roots are density-dependent. For small $\rho^* \approx 0$ we find three real roots but there exists a critical density $0 < \tilde{\rho} < \rho^* < \frac{1}{2}$ for which two roots become a complex conjugated pair. The modulus of this pair takes values bigger than 1 for a density $\rho_c$, which is very close to one half. In that case the perturbations are *spatially* unstable in a way that with increasing $i$ the perturbation diverges. Furthermore, due to a non-zero imaginary part one observes an oscillatory behavior of the densities around the equilibrated plateaux in the direct integration which is bounded by density one.

With the stability analysis one cannot determine when the phase transition takes place because the injection rate $\alpha$ is not taken into account here.

### 6.7.3 Dilute region

In the dilute region in the emptying stage (on the right hand side of the shock) one finds from the numerical integration fast oscillations in $\rho_i$ and $\sigma_i$ in time $t$ at a fixed lattice site $i$ as it is shown in Figure 6.14. Note, that neither $\rho_i$ nor $\sigma_i$ change in a sinusoidal way but that their time evolution reflects the non-linearity of (6.2a), (6.2b). From this structure it is easy to see why the Rankine-Hugoniot equations (6.52) are not sufficient to predict the densities in the dilute region. This indicates that taking the source term into account is crucial to find a full solution in this region. And also the time evolution of the shock profile is not negligible to find the full solution in this region. One finds a very stable period of about 5 s for these oscillations which corresponds to the motion of the shock front from one lattice site to the next.

In large systems is becomes obvious how these temporal density changes at each lattice site arise. Every time the shock moves by one lattice site to the left, it emits a density pulse to the right. This behavior is depicted in Figure 6.15 where the densities close to the shock are shown at different times which are smaller than the time the shock needs to move by one site. The amplitude of this pulse decreases exponentially with space until it reaches the right boundary.

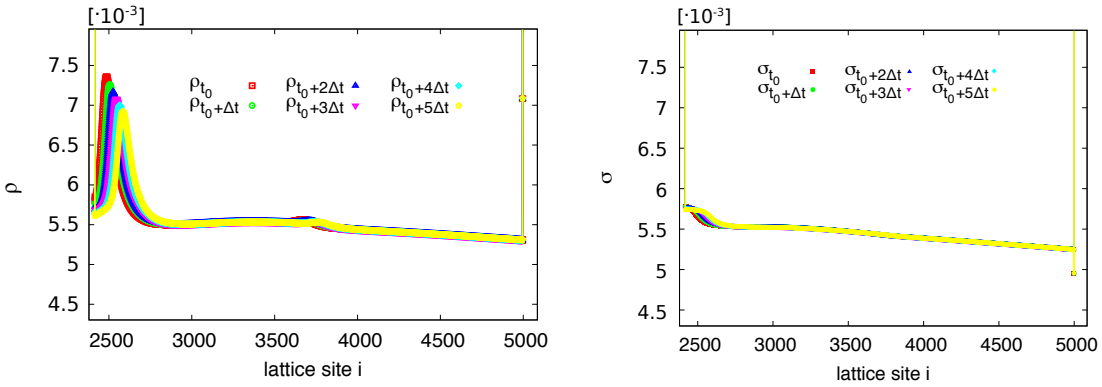


**(a)** **(b)**

**Figure 6.15:** Time propagation of the densities is connected to the emission of a density pulse. Particle densities **(a)** $\rho$ and **(b)** $\sigma$ at different times. The densities show some pulse induced by the motion of the shock position. Parameter: $\alpha = 5, r = 0.5$

### 6.7.4 Transition between the low density phase and the pulsing phase

In this section we want to characterize how the transition between the pulsing and low density phase is characterized. First, we have a look at the numerical density profiles for values of $\alpha$ close to the phase transition. We observe that with increasing $\alpha$ the single peak in $\rho$ close to the reflecting boundary detaches from the boundary and at the same time a peak in $\sigma$ arises (cf. Fig. 6.16). Once the two densities have some contact at one site of the lattice, the transition from the low density phase to the pulsing phase occurs.

In the particle picture, one can understand better why the phase transition occurs when two densities approach the value $1/2$ at the boundary. In the low density phase a boundary layer of plus particles exists at the reflecting boundary. After some time these plus particles change their type and therefore their hopping direction and so leave the system again. In case $\alpha$ is small, these new minus particles have enough time to leave the dense region at the reflecting boundary. With increasing $\alpha$ more and more plus particles arrive before those in the boundary layer can change their type and can leave. In that case the minus particles, which are created close to the boundary, cannot leave the system anymore. The density in both, plus and minus particles, increases and approaches $1/2$. This mutual blocking is necessary for the system to fill and trigger the pulsing phase.

## 6.8 Continuous space description

Considering the results shown above it is obvious that the source term has to be taken into account to describe the system A Taylor expansion of eqs. (6.2a) and (6.2b) in $\rho$ and $\sigma$ in the

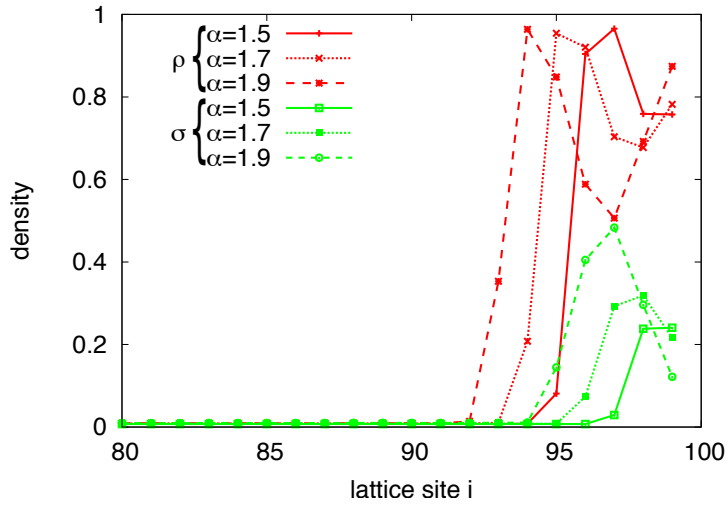


**Figure 6.16:** $\rho$ and $\sigma$ for $r = 0.5$ close to the reflecting boundary for different values of $\alpha$ and a system of length $L = 100$.

first order of $x = i/L$ is performed, which yields

$$\frac{\partial \rho}{\partial t} = (2\rho - 1 + \sigma)\frac{\partial \rho}{\partial x} + \rho\frac{\partial \sigma}{\partial x} - r(\rho - \sigma) \tag{6.63}$$

$$\frac{\partial \sigma}{\partial t} = -2\sigma(\rho + \sigma)\frac{\partial \rho}{\partial x} - \left(2\sigma(\rho + \sigma) - 1 + (\rho + \sigma)^2\right)\frac{\partial \sigma}{\partial x} + r(\rho - \sigma). \tag{6.64}$$

One way to find solutions for a set of partial differential equations is the method of characteristics. In order to apply it, it is necessary that the system is hyperbolic. For the equations written in the following form

$$\frac{\partial}{\partial t}\begin{pmatrix}\rho \\ \sigma\end{pmatrix} + \mathbf{A}\frac{\partial}{\partial x}\begin{pmatrix}\rho \\ \sigma\end{pmatrix} = \begin{pmatrix}b_1 \\ b_2\end{pmatrix} \tag{6.65}$$

the eigenvalues of the matrix $\mathbf{A}$ have to be are real and distinct for the system to be hyperbolic [59].

For the model described in section 6.4 the matrix $\mathbf{A}$ is given by

$$\mathbf{A} = \begin{pmatrix}-2\rho + 1 - \sigma & -\rho \\ 2\sigma\,(\rho + \sigma) & 2\sigma\,(\rho + \sigma) - 1 + (\rho + \sigma)^2\end{pmatrix} \tag{6.66}$$

and the inhomogeneity **b** by

$$\begin{pmatrix} b_1 \\ b_2 \end{pmatrix} = r(\rho - \sigma) \begin{pmatrix} -1 \\ 1 \end{pmatrix}. \tag{6.67}$$

One can find an expression of the two eigenvalues of **A** depending on the particle densities $\rho$ and $\sigma$

$$\begin{aligned} \lambda_{\pm}^{I} =& 2\sigma\rho + \frac{3}{2}\sigma^2 + \frac{1}{2}\rho^2 - \rho - \frac{1}{2}\sigma \\ & \pm \frac{1}{2} \cdot \Bigg( 9\sigma^4 + (24\,\rho + 6)\,\sigma^3 + \left(12\rho - 11 + 22\,\rho^2\right)\sigma^2 \\ & + \left(-12\rho - 4 + 8\rho^3 + 10\,\rho^2\right)\sigma + \left(\rho^2 + 2\rho - 2\right)^2 \Bigg)^{\frac{1}{2}}. \end{aligned} \tag{6.68}$$

The eigenvalues are then real and distinct if and only if the radicands of the eigenvalues are bigger than zero. These radicands are plotted for $0 \leq \sigma \leq 1$ and $0 \leq \rho \leq 1$ in Fig. 6.17. Note that only combinations of $\rho + \sigma \leq 1$ are allowed. In Figure 6.17 **(a)** we show the radicands of eq. 6.68. Here the white regions indicate that the radicands are either equal to or smaller than zero which results in non-distinct or complex eigenvalues. Thus, the system is of so-called *mixed type*. That also explains why one cannot use the method of characteristics in that case. In that method the eigenvalues correspond to the speed with which the characteristic propagates and so a complex value does not make sense in this frame.

In order to detect whether the densities obtained by the direct integration ever take these values in the white region the radicands are calculated at one given site $i$ in the pulsing phase, shown in Figure 6.18. One observes that the values become negative when the shock or the filling goes through this lattice site. These situations correspond to a situation when the local mass conservation is not given. This destroys the hyperbolic character of the equations.

Obviously, the system is not hyperbolic in the whole phase space $\{\rho, \sigma\} \in \{[0,1]x[0,1]\}$. However, from the direct integration of the discrete model we find a perfect periodicity and stable solutions for the densities with time.

## 6.9 Effective Markov-chain approach

In order to predict the emptying velocity one has to realize that a decrease in the overall density can only take place, if "holes" from the open boundary are injected. These holes are created by stochastic fluctuations once a blocking of an empty site in the entrance region exists. The moment the left-most plus particle, which blocks the entrance/exit, converts

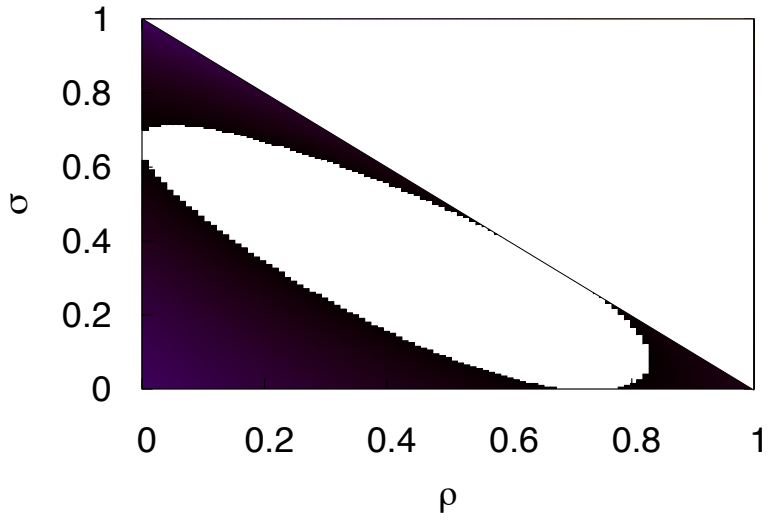


**Figure 6.17: (a)**The radicands of the square roots of (6.68) for $0 \leq \sigma \leq 1$ and $0 \leq \rho \leq 1$. Note that only values $\rho + \sigma \leq 1$ are allowed. In the white region the Eigenvalues are smaller or equal to 0, corresponding to complex or equal eigenvalues. For these values the system is no longer hyperbolic.

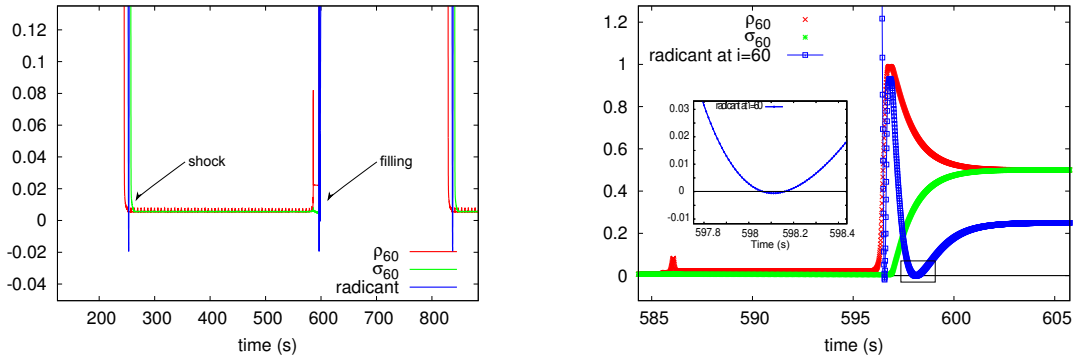


**(a)** **(b)**

**Figure 6.18:** The plot shows the densities $\rho_i$, $\sigma_i$ and the radicand of eq.(6.68) depending on $(\rho_i, \sigma_i)$ over time $t$, at a fixed site $i = 60$. In **(a)** we see one whole filling and emptying process. We observe that, when both the 'filling front' or 'emptying front' go through site $i$, the system becomes non hyperbolic (i.e. the radicand of eq. 6.68 is negative). In **(a)** we zoom in on the time interval when the system fills. We observe that during this filling stage, the system becomes non-hyperbolic, first, when the filling front arrives on site $i$, and again when the densities converge to $1/2 - \eta_{\mathcal{L}}$ (inset).

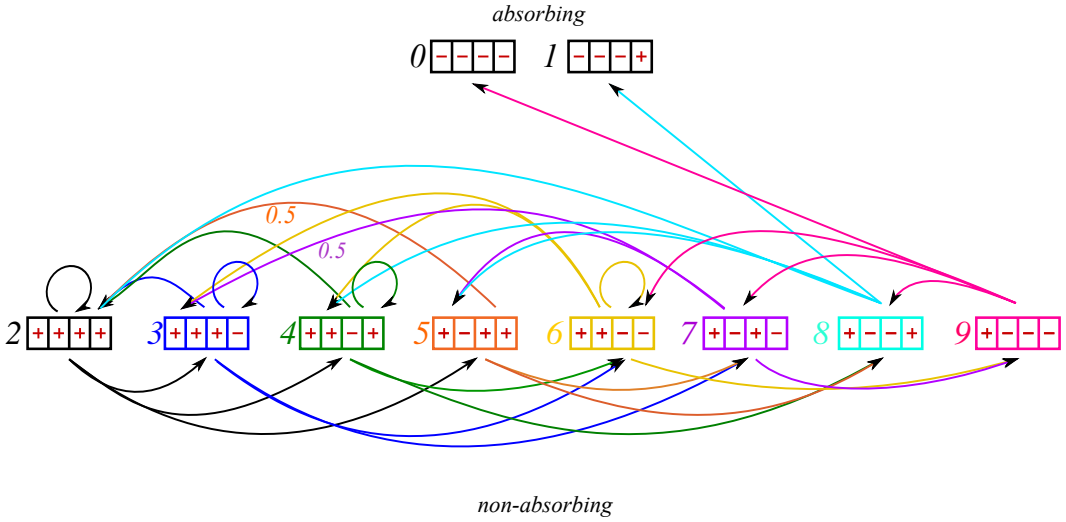


**Figure 6.19:** Sketch of all possible transitions in the simplified Markov chain approach. All probabilities are 0.25 apart from the transitions from state 5 to state 2 and from state 7 to state 3 which are 0.5.

its type, those new minus particles can leave the system. In case a plus particle is injected before the last minus particles leaves the system, a number of vacant sites are created, which can be transported through the bulk.

In the Fig. 6.19 one sees that the region at the entrance, where the densities $\rho$ and $\sigma$ change, is quite thin. Therefore, we introduce a Markov chain approach in order to describe the particle dynamics near the entrance. We assume a lattice of 4 sites. The slowest dynamic in the system is the type conversion. To estimate the time the systems takes to empty we first assume that only this conversion takes place and no other transitions are allowed. We introduce for that reason 9 different states: 2 absorbing ones and 7 non-absorbing ones (see Fig. 6.19). In general, all probabilities to go from one state to the other is equal to 0.25. There are two exception, from state 5 to state 2 and from state 7 to state 3, here the probability is 0.5. We assume that in the case of the leftmost particle flipping from $(+)$ to $(-)$ the second minus particles leaves also immediately and fills again with plus particles. Like this state 2 can be reached by flipping the first and the second particle.

We can write down the transition matrix $\underline{\underline{P}}$ for those states. Since two absorbing states exist, it is possible to write $\underline{\underline{P}}$ in a canonical form:

$$\underline{\underline{P}} = \begin{bmatrix} \underline{\underline{1}} & \underline{\underline{0}} \\ \underline{\underline{R}} & \underline{\underline{Q}} \end{bmatrix}, \tag{6.69}$$

where $\underline{\underline{1}}$ is the two-dimensional identity matrix which represents the absorbing states. The matrix $\underline{\underline{R}}$ gives the transitions from non-absorbing to absorbing states and $\underline{\underline{Q}}$ gives the transitions from non-absorbing to non-absorbing states. With above sketch (Fig. 6.19) we can

easily write down $\underline{\underline{R}}$

$$\underline{\underline{R}}^T = \begin{bmatrix} 0 & 0 & 0 & 0 & 0 & 0 & 1/4 & 0 \\ 0 & 0 & 0 & 0 & 0 & 0 & 0 & 1/4 \end{bmatrix} \tag{6.70}$$

and $\underline{\underline{Q}}$

$$\underline{\underline{Q}} = \begin{bmatrix} 1/4 & 1/4 & 1/4 & 1/4 & 0 & 0 & 0 & 0 \\ 1/4 & 1/4 & 0 & 0 & 1/4 & 1/4 & 0 & 0 \\ 1/4 & 0 & 1/4 & 0 & 1/4 & 0 & 1/4 & 0 \\ 1/2 & 0 & 0 & 0 & 0 & 1/4 & 1/4 & 0 \\ 0 & 1/4 & 1/4 & 0 & 1/4 & 0 & 0 & 1/4 \\ 0 & 1/2 & 0 & 1/4 & 0 & 0 & 0 & 1/4 \\ 0 & 0 & 1/4 & 1/4 & 0 & 0 & 0 & 1/4 \\ 0 & 0 & 0 & 0 & 1/4 & 1/4 & 1/4 & 0 \end{bmatrix}. \tag{6.71}$$

To predict the mean time to empty the system, we calculate the mean time we spend in the non-absorbing states before we reach one of the two absorbing states. The system evolves in time according to

$$\underline{x_n} = \underline{x_0}\,\underline{\underline{P}}^n \tag{6.72}$$

with the initial state $x_0 = (0\ 0\ 1\ 0\ 0\ 0\ 0\ 0\ 0\ 0)$, meaning that we always start in state 2 ($\triangleq$++++). It is easy to show that

$$\underline{\underline{P}}^n = \begin{bmatrix} \underline{\underline{1}} & \underline{\underline{0}} \\ \underline{\underline{1}} + \left(\sum_{i=1}^{n-1} \underline{\underline{Q}}^i\right) \underline{\underline{R}} & \underline{\underline{Q}}^n \end{bmatrix}, \tag{6.73}$$

with $n \in \mathbb{N}$.

Since two absorbing states exist in the system it is almost for sure, that the system reaches one of these two states with $n \to \infty$, and so $\underline{\underline{Q}}^n$ goes to $\underline{\underline{0}}$. One can then write $\underline{\underline{P}}$ as

$$\underline{\underline{P}}^n = \begin{bmatrix} \underline{\underline{1}} & \underline{\underline{0}} \\ \underline{\underline{N}}\,\underline{\underline{R}} & \underline{\underline{0}}^n \end{bmatrix}, \tag{6.74}$$

with $n \to \infty$ and

$$\underline{\underline{N}} := \underline{\underline{1}} + \underline{\underline{Q}} + \underline{\underline{Q}}^2 + .... \tag{6.75}$$

By multiplying and rearranging eq. (6.75) one finds

$$\underline{\underline{N}} = (\underline{\underline{1}} - \underline{\underline{Q}})^{-1}. \tag{6.76}$$

The matrix element $N(i, j)$ gives the expected number of periods that the chain spends in the $j$-th non-absorbing state given that the evolution began in the $i$-th non-absorbing state. Summing over all states $j$ gives then the number of periods $Z$ the systems spends in the non-absorbing states before being absorbed given that it started with state $i$.

In our system the four particles change their type with rate $r$. So the average time $\delta t$ between two events is given by $\delta t = (4r)^{-1}$.

To inject a hole into the system we need that a plus particles enters the system before all minus particles left the chain. Since particles hop with rate $p$ and enter the system with $\alpha$ this event has the probability $p(p + \alpha)^{-1}$. So to approximate the average time to induce $2L$ holes into the system $\Delta t$ we have

$$\Delta t = \left( \sum_k k \cdot Z \left( \frac{p}{\alpha + p} \right)^k \right) \cdot 2L\delta t = Z. \tag{6.77}$$

If we calculate this quantity for the parameter we use for the simulations, we get a value which is about $10^3$ too big. We know from the previous calculations that the particle asymmetry is crucial for obtaining the pulsing state. This indicates that one has to take into account that minus particles can change lanes and therefore alter the simple pattern used in this approach.

## 6.10 Chapter conclusion

At first we introduced a particle model inspired by [79], in which two types of particles hop with rate $p$ along two lattice lanes with a given length $L$. At the left boundary plus particles are injected with rate $\alpha$ and minus particles can leave with rate $p$, while the right boundary is a reflecting one. The two types (plus and minus) differ in their hopping direction but also in their lane changing behavior. Plus particles cannot change lanes whereas minus particles can, in case the adjacent site in the same lane is already occupied by another particle. Along the whole system particles can convert their type with rate $r$. For $p$ large enough, such that particles invade the system, the phase diagram is divided into two phases, a low density phase and a pulsing phase where the system shows spontaneous

pulsing in a sense that it fills until the density of particles is almost one and then empties again.

Inspired by this explicit particle model, a discrete mean-field model was introduced. It was defined by the master equations in the particle densities $\rho$ (for plus particles) and $\sigma$ (for minus particles). We found that it also exhibits either a very regular pulsing behavior or a low density phase (excluding the trivial case where particles do not change their type). We started our analysis in this low density phase. Here we were able to predict the (stationary) density profile with $L$.

The pulsing phase is more complicated to analyze. In the filling stage, for a small type changing rate we found an approximation for the filling velocity by assuming that $r \ll \alpha$.

In the emptying stage the system's dynamics are very slow. A front moves backwards, separating a dense region on the left and a dilute region on the right. In the dense area (between the entrance and the shock position) the two densities deviate from $\frac{1}{2}$ only by very small values, typically $10^{-3}$ or smaller, depending on the type conversion rate. In a first approximation we neglected type conversion and predicted the shock's velocity as a function of this deviation, by a mass conservation argument. The agreement was very good (Fig. 6.12). In the dense region some oscillations in the densities were observed, which are triggered by the shock movement on the discrete lattice. We performed a stability analysis of this region around some plateau solutions. At first, it was figured out that temporal perturbations decay exponentially in time, such that the system is dynamically stable. Assuming time-independent but spatially non-homogeneous perturbations, three exponentially decaying profiles were found for low particle densities. Above a critical plateau density, two of the three roots become imaginary with a modulus bigger than one. Corresponding to the spatial oscillations found numerically in the density profiles along the filament and the exponentially increasing density from the bulk plateau solution to the shock.

In the dilute region the densities show some oscillating behavior as well. We observed that density pulse are released from the shock and propagate through the system to the reflecting boundary. This pulse emission is connected to a hopping of the shock from one lattice site to the next one.

Furthermore, an expansion of the system's master equations in a form continuous in space was given. It was obtained in first order a set of partial differential equations which is of mixed type (hyperbolic/elliptic). The non-hyperbolicity occurs in the filling as well as at the shock position.

Finally, an effective Markov chain model was introduced in order to predict the emptying velocity in the pulsing phase. The predicted velocity is three orders of magnitude too fast, which indicates again that the asymmetric lane changing behavior is crucial in order to obtain a pulsing phase.

# Chapter 7

# Conclusion and Outlook

Bidirectional motion was observed for many types of different intracellular cargo, from small vesicles like endosome to whole organelles like mitochondria [8,110]. In the last years bidirectionally moving cargos affected much interest, both from experimentalists and theoreticians [3, 33, 34, 43, 46, 49, 71, 72, 86, 120]. One key question was, whether it has to be controlled at all, like for instance that the cell switches off one team at a time in order to reverse the moving direction, or whether stochastic fluctuations are sufficient to observe a bimodal velocity distribution [17, 46, 72, 86]. On the theoretical side, Müller *et al.* [86] introduced a mean-field description of cargo transported by two teams of motors. The main assumption in their model is given by an equal load sharing between the motors within one team, wherefore we call it a mean-field model. For a rather broad regime of parameters their model definition results in bimodal (or trimodal) symmetric distributions for both, velocity and in the number of attached motors. By means of our EPB-model, which takes the force fluctuations for the single motors explicitly into account, we demonstrated that these bimodal distributions are pure mean-field artifacts, which occur due to an implicitly assumed synchronization. With the EPB-model, we could reproduce these states by introducing an artificial motor-motor activation. This one has to be very strong and include at least three times the amount of motors which are estimated to be involved in intracellular transport [64]. Hence, we concluded that the mean-field description is not relevant for the modeling of intracellular transport. The importance of fluctuations in the stepping of motors has also been observed experimentally. In [6] it was found that, even within a team of identical motors, individual motors can build up substantial forces in both hindering and assisting directions.

With the knowledge that force fluctuations are important for modeling bidirectional transport, the next step was to make predictions within the frame of the EPB-model. As kinesin and dynein do not only differ in their preferred direction of motion but also in their reaction on external control parameters or the applied force, we included these features in the EPB-model by a biologically more relevant choice of motor properties. In detail, we

implemented the catch-bond effect for dynein for increasing force, which has apparently no relevance for kinesin motors. Furthermore, we took into account that the stall force, the maximal force a motor can withstand and keep on walking in its preferred direction, depends much stronger on the ATP concentration for dynein motors than for kinesin motors [62]. In order to test whether these assumptions in the frame of the EPB-model produce reasonable motion characteristics, the variance of the cargo displacement was calculated and compared to *in vivo* results [22, 71]. The variance of the cargo displacement is a particularly robust measure since it does neither require the definition of spatial nor temporal thresholds and can be used in order to characterize the motion in the class of anomalous diffusion. In experiments it was shown that bidirectionally moving cargo mainly exhibits superdiffusive behavior on intermediate time scales, corresponding to an exponent $1 < \gamma < 2$ defined as the algebraic growth of the variance with time (variance $\sim t^{\gamma}$). With the EPB-model, exponents, which agree almost perfectly to *in vivo* results, were produced [22,62]. The mechanical coupling of the motors induced time-correlated cargo trajectories. The exponent $\gamma$ as well as the time at which one observed the transition to Gaussian displacement distributions are parameter-dependent. For typical parameter combinations the crossover to diffusion takes place at time intervals of the order of one second. At shorter time scales, in *in vivo* experiments subdiffusive motion was found ($\gamma < 1$) [71]. With the pure EPB-model this type of motion cannot be observed but thermal fluctuations of the surrounding environment have to be taken into account. For a particle moving in the potential created by the motor springs under the influence of thermal noise moves subdiffusively on time scales of up to 30 ms, which is in perfect agreement with experiments [71]. Within the frame of the EPB-model taking thermal fluctuations into account the three different motion regimes can be found without taking any network effects or the motion of the underlying filament into account. Here, the anomalous diffusion is a pure product of a correlation induced via the coupling of the motors to the cargo.

Moreover, it was found that trajectories produced with the EPB-model exhibit different dynamic regimes. Generically one observes biased motion of the cargo, since the activity of dynein and kinesin motors can only be balanced in a very narrow interval of the external control parameters. In this thesis the viscosity and ATP-concentration were used in order to model external influences. Naively one would expect faster cargo transport for higher concentrations of ATP and lower viscosities. With the EPB-model however, it was shown that this is not the generic case. The response to both environmental parameters is non-monotonous. Counter-intuitively, the cargo accelerated with increasing viscosity within a given range of parameters. Furthermore, an unexpected response of the cargo dynamics to variation of the ATP concentration was found. Not only a change of the bias was observed but also a non-monotonous dependence of the width of the displacement distribution on the ATP concentration.

In crowded areas of the cell, interactions between different cargos as well as between

cargo and filament may apply forces on the molecular motors. The EPB-model results showed that this may lead to an inversion of the cargo's bias, even if no distinct control mechanism is applied. The ability of the cargo to change its direction in a crowded environment i.e. an environment of higher effective viscosity, may give an argument why the transport of cargo by oppositely directed motors can be beneficial for the cell. In order to test this hypothesis the filament on which the motor-cargo complex moves was confined by two viscous barriers. For low viscosities or small areas of increased viscosity the pure cargo diffusion is faster than an actively transported one, since in the latter case the cargo can be trapped in the potential of motor springs. In macroscopic crowded areas of the cell, however, the situation is inverted: While the diffusively moving cargo drastically slows down, the actively transported one keeps its motility to a large extend. This illustrates that the cell can use the asymmetry between the motors as a driving force.

By means of the EPB-model the effects occurring due to the interaction of motors pulling a cargo were investigated. But inside a cell the environment is more complicated and in general many cargos move along the same microtubule. In order to capture the essential dynamics of a single cargo pulled by two teams of motors, a coarse-grained approach was introduced. Therefore, the characteristic motion of a cargo in the EPB-model was analyzed and a particle with four internal states was designed. These four states represent on the one hand slow and fast diffusion and on the other hand left and right biased motion. With a appropriate choice of transitions between the single states it was possible to define a symmetric model. The particle showed the same signatures as a cargo in the EPB-model concerning the turning time distribution characterized by two length scales, but gives a better base for analytic predictions.

The main emphasis lied on the analysis of possible particle accumulations in a long cell like an axon. Therefore, several of these particles with internal states were considered to move along an one-dimensional periodic lattice considering exclusion at each site. Due to the change between the single states the system shows signatures of a time-dependent particle-wise disorder. This led, though the single particles were chosen to be symmetric, to a macroscopic clustering along the lattice. As a result, the probability distribution for the distance between particles showed two different exponential decays. The probability to find small distances was increased. This increase of probability was reflected in a decreased velocity and flux compared to a symmetric simple exclusion process.

The fact that the probability distribution does not decay in a purely exponential form, shows that the process with internal states is not a zero-range process but that correlations between the particles exist. Hence, a mean-field description of the model is not exact. iIndeed, from Monte Carlo simulations of the lattice model we found that two-point correlations exist. Though, for the total distribution for the distances, defined as the sum of distributions of the four states, the asymptotic behavior is the same as in the mean-field model.

In a second approach to study collective effects in exclusion models a half-open chain was introduced, which was inspired by the dynein dynamics at the tip of hyphal cells. In this system an accumulation of dynein motors was observed [74]. In order to model this accumulation, a rather complex model was introduced by Lin *et al.* [79]. This model shows for significant range of parameters a phase characterized by periodic changes in the particle density. In this thesis a minimal model, reproducing these global periodic density changes, was defined. The base for this model is given by two one-dimensional lanes with an open and a closed end, representing a tubular geometry. Two types of particles hop along these equal lanes: plus particles, which are injected at the open boundary, hop towards the reflecting boundary. All along the filament they can convert their type and become a minus particle, hopping in opposite direction. Just as plus particles, minus particles can convert to plus particles with the same rate. At the the open boundary, minus particles leave the system again. Therefore, the number of particles remains conserved in the bulk but changes globally due to the open boundary. By introducing an asymmetry between the two types of particles a phase transition from a low density phase to a phase, characterized by the aforementioned periodic density change, was found. In this thesis, it was assumed that only minus particles can change lanes, in case they are blocked by another particle in the current lane. The actual model under investigation was not the explicit particle model but a mean-field description of it.

This mean-field model was defined by the master equations of the particle densities $\rho$ (for plus particles) and $\sigma$ (for minus particles). It was found that the model exhibits either a very regular pulsing behavior or a low density phase, just as the particle model. Throughout the whole work the trivial case for which particles cannot change their type was ignored as it simply results in a filled lattice. For the low density phase, the (stationary) bulk density profile, which decreases linearly along the lattice, was determined analytically.

The pulsing phase was more complicated to analyze. In the filling stage, for a small type conversion rate an approximation for the filling velocity was found. In the emptying stage the system's dynamics are very slow. A front moves backwards, separating a dense region on the left and a dilute region on the right. In the dense area (between the entrance and the shock position) the two densities deviate from $\frac{1}{2}$ only by a very small value $\eta$, typically in the order of $10^{-3}$ or smaller. By neglecting the type conversion, a Rankine-Hugoniot relation can be used in order to predict the shock's backward velocity, as a function depending on this deviation $\eta$. The resulting shock velocity showed good agreement with the numerically obtained results.

In the dense region some oscillations in the densities were observed. These were triggered by the shock movement on the discrete lattice. By means of a stability analysis of the densities around a plateau value, it was obtained that the system is dynamically stable in a sense that temporal perturbation from flat solutions decay exponentially with time. However, the system is not spatially stable. For low particle densities, the spatial perturbations

on plateaux solutions decay exponentially in space, representing the boundary layer found in the entrance region. For increasing densities it was found that the modulus of the eigenvalues of the propagation matrix exceeds one and further has a non-zero imaginary part. This explained on the one hand the density oscillations close to the shock and the exponentially decreasing envelop of these oscillations from the shock towards the bulk density in the dense region in the emptying stage of the pulsing phase.

In the dilute region of the pulsing phase, the system shows some oscillatory behavior as well. It was observed in the numerical solution of the master equations that density pulses are released from the shock and propagate through the system to the reflecting boundary. The pulse emission is connected to hopping of the shock from one lattice site to the next. Recording of the densities at one lattice site with time, showed that the changes are not sinusoidal, which indicated that the effect has its origin in the non-linearity of the master equation.

Furthermore, we expanded the system's master equations in space and obtained a set of partial differential equations. At first order this system is of mixed type (hyperbolic/elliptic) and the non-hyperbolicity occurs in the filling as well as at the shock position.

From the mean-field description it was not possible to find a closed form for the pulsing period. In order to obtain it in another way, an effective Markov chain for the open end was introduced. By this, the injection of holes in the system was modeled explicitly. From the integration of the mean-field equations it follows that the boundary layer is rather thin, usually of about four lattice sites. Under the assumption that the hopping rate is much bigger than the type conversion rate, only type conversion events were considered and furthermore, only one effective lane was assumed. Under these assumptions, the predicted period for the shock moving through the system was three orders too big. This result indicated that the lane change is essential for the creation of holes, which again reflects that without the asymmetry between the two types of particles no pulsing phase occurs.

Though we were able to make several predictions for this model, and in particular to characterize the densities in the low density phase, in the pulsing phase the analytic prediction for the density deviation from $\frac{1}{2}$ in the dense region remains an open question. Close to the shock position, at the entrance and at the reflecting boundary steep gradients in the densities occurred. One of the main problems was how to take the type changing into account. Another problem was the order of the terms. The particular shape of the densities made it difficult to find a criterion that predicts the phase transition. A full characterization of the pulsing phase would allow one to find a criterion to predict the phase transition line.

Several characteristics of cargo transport as they are discussed above have been observed in *in vivo* experiments [22,71]. But still, these *in vivo* experiments are not so simple to interpret due to network effects, the heterogeneous environment or the interplay of many cargos. By means of the EPB-model we showed that the complex particle dynamics has an intriguing response to external control parameters.

The recent progress in dynein motility assays allows one now to test the predictions made with the EPB-model *in vitro* [84]. As one of the first realizations, in *in vitro* experiments by M. Vershinin *et al.* the temperature is changed. Remarkably, this influences dynein's stall force and therefore they find a similar effect on the cargo bias as we do by changing the ATP concentration[1]. The realization of *in vitro* assays with two teams of motors bound to a cargo would allow one to study the mechanic coupling of molecular motors via the cargo in a much simpler environment than in the living cell. In particular, such experiments could help validate one of the main results of this work that SBD states are merely an artifact of a specific type of model and therefore probably irrelevant for realistic biological situations. Further, in *in vitro* assays the environment could be changed in a well-defined manner such that the for instance the ATP concentration would be changed or an effective force could be realized locally by an optical trap, to test our predictions. On-going experiments with isolated endogenous cargos give first results and are able to reconstitute the cargo motility [48].

These cargos may further deepen the understanding of the interaction between several transported cargos as several of them could be put on a single stabilized microtubule in order to study the effects occurring due to steric hindering. Furthermore, the effects of the underlying MT network could be studied. Once one understands these dynamics, it will be possible to figure out what disrupts transport in neuronal diseases.

Besides the biological importance, this thesis contributes to the deeper understanding of interacting systems in general. By means of two different exclusion processes we showed that internal degrees of freedom and the geometry trigger intriguing collective effects and phase transitions.

[1]These results are not yet published but were discussed at the conference *Multiscale Motility of biomolecular motors*, 2015 in Berlin.

# Appendix A

# Simulation parameters

| | | | | | |
|---|---|---|---|---|---|
| $v_F$ | 1000 nm/s | $F_D$ | 3 pN | $\mathcal{K}$ | 0.1 pN/nm |
| $v_B$ | 6 nm/s | $k_d^0$ | 1 $s^{-1}$ | $L_0$ | 110 nm |
| $F_S$ | 6 pN | $k_a$ | 5 $s^{-1}$ | $d$ | 8 nm |
| $\eta$ | $1 \cdot 10^{-4}$ kg $s^{-1}$ | $m$ | $5 \cdot 10^{-14}$ kg | $R$ | 1 $\mu$m |

**Table A1:** Simulation parameter for the symmetric motors EPB-model taken from [86] and [72].

| | **kinesin** | **dynein** | Ref. |
|---|---|---|---|
| $d$ | 8 nm | | [21, 117] |
| $N_\pm$ | 5 | | [121] |
| $L_0$ | 110 nm | | [72] |
| $v_F$ | 1000 nm/s | | [21, 117] |
| $v_B$ | 6 nm/s | | [21, 40]* |
| $\mathcal{K}$ | 0.1 pN/nm | | [72]* |
| $k_a$ | $5\ \mathrm{s}^{-1}$ | | [73, 86] |
| $k_d^0$ | $1\ \mathrm{s}^{-1}$ | | [72]* |
| $f$ | 1 pN | | |
| $F_S$ | 2.6 pN | 0.3-1.2 pN | [82, 108] |
| $k_{\mathrm{cat}}^0$ | $v_F \cdot d^{-1}$ | | [100] |
| $k_{\mathrm{b}}^0$ | $1.3\ \mu\mathrm{M}^{-1}\mathrm{s}^{-1}$ | | [100] |
| $q_{\mathrm{cat}}$ | $6.2 \cdot 10^{-3}$ | | [100] |
| $q_{\mathrm{b}}$ | $4 \cdot 10^{-2}$ | | [100] |
| $\Delta$ | 4267.3 nm | $\max\left(\frac{2.9 \cdot 10^5}{[ATP]^{0.3}} - 28111.1, 8534.6\right)$ nm | eq. (4.12) |
| Environment | | | |
| $k_s$ | $10^6\ \mathrm{s}^{-1}$ | | |
| $\eta$ | 10 mPa·s | | [71]* |
| [ATP] | 0.5 mM | | |
| $T$ | 300 K | | |
| $x_B$ | 50 nm | | |
| Cargo | | | |
| $R$ | 1000 nm | | [115]* |
| $m$ | $10^{-14}$ kg | | |

**Table A2:** The second and third column show the simulation parameters for kinesin and dynein, respectively. The fourth column gives the references providing experimental basis to these values. The * indicates that the experimental values must be considered as orders of magnitude.

# Publications

- *Motility states in bidirectional cargo transport*,
  S. Klein, C. Appert-Rolland, L. Santen,
  **EPL**, 111(68005), 2015.

- *Environmental control of microtubule-based bidirectional cargo transport*,
  S. Klein, C. Appert-Rolland, L. Santen,
  **EPL** 107 18004, 2014.

- *Fluctuation effects in bidirectional cargo transport*,
  S. Klein, C. Appert-Rolland, L. Santen,
  **The European Physical Journal Special Topics**, 223(14):3215-3225, 12/2014

- *Stochastic modeling of cargo transport by teams of molecular motors*,
  S. Klein, C. Appert-Rolland, L. Santen,
  **Proceedings of Traffic and Granular Flow'13** (pp. 609-617). Springer International Publishing. 11/2014

- *Spontaneous pulsing states in an active particle system*,
  S. Klein, C. Appert-Rolland, M. R. Evans,
  submitted

# Bibliography


[1] Bruce Alberts, Alexander Johnson, Julian Lewis, Martin Raff, Keith Roberts, and Peter Walter. Molecular biology of the cell. Garland Science Taylor & Francis Group, 4 edition, 2002.

[2] Bruce Alberts, Alexander Johnson, Julian Lewis, Martin Raff, Keith Roberts, and Peter Walter. Molecular biology of the cell. Garland Science Taylor & Francis Group, 4 edition, 2002.

[3] Shabeen Ally, Adam G. Larson, Kari Barlan, Sarah E. Rice, and Vladimir I. Gelfand. Opposite-polarity motors activate one another to trigger cargo transport in live cells. The Journal of Cell Biology, 187(7):1071–1082, 2009.

[4] C Appert-Rolland, J Cividini, and HJ Hilhorst. Frozen shuffle update for an asymmetric exclusion process on a ring. Journal of Statistical Mechanics: Theory and Experiment, 2011(07):P07009, 2011.

[5] C Appert-Rolland, H J Hilhorst, and G Schehr. Spontaneous symmetry breaking in a two-lane model for bidirectional overtaking traffic. Journal of Statistical Mechanics: Theory and Experiment, 2010(08):P08024, 2010.

[6] Göker Arpağ, Shankar Shastry, William O Hancock, and Erkan Tüzel. Transport by populations of fast and slow kinesins uncovers novel family-dependent motor characteristics important for in vivo function. Biophysical journal, 107(8):1896–1904, 2014.

[7] Richard Arratia. The motion of a tagged particle in the simple symmetric exclusion system on z. The Annals of Probability, 11(2):362–373, 1983.

[8] A. Ashkin, Karin Schutze, J. M. Dziedzic, Ursula Euteneuer, and Manfred Schliwa. Force generation of organelle transport measured in vivo by an infrared laser trap. Nature, 348(6299):346–348, 11 1990.

[9] Peter Ashwin, Congping Lin, and Gero Steinberg. Queueing induced by bidirectional motor motion near the end of a microtubule. Physical Review E, 82(5):051907, 2010.

[10] F. Banuett. Genetics of ustilago maydis, a fungal pathogen that induces tumors in maize. Annual Review of Genetics, 29(1):179–208, 2015/07/27 1995.

[11] Mustansir Barma. Driven diffusive systems with disorder. Physica A: Statistical Mechanics and its Applications, 372(1):22–33, 2006.

[12] S Bartnicki-Garcia, F Hergert, and G Gierz. Computer simulation of fungal morphogenesis and the mathematical basis for hyphal (tip) growth. Protoplasma, 153(1-2):46–57, 1989.

[13] Jonathan S Berg and Richard E Cheney. Myosin-x is an unconventional myosin that undergoes intrafilopodial motility. Nature cell biology, 4(3):246–250, 2002.

[14] Ewa Bielska, Yujiro Higuchi, Martin Schuster, Natascha Steinberg, Sreedhar Kilaru, Nicholas J. Talbot, and Gero Steinberg. Long-distance endosome trafficking drives fungal effector production during plant infection. Nat Commun, 5, 10 2014.

[15] Steven M Block. Kinesin motor mechanics: binding, stepping, tracking, gating, and limping. Biophysical journal, 92(9):2986–2995, 2007.

[16] Sebastián Bouzat and Fernando Falo. The influence of direct motor–motor interaction in models for cargo transport by a single team of motors. Physical Biology, 7(4):046009, 2010.

[17] Sebastián Bouzat and Fernando Falo. Tug of war of molecular motors: the effects of uneven load sharing. Physical Biology, 8(6):066010, 2011.

[18] H. Brunswick. Untersuchungen über die Geschlechts- und Kernverhältnisse bei der Hymenomyzetengattung Coprinus. Number Nr. 5-10 in Botanische abhandlungen. G. Fischer., 1924.

[19] Peter Buchholz. Input Modeling with Phase-Type Distributions and Markov Models: Theory and Applications. Springer, 2014.

[20] Otger Campàs, Cécile Leduc, Patricia Bassereau, Jaume Casademunt, Jean-François Joanny, and Jacques Prost. Coordination of kinesin motors pulling on fluid membranes. Biophysical Journal, 94(12):5009 – 5017, 2008.

[21] N. J. Carter and R. A. Cross. Mechanics of the kinesin step. Nature, 435(7040):308–312, 05 2005.

[22] Avi Caspi, Rony Granek, and Michael Elbaum. Diffusion and directed motion in cellular transport. Physical Review E, 66(1):011916, 2002.

[23] D. Chowdhury. Stochastic mechano-chemical kinetics of molecular motors: A multidisciplinary enterprise from a physicist's perspective. Physics Reports, 529(1):1–197, 2013.

[24] Debashish Chowdhury, Ludger Santen, and Andreas Schadschneider. Statistical physics of vehicular traffic and some related systems. Physics Reports, 329(4):199–329, 2000.

[25] Luca Ciandrini, M. Carmen Romano, and Andrea Parmeggiani. Stepping and crowding of molecular motors: Statistical kinetics from an exclusion process perspective. Biophysical Journal, 107(5):1176–1184, 9 2014.

[26] Iain D Couzin, Jens Krause, Richard James, Graeme D Ruxton, and Nigel R Franks. Collective memory and spatial sorting in animal groups. Journal of theoretical biology, 218(1):1–11, 2002.

[27] AI Curatolo, MR Evans, Y Kafri, and J Tailleur. Multilane driven diffusive systems. arXiv preprint arXiv:1510.04150, 2015.

[28] Kurt J. De Vos, Andrew J. Grierson, Steven Ackerley, and Christopher C. J. Miller. Role of axonal transport in neurodegenerative diseases. Annual Review of Neuroscience, 31(1):151–173, 2015/10/19 2008.

[29] B. Derrida. An exactly soluble non-equilibrium system: The asymmetric simple exclusion process. Physics Reports, 301(1–3):65–83, 7 1998.

[30] Bernard Derrida, MR Evans, Vincent Hakim, and Vincent Pasquier. Exact solution of a 1d asymmetric exclusion model using a matrix formulation. Journal of Physics A: Mathematical and General, 26(7):1493, 1993.

[31] C. Domb. Phase Transitions and Critical Phenomena. Number Bd. 19. Elsevier Science, 2000.

[32] Cyril Domb, Royce KP Zia, B Schmittmann, and Joel L Lebowitz. Statistical mechanics of driven diffusive systems, volume 17. Academic Press, 1995.

[33] M. Ebbinghaus, C. Appert-Rolland, and L. Santen. Bidirectional transport on a dynamic lattice. Physical Review E, 82(4):040901–, 10 2010.

[34] Maximilian Ebbinghaus and Ludger Santen. A model for bidirectional traffic of cytoskeletal motors. Journal of Statistical Mechanics: Theory and Experiment, 2009(03):P03030, 2009.

[35] M. R. Evans, D. P. Foster, C. Godrèche, and D. Mukamel. Asymmetric exclusion model with two species: Spontaneous symmetry breaking. Journal of Statistical Physics, 80(1-2):69–102, 1995.

[36] M. R. Evans, D. P. Foster, C. Godrèche, and D. Mukamel. Spontaneous symmetry breaking in a one dimensional driven diffusive system. Physical Review Letters, 74(2):208–211, 01 1995.

[37] M R Evans and T Hanney. Nonequilibrium statistical mechanics of the zero-range process and related models. Journal of Physics A: Mathematical and General, 38(19):R195, 2005.

[38] MR Evans. Bose-einstein condensation in disordered exclusion models and relation to traffic flow. EPL (Europhysics Letters), 36(1):13, 1996.

[39] MR Evans, Y Kafri, KEP Sugden, and J Tailleur. Phase diagrams of two-lane driven diffusive systems. Journal of Statistical Mechanics: Theory and Experiment, 2011(06):P06009, 2011.

[40] Arne Gennerich, Andrew P. Carter, Samara L. Reck-Peterson, and Ronald D. Vale. Force-induced bidirectional stepping of cytoplasmic dynein. Cell, 131(5):952–965, 11 2007.

[41] Daniel T. Gillespie. Monte carlo simulation of random walks with residence time dependent transition probability rates. Journal of Computational Physics, 28(3):395–407, 9 1978.

[42] Daniel T Gillespie. Exact numerical simulation of the ornstein-uhlenbeck process and its integral. Physical review E, 54(2):2084, 1996.

[43] Steven P. Gross, M. Carolina Tuma, Sean W. Deacon, Anna S. Serpinskaya, Amy R. Reilein, and Vladimir I. Gelfand. Interactions and regulation of molecular motors in xenopus melanophores. The Journal of Cell Biology, 156(5):855–865, 2002.

[44] Steven P Gross, Michael Vershinin, and George T Shubeita. Cargo transport: two motors are sometimes better than one. Current Biology, 17(12):R478–R486, 2007.

[45] Steven P Gross, Michael A Welte, Steven M Block, and Eric F Wieschaus. Dynein-mediated cargo transport in vivo a switch controls travel distance. The Journal of cell biology, 148(5):945–956, 2000.

[46] Steven P. Gross, Michael A. Welte, Steven M. Block, and Eric F. Wieschaus. Coordination of opposite-polarity microtubule motors. The Journal of Cell Biology, 156(4):715–724, 2002.

[47] William O Hancock. Bidirectional cargo transport: moving beyond tug of war. Nature Reviews Molecular Cell Biology, 15(9):615–628, 2014.

[48] Adam G. Hendricks, Yale E. Goldman, Erika L. F. Holzbaur, and Ronald D. Vale. Chapter Fourteen - Reconstituting the Motility of Isolated Intracellular Cargoes, volume 540, pages 249–262. Academic Press, 2014.

[49] Adam G. Hendricks, Eran Perlson, Jennifer L. Ross, Harry W. Schroeder III, Mariko Tokito, and Erika L.F. Holzbaur. Motor coordination via a tug-of-war mechanism drives bidirectional vesicle transport. Current Biology, 20(8):697 – 702, 2010.

[50] Malte Henkel and Gunter Schütz. Boundary-induced phase transitions in equilibrium and non-equilibrium systems. Physica A: Statistical Mechanics and its Applications, 206(1):187–195, 1994.

[51] HJ Hilhorst and C Appert-Rolland. A multi-lane tasep model for crossing pedestrian traffic flows. Journal of Statistical Mechanics: Theory and Experiment, 2012(06):P06009, 2012.

[52] Martin Howard, Andrew D Rutenberg, and Simon de Vet. Dynamic compartmentalization of bacteria: accurate division in e. coli. Physical review letters, 87(27):278102, 2001.

[53] Alexander John, Andreas Schadschneider, Debashish Chowdhury, and Katsuhiro Nishinari. Characteristics of ant-inspired traffic flow. Swarm Intelligence, 2(1):25–41, 2008.

[54] Róbert Juhász. Dynamics at barriers in bidirectional two-lane exclusion processes. Journal of Statistical Mechanics: Theory and Experiment, 2010(03):P03010, 2010.

[55] Róbert Juhász, Ludger Santen, and Ferenc Iglói. Partially asymmetric exclusion processes with sitewise disorder. Phys. Rev. E, 74:061101, Dec 2006.

[56] N.G. Van Kampen. Stochastic processes in physics and chemistry stochastic processes in physics and chemistry stochastic processes in physics and chemistry stochastic processes in physics and chemistry. North-Holland Personal Library, 2007.

[57] Mehran Kardar, Giorgio Parisi, and Yi-Cheng Zhang. Dynamic scaling of growing interfaces. Physical Review Letters, 56(9):889–892, 03 1986.

[58] Sheldon Katz, JoelL. Lebowitz, and Herbert Spohn. Nonequilibrium steady states of stochastic lattice gas models of fast ionic conductors. Journal of Statistical Physics, 34(3-4):497–537, 1984.

[59] Jirayr Kevorkian. Partial differential equations: Analytical solution techniques, volume 6. Springer Science & Business Media, 2000.

[60] Stephen M King. Aaa domains and organization of the dynein motor unit. Journal of Cell Science, 113(14):2521–2526, 2000.

[61] Sarah Klein, Cécile Appert-Rolland, and Martin Evans. Spontaneous pulsing states in an active particle system. in preparation, 2015.

[62] Sarah Klein, Cécile Appert-Rolland, and Ludger Santen. Environmental control of microtubule-based bidirectional cargo transport. EPL, 107(1):18004, 2014.

[63] Sarah Klein, Cécile Appert-Rolland, and Ludger Santen. Fluctuation effects in bidirectional cargo transport. EPJST, 223(14):3215–3225, 2014.

[64] Sarah Klein, Cécile Appert-Rolland, and Ludger Santen. Motility states in bidirectional cargo transport. EPL, 111(68005), 2015.

[65] Sarah Klein, Cécile Appert-Rolland, and Ludger Santen. Stochastic modeling of cargo transport by teams of molecular motors. Traffic and Granular Flow'13, pages 609–617, 2015.

[66] D J Klionsky, P K Herman, and S D Emr. The fungal vacuole: composition, function, and biogenesis. Microbiological Reviews, 54(3):266–292, 09 1990.

[67] Hiroaki Kojima, Etsuko Muto, Hideo Higuchi, and Toshio Yanagida. Mechanics of single kinesin molecules measured by optical trapping nanometry. Biophysical Journal, 73(4):2012–2022, 1997.

[68] Joachim Krug. Boundary-induced phase transitions in driven diffusive systems. Physical review letters, 67(14):1882, 1991.

[69] Joachim Krug. Origins of scale invariance in growth processes. Advances in Physics, 46(2):139–282, 1997.

[70] Joachim Krug and Pablo A Ferrari. Phase transitions in driven diffusive systems with random rates. Journal of Physics A: Mathematical and General, 29(18):L465, 1996.

[71] I.M. Kulić, A.E.X. Brown, H. Kim, C. Kural, B. Blehm, P.R. Selvin, P.C. Nelson, and V.I. Gelfand. The role of microtubule movement in bidirectional organelle transport. P.N.A.S., 105:10011–10016, 2008.

[72] Ambarish Kunwar, Suvranta K. Tripathy, Jing Xu, Michelle K. Mattson, Preetha Anand, Roby Sigua, Michael Vershinin, Richard J. McKenney, Clare C. Yu, Alexander Mogilner, and Steven P. Gross. Mechanical stochastic tug-of-war models cannot explain bidirectional lipid-droplet transport. Proceedings of the National Academy of Sciences, 108(47):18960–18965, 2011.

[73] Cécile Leduc, Otger Campàs, Konstantin B Zeldovich, Aurélien Roux, Pascale Jolimaitre, Line Bourel-Bonnet, Bruno Goud, Jean-François Joanny, Patricia Bassereau, and Jacques Prost. Cooperative extraction of membrane nanotubes by molecular motors. Proceedings of the National Academy of Sciences of the United States of America, 101(49):17096–17101, 2004.

[74] JH Lenz, I Schuchardt, A Straube, and G Steinberg. A dynein loading zone for retrograde endosome motility at microtubule plus-ends. The EMBO journal, 25(11):2275–2286, 2006.

[75] Andrea C Levi and Miroslav Kotrla. Theory and simulation of crystal growth. Journal of Physics: Condensed Matter, 9(2):299, 1997.

[76] Xin Li, Reinhard Lipowsky, and Jan Kierfeld. Bifurcation of velocity distributions in cooperative transport of filaments by fast and slow motors. Biophysical Journal, 104(3):666–676, 2 2013.

[77] MJ Lighthill and GB Whitham. On kinematic waves. i. flood movement in long rivers. volume 229, pages 281–316. The Royal Society, 1955.

[78] Congping Lin, Peter Ashwin, and Gero Steinberg. Motor-mediated bidirectional transport along an antipolar microtubule bundle: A mathematical model. Physical Review E, 87(5):052709, 2013.

[79] Congping Lin, Gero Steinberg, and Peter Ashwin. Bidirectional transport and pulsing states in a multi-lane asep model. Journal of Statistical Mechanics: Theory and Experiment, 2011(09):P09027, 2011.

[80] Harvey F Lodish, Arnold Berk, S Lawrence Zipursky, Paul Matsudaira, David Baltimore, and James Darnell. Molecular cell biology, volume 4. Citeseer, 2000.

[81] Carolyn T. MacDonald, Julian H. Gibbs, and Allen C. Pipkin. Kinetics of biopolymerization on nucleic acid templates. Biopolymers, 6(1):1–25, 1968.

[82] Roop Mallik, Brian C. Carter, Stephanie A. Lex, Stephen J. King, and Steven P. Gross. Cytoplasmic dynein functions as a gear in response to load. Nature, 427(6975):649–652, 02 2004.

[83] Roop Mallik and Steven P. Gross. Molecular motors: Strategies to get along. Current Biology, 14(22):R971 – R982, 2004.

[84] Richard J McKenney, Walter Huynh, Marvin E Tanenbaum, Gira Bhabha, and Ronald D Vale. Activation of cytoplasmic dynein motility by dynactin-cargo adapter complexes. Science, 345(6194):337–341, 2014.

[85] Leonor Michaelis and Maud L Menten. Die kinetik der invertinwirkung. Biochem. z, 49(333-369):352, 1913.

[86] Melanie J. I. Müller, Stefan Klumpp, and Reinhard Lipowsky. Tug-of-war as a cooperative mechanism for bidirectional cargo transport by molecular motors. Proceedings of the National Academy of Sciences, 105(12):4609–4614, 2008.

[87] Kai Nagel and Michael Schreckenberg. A cellular automaton model for freeway traffic. Journal de physique I, 2(12):2221–2229, 1992.

[88] Alexandra A. Nascimento, Joseph T. Roland, and Vladimir I. Gelfand. Pigment cells: A model for the study of organelle transport. Annual Review of Cell and Developmental Biology, 19(1):469–491, 2003.

[89] Helen Nilsson Sköld, Sara Aspengren, and Margareta Wallin. Rapid color change in fish and amphibians–function, regulation, and emerging applications. Pigment cell & melanoma research, 26(1):29–38, 2013.

[90] Simon F Nørrelykke and Henrik Flyvbjerg. Harmonic oscillator in heat bath: Exact simulation of time-lapse-recorded data and exact analytical benchmark statistics. Physical Review E, 83(4):041103, 2011.

[91] Itai Pinkoviezky and Nir S Gov. Modelling interacting molecular motors with an internal degree of freedom. New Journal of Physics, 15(2):025009, 2013.

[92] Sylvain Prolhac, Martin R Evans, and Kirone Mallick. The matrix product solution of the multispecies partially asymmetric exclusion process. Journal of Physics A: Mathematical and Theoretical, 42(16):165004, 2009.

[93] N. Rajewsky, L. Santen, A. Schadschneider, and M. Schreckenberg. The asymmetric exclusion process: Comparison of update procedures. Journal of Statistical Physics, 92(1-2):151–194, 1998.

[94] Sidney Redner. A guide to first-passage processes. Cambridge University Press, 2001.

[95] Damien Robert, Thi-Hanh Nguyen, François Gallet, and Claire Wilhelm. In vivo determination of fluctuating forces during endosome trafficking using a combination of active and passive microrheology. PloS one, 5(4):e10046, 2010.

[96] Hanna Salman, Yotam Gil, Rony Granek, and Michael Elbaum. Microtubules, motor proteins, and anomalous mean squared displacements. Chemical physics, 284(1):389–397, 2002.

[97] Tomohiro Sasamoto and Miki Wadati. Exact results for one-dimensional totally asymmetric diffusion models. Journal of Physics A: Mathematical and General, 31(28):6057, 1998.

[98] Andreas Schadschneider and Michael Schreckenberg. Car-oriented mean-field theory for traffic flow models. Journal of Physics A: Mathematical and General, 30(4):L69, 1997.

[99] Manfred Schliwa and Gunther Woehlke. Molecular motors. Nature, 422:759–765, 04 2003.

[100] Mark J. Schnitzer, Koen Visscher, and Steven M. Block. Force production by single kinesin motors. Nat Cell Biol, 2(10):718–723, 10 2000.

[101] Isabel Schuchardt, Daniela Assmann, Eckhard Thines, Christian Schuberth, and Gero Steinberg. Myosin-v, kinesin-1, and kinesin-3 cooperate in hyphal growth of the fungus ustilago maydis. Molecular Biology of the Cell, 16(11):5191–5201, 2005.

[102] Martin Schuster, Sreedhar Kilaru, Peter Ashwin, Congping Lin, Nicholas J Severs, and Gero Steinberg. Controlled and stochastic retention concentrates dynein at microtubule ends to keep endosomes on track. The EMBO journal, 30(4):652–664, 2011.

[103] Martin Schuster, Sreedhar Kilaru, Gero Fink, Jérôme Collemare, Yvonne Roger, and Gero Steinberg. Kinesin-3 and dynein cooperate in long-range retrograde endosome motility along a nonuniform microtubule array. Molecular biology of the cell, 22(19):3645–3657, 2011.

[104] Martin Schuster, Reinhard Lipowsky, Marcus-Alexander Assmann, Peter Lenz, and Gero Steinberg. Transient binding of dynein controls bidirectional long-range motility of early endosomes. Proceedings of the National Academy of Sciences, 108(9):3618–3623, 2011.

[105] Arne Seitz, Hiroaki Kojima, Kazuhiro Oiwa, Eva-Maria Mandelkow, Young-Hwa Song, and Eckhard Mandelkow. Single-molecule investigation of the interference between kinesin, tau and map2c. The EMBO journal, 21(18):4896–4905, 2002.

[106] M. Reza Shaebani, Zeinab Sadjadi, Igor M. Sokolov, Heiko Rieger, and Ludger Santen. Anomalous diffusion of self-propelled particles in directed random environments. submitted, 2014.

[107] Leah B Shaw, RKP Zia, and Kelvin H Lee. Totally asymmetric exclusion process with extended objects: a model for protein synthesis. Physical Review E, 68(2):021910, 2003.

[108] George T. Shubeita, Susan L. Tran, Jing Xu, Michael Vershinin, Silvia Cermelli, Sean L. Cotton, Michael A. Welte, and Steven P. Gross. Consequences of motor copy number on the intracellular transport of kinesin-1-driven lipid droplets. Cell, 135(6):1098 – 1107, 2008.

[109] P. Silar and F. Malagnac. Les champignons redécouverts. Belin, 2013.

[110] Virupakshi Soppina, Arpan Kumar Rai, Avin Jayesh Ramaiya, Pradeep Barak, and Roop Mallik. Tug-of-war between dissimilar teams of microtubule motors regulates transport and fission of endosomes. Proceedings of the National Academy of Sciences, 106(46):19381–19386, 2009.

[111] Frank Spitzer. Interaction of markov processes. Advances in Mathematics, 5(2):246–290, 10 1970.

[112] Gero Steinberg. Hyphal growth: a tale of motors, lipids, and the spitzenkörper. Eukaryotic Cell, 6(3):351–360, 2007.

[113] Gero Steinberg and Jose Perez-Martin. Ustilago maydis, a new fungal model system for cell biology. Trends in cell biology, 18(2):61–67, 2008.

[114] Julien Tailleur, MR Evans, and Y Kafri. Nonequilibrium phase transitions in the extraction of membrane tubes by molecular motors. Physical review letters, 102(11):118109, 2009.

[115] Abdou Rachid Thiam, Robert V Farese Jr, and Tobias C Walther. The biophysics and cell biology of lipid droplets. Nature Reviews Molecular Cell Biology, 14(12):775–786, 2013.

[116] Shiori Toba, Tomonobu M. Watanabe, Lisa Yamaguchi-Okimoto, Yoko Yano Toyoshima, and Hideo Higuchi. Overlapping hand-over-hand mechanism of single molecular motility of cytoplasmic dynein. Proceedings of the National Academy of Sciences, 103(15):5741–5745, 2006.

[117] Shiori Toba, Tomonobu M. Watanabe, Lisa Yamaguchi-Okimoto, Yoko Yano Toyoshima, and Hideo Higuchi. Overlapping hand-over-hand mechanism of single molecular motility of cytoplasmic dynein. Proceedings of the National Academy of Sciences, 103(15):5741–5745, 2006.

[118] O Valiron, N Caudron, and D Job. Microtubule dynamics. Cellular and Molecular Life Sciences CMLS, 58(14):2069–2084, 2001.

[119] Matthias Weiss, Markus Elsner, Fredrik Kartberg, and Tommy Nilsson. Anomalous subdiffusion is a measure for cytoplasmic crowding in living cells. Biophysical journal, 87(5):3518–3524, 2004.

[120] Michael A Welte. Bidirectional transport along microtubules. Current Biology, 14(13):R525–R537, 7 2004.

[121] Michael A Welte, Steven P Gross, Marya Postner, Steven M Block, and Eric F Wieschaus. Developmental regulation of vesicle transport in< i> drosophila</i> embryos: Forces and kinetics. Cell, 92(4):547–557, 2 1998.

[122] Marko Woelki, Andreas Schadschneider, and Michael Schreckenberg. Asymmetric exclusion processes with shuffled dynamics. JPA, 39(1):33–44, 2005.

# Acknowledgments

Finally, I want to thank the people who supported me on my way and made this work possible.

At first I want to express my thanks to my two supervisors Cécile Appert-Rolland and Ludger Santen who supported me right from the very first day, already during my Bachelor's and Master's project and by that always gave me the feeling that I'm doing a good job. And this not only during daily research but also by encouraging me to present our work at many opportunities in different environments and discuss it with various people. For my thesis they gave me the opportunity to work at both universities - Universität des Saarlands and Université Paris-Sud. I enjoyed very much seeing two quite different working environments.

A special thank also to Martin Evans from University of Edinburgh with whom I worked on the project of pulsing states. He always had an open ear and taught many mechanisms and approaches for driven lattice gases. Thanks to him (and his publications) my tool box in statistical physics grew quite a lot.

Furthermore, I want to thank Danielle Hilhorst, Frédéric Lagoutière, Christian Tenaud, Henk Hilhorst and Pascal Viot for fruitful discussions on the subject of pulsing states.

Apart from that, I want to thank all friends and colleagues for good times at both university. Here in particular Daniel Bahr and Katharina Rojan in Saarbrücken, and Andrei Angelescu and Luiz Henrique Vale Silva in Orsay for making the time spent in the office more lively. Further, I thank Sébastien Suignard for an unbelievable patience with me talking in French. A special thank to Richard Carter, Daniel Bahr and Daniel Flormann for proof-reading of this manuscript.

Finally, I thank my parents, Robert and Birgit Klein, and my sister, Julia Klein, for the family support and keeping my options open all the time. They always gave me the feeling to be on a good way with what I'm doing.